Title	High-Field Magnetism of the Spin-1/2 Low-Dimensional Antiferromagnets BaCo2V208 and Cu2(pymca)3(ClO4)
Author(s)	奥谷, 顕
Citation	大阪大学, 2021, 博士論文
Version Type	VoR
URL	https://doi.org/10.18910/81998
rights	
Note	

Doctoral Thesis

High-Field Magnetism of the Spin-1/2 Low-Dimensional Antiferromagnets $BaCo_2V_2O_8$ and $Cu_2(pymca)_3(ClO_4)$

Akira Okutani

Department of Physics, Graduate School of Science
Osaka University

February, 2021

Abstract

Low-dimensional antiferromagnets with a small spin quantum number have been studied extensively because of their intriguing features, such as the appearance of a spin liquid state owing to strong quantum fluctuations. In experimental studies, unconventional magnetic-field induced quantum phase transitions have been observed in such antiferromagnets, and hence high-magnetic fields are required to investigate their properties. In this thesis, we have studied two types of low-dimensional antiferromagnets, the spin-1/2 quasi-one-dimensional (1D) Ising-like antiferromagnet $BaCo_2V_2O_8$ and the honeycomb-lattice antiferromagnet (HLA) $Cu_2(pymca)_3(ClO_4)$, and performed magnetization, electron spin resonance (ESR), specific heat, and magnetostriction measurements in high magnetic field of up to 70 T.

$BaCo_2V_2O_8$ has attracted a lot of attention as a candidate of the spin-1/2 quasi-1D Ising-like antiferromagnet. The Néel state is realized below 5.4 K in zero field, and the field-induced order-disorder transition was observed at 3.9 T in magnetic fields along the [001] (chain) direction. These observations have been explained by the spin-1/2 1D Ising-like antiferromagnet model. Several studies were conducted in transverse magnetic field, and the difference in physical properties between the [100] and [110] directions was reported. The Néel order collapses at approximately 10 T for $H \parallel [100]$, while it does not above this field for $H \parallel [110]$. Therefore, magnetic excitations for these two different directions should be studied. We report on the experimental results of the magnetic susceptibility, the high-field multi-frequency ESR, the specific heat, and the magnetostriction on $BaCo_2V_2O_8$ single crystals in magnetic fields applied along the [100] and [110] directions. Two main ESR branches, which are ascending and descending with increasing magnetic fields, were observed from 400 GHz in zero magnetic field for both directions. The lower ESR branch shows a softening near 10 T for $H \parallel [100]$, whereas no softening was observed up to the saturation field for $H \parallel [110]$. These observations are reproduced by numerical calculations using the density-matrix renormalization group method, including the staggered magnetic fields, which reflects the crystal structure of $BaCo_2V_2O_8$, induced by a uniform external magnetic field and the interchain magnetic exchange interaction. For $H \parallel [100]$, the observed transition magnetic field is reproduced by the calculations for two cases, the staggered magnetic field parameter $C_y = 0.4$ (C_y: the ratio of the staggered field along the y-axis to the external magnetic field) and the finite interchain interaction $J'/J = 0.02$, and $C_y = 0.25$ and $J'/J = 0$. The former calculation agrees well with the observation compared to the latter one. The disordered state above the critical magnetic field for $H \parallel [100]$ is considered to be a field-induced ferromagnetic state or a paramagnetic state, unlike a Tomonaga-Luttinger spin liquid state above the transition field for $H \parallel [001]$.

A number of theoretical studies on HLAs have been conducted, but in contrast, there are few experimental studies owing to the small number of candidate substances. $Cu_2(pymca)_3(ClO_4)$ (pymca: pyrimidine-2-carboxylate) has attracted a substantial interest as a spin-1/2 HLA, because no magnetic long-range order was observed down to 2 K even though this compound was believed to have a regular honeycomb-lattice structure. We report on the experimental results of magnetic susceptibility, specific heat, ESR, and high-field magnetization measurements on a polycrystalline sample of $Cu_2(pymca)_3(ClO_4)$. Magnetic susceptibility exhibits a broad peak at about 25 K, which is typical of a low dimensional antiferromagnet, and the intrinsic susceptibility after subtracting an impurity contribution shows an exponential decrease with lowering temperatures, suggesting a singlet ground state with an energy gap to the lowest excited state. No sign of long-range order was observed down to 0.6 K from the specific heat measurements in zero magnetic field. A paramagnetic signal with $g = 2.13$ was observed in the ESR measurements. The magnetization curve up to 70 T at 1.4 K shows three stepwise increases with 1/3 and 2/3 magnetization plateaus. Assuming three different exchange bonds J_{A}, J_{B} and J_{C} from the crystal structure that was precisely determined by synchrotron X-ray analysis, the calculated magnetization curve by using a quantum Monte Carlo (QMC) method reproduces the observed one when $J_{\mathrm{A}}/k_{\mathrm{B}} = 43.7$ K, $J_{\mathrm{B}}/J_{\mathrm{A}} = 1$ and $J_{\mathrm{C}}/J_{\mathrm{A}} = 0.2$, except the magnetization near 70 T where the observed magnetization indicates another step while the calculated magnetization becomes saturated. The parameters used for the calculation are found to be located in the spin liquid (singlet) phase calculated by a QMC method, which agrees with the experimental observation.

Contents

1 Introduction 1

1-1 $S = 1/2$ One-dimensional Antiferromagnet . . . 1

1-1-1 XXZ Antiferromagnet . . . 1

1-1-2 Ising-like Antiferromagnet: Theory and Experiment . . . 2

1-2 $S = 1/2$ Two-Dimensional Antiferromagnet . . . 8

1-2-1 Various types of $S = 1/2$ Two-Dimensional Antiferromagnets . . 8

1-2-2 Honeycomb-Lattice Antiferromagnets . . . 8

2 Experimental Apparatus and Methods 14

2-1 Magnetic Field Generation Method . . . 14

2-2 Magnetic Measurements (Susceptibility, Magnetization) . . . 16

2-2-1 Magnetic Susceptibility and Magnetization Measurements in Static Magnetic Fields . . . 16

2-2-2 Magnetization Measurements in Pulsed Magnetic Fields . . . 16

2-3 Electron Spin Resonance (ESR) Measurements . . . 17

2-3-1 ESR Measurements in Static Magnetic Fields . . . 17

2-3-2 ESR Measurements in Pulsed Magnetic Fields . . . 19

2-4 Specific Heat Measurements . . . 20

2-5 Magnetostriction Measurements . . . 21

3 $S = 1/2$ Quasi-1D Antiferromagnet $\mathbf{BaCo_2V_2O_8}$ 23

3-1 Introduction . . . 23

3-1-1 Fundamental Properties (Crystal Structure, Low-Field Magnetism) 23

3-1-2 High-Field Magnetism in Longitudinal Magnetic Fields . . . 26

3-1-3 High-Field Magnetism in Transverse Magnetic Fields . . . 34

3-1-4 Purpose of This Study . . . 38

3-2 Experiment and Calculation . . . 39

3-2-1 Crystal Growth . . . 39

3-2-2 Experimental Results . . . 43

3-2-3 Numerical Calculation Method . . . 49

3-2-4 Comparison with Numerical Results . . . 51

3-3 Discussion . . . 58

3-4 Conclusion . . . 60

4 $S = 1/2$ Honeycomb-Lattice Antiferromagnet $\mathbf{Cu_2(pymca)_3(ClO_4)}$ 61

4-1 Introduction . . . 61

4-1-1 Fundamental Properties of M_2(pymca)$_3$(ClO$_4$) (M=Fe, Co, Ni, Cu) 61

4-1-2 Crystal Structure of Cu$_2$(pymca)$_3$(ClO$_4$) . . . 64

4-1-3 Purpose of This Study . . . 65

4-2 Experiment and Calculation . . . 66

4-2-1 Sample preparation . . . 66

4-2-2 Experimental Results . . . 66

4-2-3 Numerical Calculation Method . . . 70

4-2-4 Comparison with Numerical Results . . . 71

4-3 Discussion . . . 74

4-4 Conclusion . . . 77

5 Summary **78**

Appendix I **79**

Appendix II **82**

Appendix III **88**

Publication List **96**

Acknowledgment **98**

1 Introduction

1-1 $S = 1/2$ One-dimensional Antiferromagnet

1-1-1 XXZ Antiferromagnet

One-dimensional (1D) antiferromagnets with a small spin quantum number (S) have been studied extensively because of the simplest strongly correlated system and their unconventional properties, such as quantum phase transitions (QPTs) and quantum critical behavior observed at extremely low temperatures [1]. Furthermore, their magnetic properties are calculated easier than those in higher dimension, and exact solutions of the interacting many body systems in which quantum effects play an important role are obtained in some cases, and are used to test the validity of quantum statistical mechanics. The spin Hamiltonian for this 1D antiferromagnet with $S = 1/2$ and anisotropic exchange interaction in zero magnetic field is given by

$$\mathcal{H} = J \sum_j \left\{ S_j^z S_{j+1}^z + \varepsilon \left(S_j^x S_{j+1}^x + S_j^y S_{j+1}^y \right) \right\}, \tag{1-1-1}$$

where S_j^α is the α component ($\alpha = x$, y, or z) of spin-1/2 operator at site j, J (> 0) is the antiferromagnetic (AF) exchange constant between the nearest-neighbor spins, ε (≥ 0) is the ratio of the xy component of the exchange interaction to its z component, respectively. The ground state of the $S = 1/2$ 1D Heisenberg antiferromagnet ($\varepsilon = 1$) is a spin liquid state [2,3] possessing a spin-spin correlation with a power law decay, which indicates a quantum critical point, and a gapless excitation (a Tomonaga-Luttinger (TL) liquid with a linear energy dispersion). Concerning spin excitations, the spin wave was calculated exactly by des Cloizeaux and Peason in 1962 [4]. The dispersion relation $\varepsilon(k) = \pi|J||\sin k|/2$ was obtained and it is $\pi/2$ times as large as that calculated by the classical spin wave theory [5–7]. This relation was confirmed by the inelastic neutron scattering experiment on $\mathrm{CuCl_2 \cdot 2\,N(C_5D_5)}$ as shown in Fig. 1-1-1 [8].

In addition to this fundamental isotropic antiferromagnet, $S = 1/2$ 1D anisotropic models such as XY ($\varepsilon = \infty$)- and Ising ($\varepsilon = 0$)-types have been studied intensively for long time. Both cases are solvable exactly, especially the Ising-type is easy to solve by hand. For XY-case, the ground state energy, elementary excitation and free energy were obtained exactly by Lieb, Shultz and Mattis [9], and Katsura [10] studied the thermal and magnetic properties including the behavior in a magnetic field.

The $S = 1/2$ Ising-type antiferromagnet in transverse magnetic fields has been studied as a simplest QPT system for long time. As described in Ref. 11 (not only antiferromagnet but also ferromagnet), the advantage of the use of the transverse Ising model is as follows: (i) the one-dimensional case is exactly solvable and the QCP is conformally invariant, and (ii) the model can be mapped to a classical two-dimensional Ising model using the Suzuki-Trotter formalism or the path integral formalism. These two remarkable properties of the models have been exploited to understand quantum phase transitions and their connection to quantum information processing, non-equilibrium dynamics, and quantum annealing [12], followed by an efficient quantum computer in the near future. From the experimental side of the transverse Ising model, one dimensional Ising-like ferromagnet $\mathrm{CoNb_2O_6}$ was studied recently and novel excitation peaks m_1 and m_2 with the golden ratio $m_2/m_1 = (1 + \sqrt{5})/2$ predicted theoretically as a result of E_8 symmetry were observed by neutron scattering experiments [13].

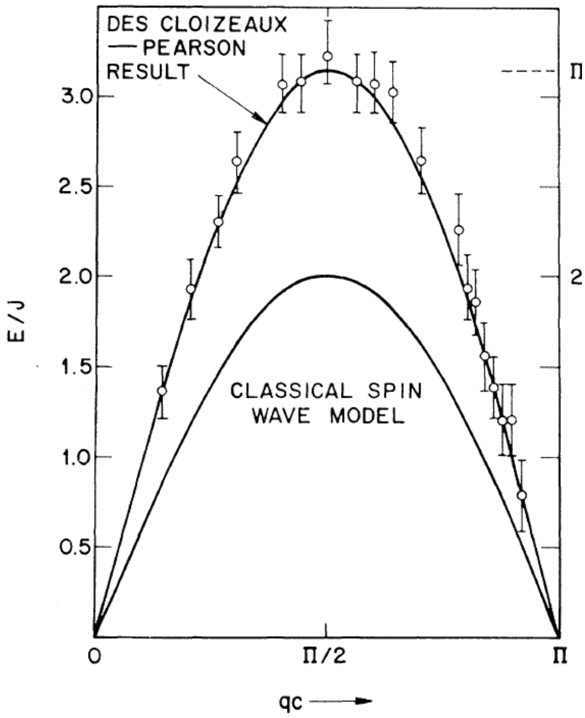

Figure 1-1-1: Energy dispersion of the elementary excitations in $\mathrm{CuCl_2 \cdot 2\,N(C_5D_5)}$ at 1.3 K with the energy in units of $J/k_\mathrm{B} = 13.4$ K (k_B: the Boltzmann constant). The solid lines indicate the theoretical dispersion curves calculated by the method devised by des Cloizeaux and Pearson [4], and by using a classical spin wave model [5]. Quoted from [8].

1-1-2 Ising-like Antiferromagnet: Theory and Experiment

We distinguish two cases depending on ε, namely Ising-like ($0 < \varepsilon < 1$) and XY-like ($\varepsilon > 1$), and describe the nature of Ising-like antiferromagnet in this subsection.

As a prototypical spin system exhibiting QPTs, let us here consider the $S = 1/2$ 1D XXZ antiferromagnet with Ising-like anisotropy in magnetic fields. The ground state at zero magnetic field is a magnetically ordered Néel state, while it changes in a different way depending on the magnetic field direction. On applying a magnetic field along the easy axis (z-axis), the ground state turns into a TL spin liquid state [3,14,15] and eventually it reaches a field-induced ferromagnetic state. That is, two QPTs occur. In addition, within the spin liquid phase, a longitudinal incommensurate correlation is dominant in the low magnetic field region and a transverse staggered one is dominant in the high magnetic field region [16]. In contrast, applying a magnetic field along the hard axis (x-axis), a single QPT from a Néel state to a field-induced ferromagnetic state takes place at a critical field [17,18].

Regarding the experimental realization of the $S = 1/2$ 1D Ising magnets, several Co compounds have been investigated. $\mathrm{CsCo}X_3$ (X=Cl, Br) are known as model substances for the $S = 1/2$ quasi-1D Ising-like antiferromagnet. For magnetic excitations at zero magnetic field, a two-spinon continuum should appear in the pure 1D case, whereas quantized discrete spectra, named as the Zeeman ladder [19], were observed due to the interchain interactions as shown in Fig. 1-1-2 [20,21]. The experimental

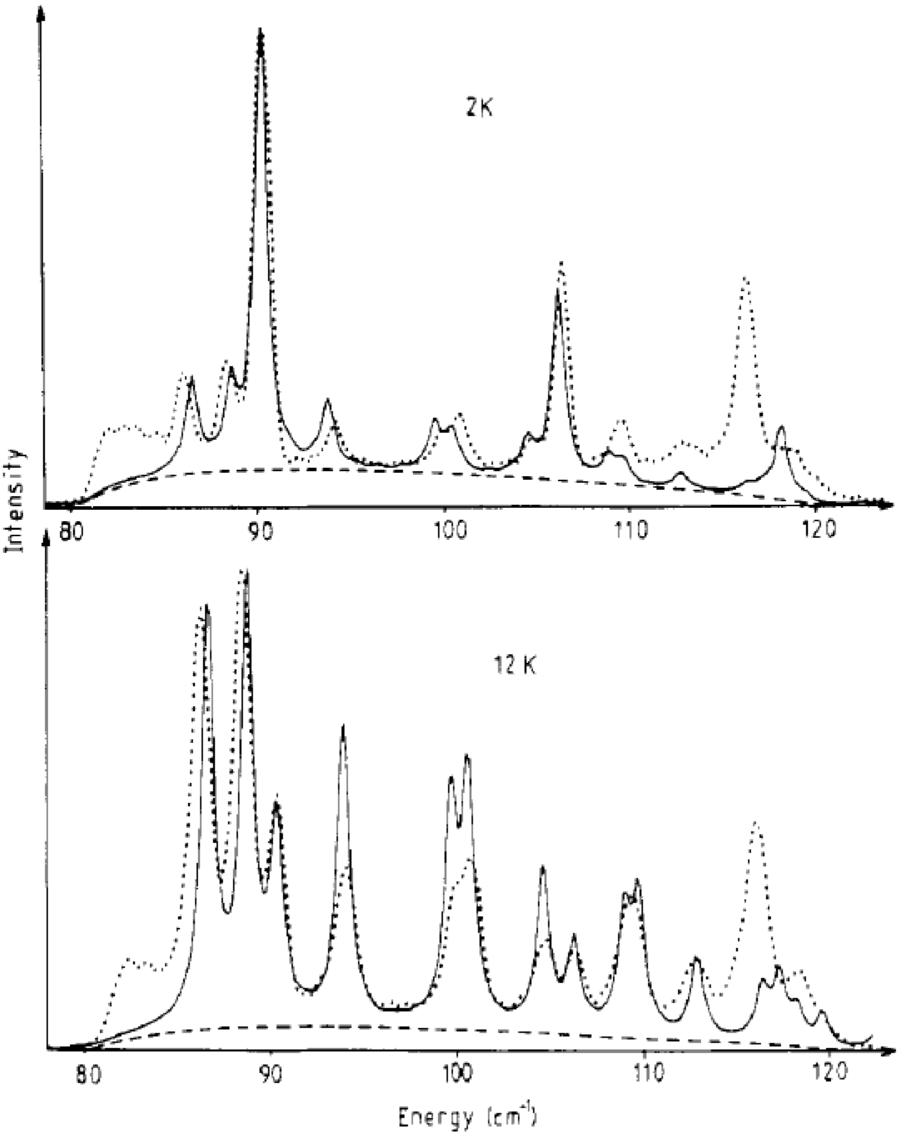

Figure 1-1-2: Comparison of calculation (solid lines) with experiment (dotted lines) for Raman spectra of $CsCoCl_3$ in the xz polarisation at 2 K and 12 K. The calculated continuum is drawn separately as dashed lines. These represent how the continuum spectra is quantized. Quoted from [20].

results of the magnetization (Fig. 1-1-3) and the electron spin resonance (ESR) [22,23] in $\mathrm{CsCoCl_3}$ in pulsed high fields applied parallel to the chain (z-axis) direction were analyzed successfully based on the $S = 1/2$ quasi-1D Ising-like antiferromagnet with an additional small next-nearest-neighbor ferromagnetic interaction [23]. However, the critical field, above which the Néel state is destroyed and the TL spin liquid state is expected to appear, is as high as 33 T owing to large Ising anisotropy. Hence, it was difficult to perform experiments to investigate magnetic properties above the critical field in detail, and a suitable substance with a much lower critical field has been desired. In transverse magnetic fields, the magnetization for $\mathrm{CsCoCl_3}$ was measured in magnetic fields of up to 60 T at 4.2K, and was compared with the calculated magnetization [24]. Figure 1-1-4(a) represents the calculated magnetization curves at designated γ, where γ corresponds to ε in Eq. (1-1-1) and h is the normalized magnetic field by J along the x-direction, and the observed magnetization with $g = 3.5$. When $0 \leq \gamma < 1$, the magnetization saturates only in the limit $h \to \infty$, while the magnetic field derivative of the magnetization ($\mathrm{d}m/\mathrm{d}h$) diverges at a finite critical field, as shown in Fig. 1-1-4(b), indicating the phase transition to the field-induced ferromagnetic state. Although the experimental curve follows the calculated one with $\gamma = 0.13$ at low fields, it deviates from the calculated one near the critical field. A higher magnetic field is required to observe the phase transition in $\mathrm{CsCoCl_3}$.

Recently, $A\mathrm{Co_2V_2O_8}$ (A=Ba, Sr) compounds have been studied intensively as a series of candidates suitable for the study of the field-induced QPT in the $S = 1/2$ 1D Ising-like antiferromagnet, because moderate Ising anisotropy makes the critical field for the easy axis lower and thus we can easily access the field-induced TL spin liquid state and its long-range ordered one due to a weak interchain interaction. We note that both compounds have similar screw-chain structures along the c-axis, although $\mathrm{BaCo_2V_2O_8}$ is centrosymmetric ($I4_1/acd$, non-polar) [25] and $\mathrm{SrCo_2V_2O_8}$ is non-centrosymmetric ($I4_1cd$, polar) [26]. They are very similar in magnetic and thermodynamic properties such as magnetic susceptibility, specific heat [27–29], high-field magnetization [30,31], and ESR spectra of the Zeeman ladder [32–34].

Here, we describe the electronic state of Co^{2+} ion. The total orbital angular momentum L, the spin quantum number S and the lowest LS multiplet of Co^{2+} ion are $L = 3$, $S = 3/2$, and ^4F, respectively. As shown in Fig. 1-1-5, the electronic state shows seven-fold degenerate in a spherically symmetric field, but in a cubically symmetric octahedral ligand-field, it splits into two orbital triplets ($^4T_1, {}^4T_2$) and one orbital singlet ($^4A_2$) [23,35,36]. At this time, the energy difference between the orbital triplet in the ground state and the orbital triplet in the lower excited state is about 10^4 K, and thus only the ground orbital state should be considered at room temperature and lower temperatures. When the quantization axis is taken along the [111] direction, these states can be described by

$$^4A_2 = \frac{\sqrt{2}}{3}\left(\phi_3 - \phi_{-3}\right) - \frac{\sqrt{5}}{3}\phi_0 \tag{1-1-2}$$

$$^4T_2 = \begin{cases} \frac{1}{\sqrt{2}}\left(\phi_3 + \phi_{-3}\right) \\ \frac{1}{\sqrt{6}}\phi_2 - \sqrt{\frac{5}{6}}\phi_{-1} \\ \frac{1}{\sqrt{6}}\phi_{-2} + \sqrt{\frac{5}{6}}\phi_1 \end{cases} \tag{1-1-3}$$

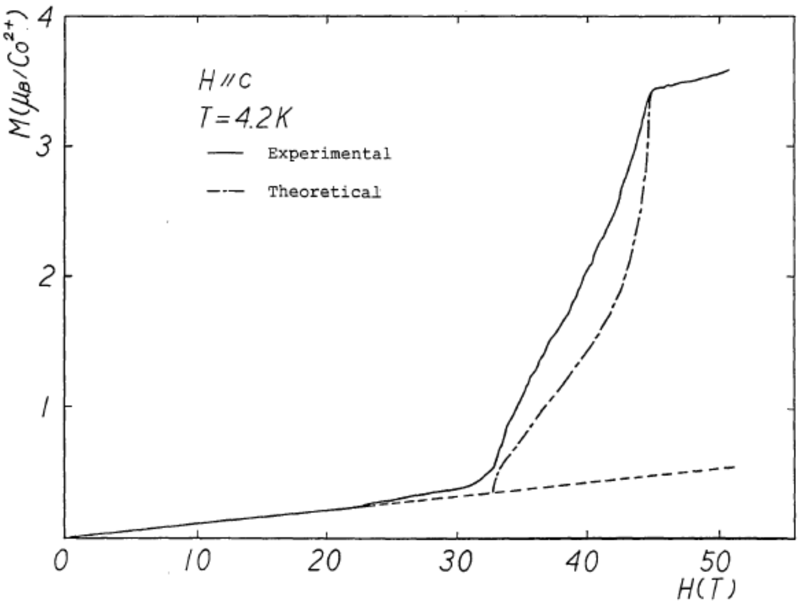

Figure 1-1-3: High-field magnetization curve of $CsCoCl_3$ for $H \parallel c$ at 4.2 K. The solid, dash-dotted, and broken lines indicate the experimental curve, theoretical curve, and Van-Vleck contribution, respectively. Quoted from [22].

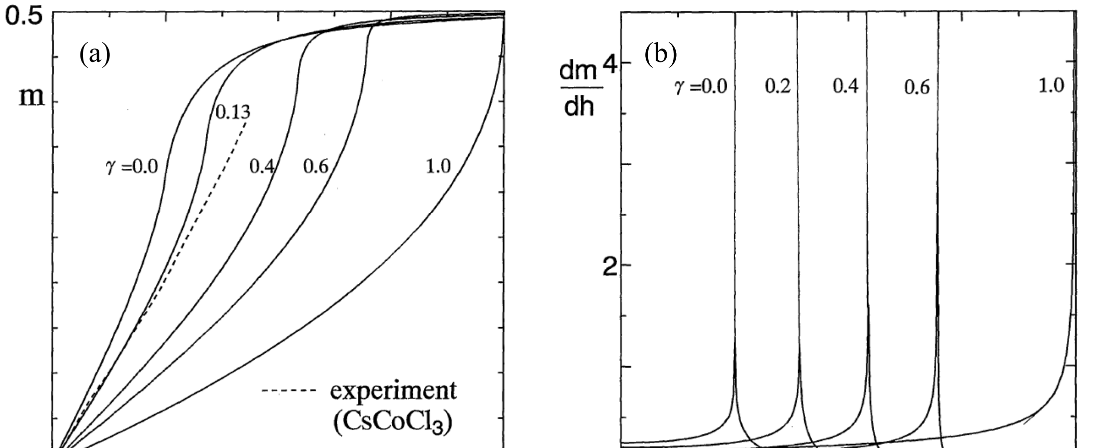

Figure 1-1-4: (a) Magnetization (m) curves calculated at designated γ (solid lines) corresponding to ε in the text, and the experimental m curve for $CsCoCl_3$ at 4.2 K with $g = 3.5$ (dashed lines). h is the normalized magnetic field by J along the x-direction. (b) Magnetic field derivatives of the magnetization ($\mathrm{d}m/\mathrm{d}h$) at designated γ. Quoted from [24].

$$ {}^4T_1 = \begin{cases} \frac{2}{3}\phi_0 - \frac{\sqrt{5}}{3\sqrt{2}}\left(\phi_3 - \phi_{-3}\right) = |0\rangle \\ \sqrt{\frac{5}{6}}\phi_2 - \frac{1}{\sqrt{6}}\phi_{-1} = |{+1}\rangle \\ \sqrt{\frac{5}{6}}\phi_{-2} + \frac{1}{\sqrt{6}}\phi_1 = |{-1}\rangle \end{cases} \tag{1-1-4} $$

where ϕ_m is the state of the orbital magnetic quantum number m of the total orbital angular momentum $\boldsymbol{L}$.

We calculate the matrix elements of L^z, which is the z component of the angular momentum of $L = 3$, for these three ground states

$$ \langle \pm 1|L^z| \pm 1\rangle = \mp\frac{3}{2} \tag{1-1-5} $$

$$ \langle 0|L^z|0\rangle = 0. \tag{1-1-6} $$

Therefore, the value obtained by multiplying the matrix element of l^z, which is the z component of the angular momentum of $l = 1$, is $-3/2$. These relations are the same for L^+ and L^-, and hence when considering only the orbital triplet in the orbital ground state, $L = 3$ angular momentum $\boldsymbol{L} = -(3/2)\boldsymbol{l}$ can be replaced by $l = 1$ effective angular momentum $\boldsymbol{l}$.

Usually, Co^{2+} ions are often placed in a tetragonal symmetric field or a trigonal symmetric field that is less symmetric from a cubic symmetry, but the magnitudes of these split widths are smaller than those by the cubic symmetry field and are similar to the magnitude of the spin-orbit interaction $\lambda'\boldsymbol{L}\cdot\boldsymbol{S}$. Therefore, the spin-orbit interaction and the uniaxial crystal field are combined and written in the following, and are considered to be perturbations for the ground state orbital triplet.

$$ \mathcal{H}' = -\frac{3}{2}\lambda'\boldsymbol{l}\cdot\boldsymbol{S} - \delta\left\{(l^z)^2 - \frac{2}{3},\right\} \tag{1-1-7} $$

where λ' is the spin-orbit coupling constant, and the second term represents the splitting by the tetragonal field where δ is the split width due to the uniaxial crystal field of ${}^4T_1$.

When the matrix elements of the angular momentum $\boldsymbol{l}$ and spin $\boldsymbol{S}$ are given by the eigenfunction of magnetic quantum number m_l and m_S $|m_l, m_S\rangle$, the matrix elements by $|m_l, m_S\rangle$ are equal to those by $|-m_l, -m_S\rangle$, and then double degeneracy remains. This is called the Kramers doublet, and the lowest electronic state is split into six Kramers doublets as a whole. The energy eigenvalues of these Kramers doublets are plotted as a function of δ/λ' in Fig. 1-1-6. The E_1 state in Fig. 1-1-6 always has the lowest energy, and the energy difference between the E_1 and the lowest excited states is about 10^2 K. Therefore, at low temperatures well below 100 K, the lowest energy state E_1 only have to be dealt with.

The doubly degenerate wave functions of the lowest energy state $\psi_\pm$ are expressed as follows:

$$ \psi_\pm = c_1\,|\mp 1, \pm\frac{3}{2}\rangle + c_2\,|0, \pm\frac{1}{2}\rangle + c_3\,|\pm 1, \mp\frac{1}{2}\rangle \tag{1-1-8} $$

Here, there is the following relationship between the coefficients c_1, c_2,and c_3.

$$ c_1^2 + c_2^2 + c_3^2 = 1 \tag{1-1-9} $$

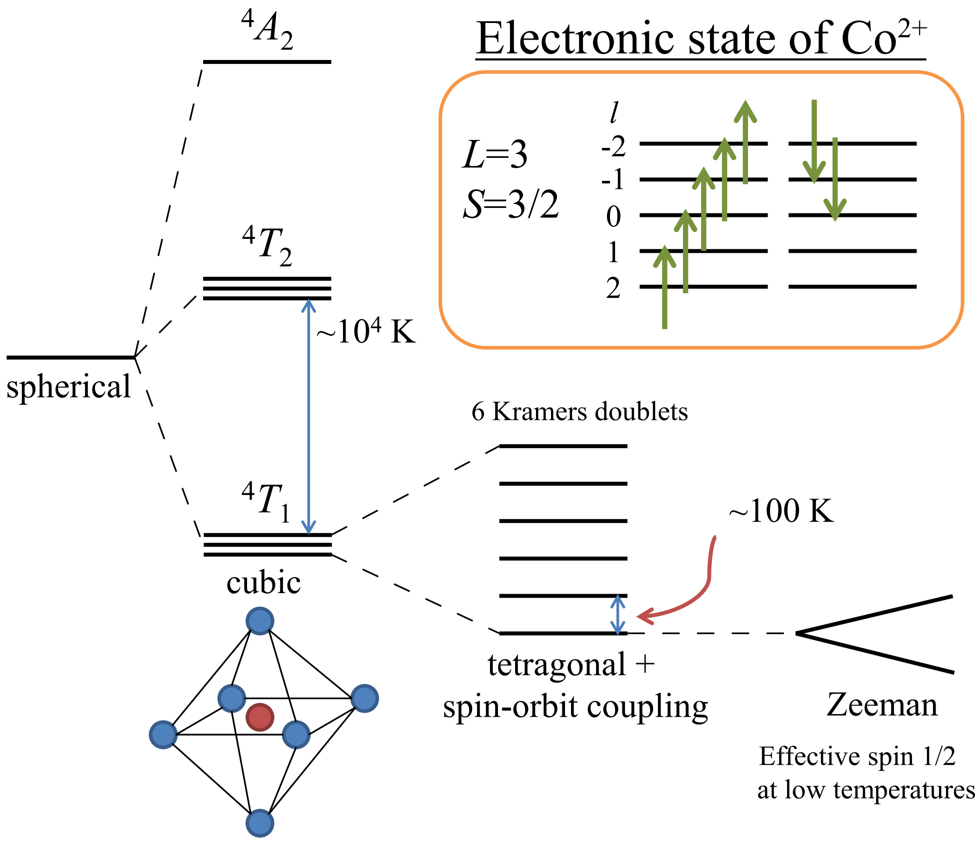

Figure 1-1-5: The electronic state of Co^{2+} ion in a tetragonal ligand-field surrounding. The effective spin of Co^{2+} ion becomes 1/2 well below 100 K.

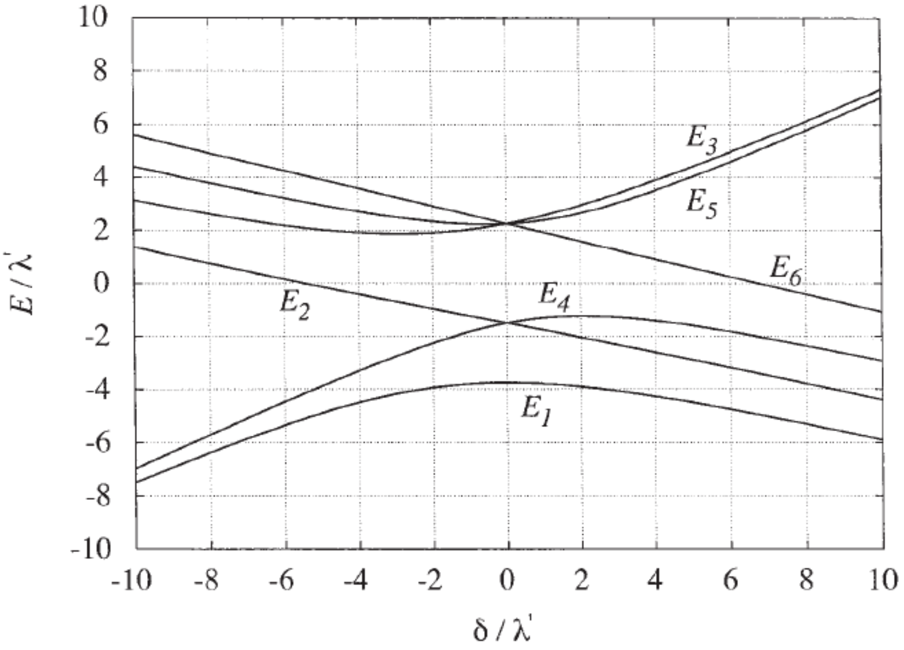

Figure 1-1-6: Crystal-field splitting of $^4T_1$ as a function of δ/λ'. δ and λ' are explained in the text. The six levels are doubly degenerate owing to time reversal symmetry. Quoted from [23].

The matrix elements of S^z and $S^\pm$ for $S = 3/2$ are written as,

$$\langle\psi_\pm|S^z|\psi_\pm\rangle = \pm\frac{1}{2}\left(3c_1^2 + c_2^2 - c_3^2\right) = \pm\frac{1}{2}p \tag{1-1-10}$$

$$\langle\psi_\pm|S^\pm|\psi_\mp\rangle = 2\left(\sqrt{3}c_1c_3 + c_2^2\right) = q \tag{1-1-11}$$

A pseudo spin (fictitious spin) s of 1/2 is introduced, and its z components $s^z = \pm 1/2$ correspond to the states $\psi_\pm$. The true spin $\boldsymbol{S}$ is expressed by the pseudo spin $\boldsymbol{s}$ like

$$S^x = qs^x, S^y = qs^y, S^z = ps^z. \tag{1-1-12}$$

Assuming that the exchange interaction $\mathcal{H}_{ex} = J\boldsymbol{S}_1 \cdot \boldsymbol{S}_2$ acts between the true spins $\boldsymbol{S}_1$ and $\boldsymbol{S}_2$ of two magnetic ions 1 and 2, the effective exchange interaction represented by the pseudo spin is described as follows:

$$\mathcal{H}_{ex} = J\left[p^2 s_1^z s_2^z + q^2\left(s_1^x s_2^x + s_1^y s_2^y\right)\right]. \tag{1-1-13}$$

Consequently, when $J > 0$ and $p^2 > q^2$, the system becomes an Ising-like antiferromagnet, and when $J > 0$ and $p^2 < q^2$, it becomes an XY-like antiferromagnet. Then, when $p^2 = q^2$, it becomes a Heisenberg antiferromagnet. Thus, the exchange interaction of Co^{2+} ion in an octahedral surrounding mostly becomes anisotropic for the effective spin $S = 1/2$.

1-2 $S = 1/2$ Two-Dimensional Antiferromagnet

1-2-1 Various types of $S = 1/2$ Two-Dimensional Antiferromagnets

There are several kinds of simple two-dimensional (2D) antiferromagnets with the nearest-neighbor (NN) exchange interaction. Here, we classify them by the coordination number z of exchange bonds: (i) $z = 3$: honeycomb-lattice antiferromagnet (bipartite) (HLA), (ii) $z = 4$: square-lattice antiferromagnet (bipartite) (SLA) and kagome-lattice antiferromagnet (non-bipartite) (KLA), and (iii) $z = 6$: triangular-lattice antiferromagnet (non-bipartite) (TLA). In these bipartite 2D antiferromagnets, no magnetic frustration occurs, while magnetic frustration occurs in the case of non-bipartite owing to the competition of exchange interactions caused by the geometry, the so-called geometrical frustration.

1-2-2 Honeycomb-Lattice Antiferromagnets

In this thesis, we focus on a HLA with the NN exchange interactions. The HLA has the minimum z among the 2D antiferromagnets, implying that quantum fluctuations must be larger than those in the SLA. When the next-nearest-neighbor (NNN) AF exchange interactions are included, the HLA system is expected to exhibit magnetic frustration. A recent theory predicted a rich phase diagram depending on the magnitudes of distant interactions (NNN and the third nearest-neighbor). Figure 1-2-1 shows the spin configurations and the phase diagram of the spin-1/2 J_1-J_2-J_3 honeycomb-lattice model given by,

$$\mathcal{H} = J_1 \sum_{<i,j>} S_i \cdot S_j + J_2 \sum_{<i,k>} S_i \cdot S_k + J_3 \sum_{<i,l>} S_i \cdot S_l, \tag{1-2-1}$$

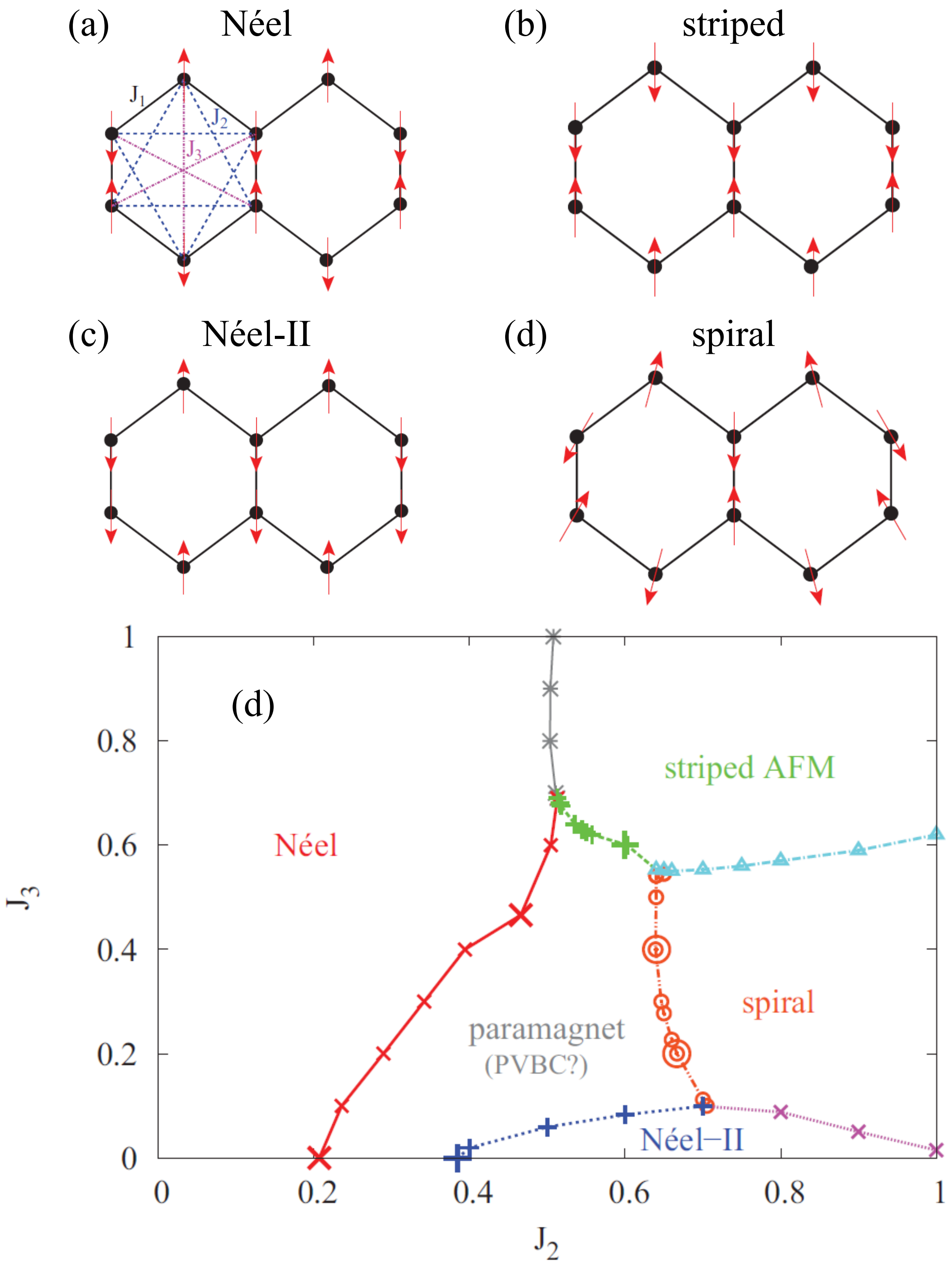

Figure 1-2-1: (a)–(d) Spin configurations of the spin-1/2 J_1-J_2-J_3 honeycomb-lattice model with $J_1 \equiv 1$, $J_2 > 0$, and $J_3 > 0$ where J_1, J_2, and J_3 represent the nearest-neighbor, the next-nearest-neighbor, and the third nearest-neighbor exchange interactions, respectively as depicted in (a). The spins on lattice sites (solid dots) are indicated by the red arrows. (e) Phase diagram of the spin-1/2 J_1-J_2-J_3 model on the HLA with $J_1 \equiv 1$ in the parameter window $J_2, J_3 \in [0, 1]$. Quoted from [37].

where S_i is the spin-1/2 operator at site i, J_1, J_2, and J_3 are the AF exchange constants between NN, NNN, and third nearest-neighbor spins, respectively, as depicted in Fig. 1-2-1(a) [37]. Various ground states were predicted.

The ground state of a HLA with anisotropic NN and identical NNN exchange interactions (Fig. 1-2-2(a)) was also investigated theoretically [38]. The phase diagram of the distorted HLA with the NN interaction are represented in Fig. 1-2-2(b). The spin Hamiltonian of this model is given by

$$\mathcal{H} = J_1 \sum_{<i,j>} S_i \cdot S_j + J_1' \sum_{<i,k>} S_i \cdot S_k + J_2 \sum_{<i,l>} S_i \cdot S_l, \tag{1-2-2}$$

where S_i is the quantum spin at site i, and the exchange constants J_1, J_1', and J_2 are indicated in Fig. 1-2-2(a). The distortion parameter δ and the frustration parameter α are defined by,

$$J_1 = \bar{J}_1(1-\delta) \tag{1-2-3}$$

$$J_1' = \bar{J}_1(1+2\delta) \tag{1-2-4}$$

$$\alpha = J_2/\bar{J}_1. \tag{1-2-5}$$

The $\bar{J}_1$ is an average of all the NN exchange constants $\bar{J}_1 = \frac{1}{3}(2J_1+J_1')$. The appearance of disordered phase or spin liquid state results from the magnetic frustration and the different NN exchange interactions owing to the bond distortion.

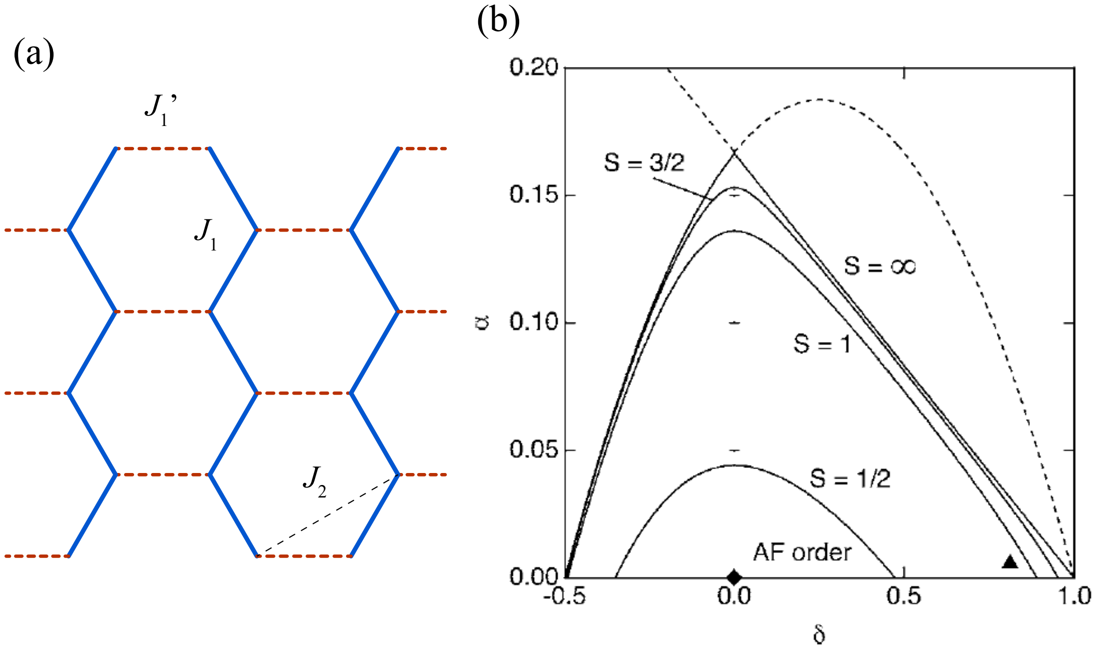

Figure 1-2-2: (a) The nearest-neighbor exchange interactions J_1 and J_1' are represented by the solid and the dashed lines, respectively. The next-nearest-neighbor interaction J_2 is represented by the thin dashed line. (b) Phase diagram in the space of the distortion parameter δ and the frustration parameter α for various quantum spin numbers. The details of δ and α are given in the text. Possible positions for $\mathrm{InCu_{2/3}V_{1/3}O_3}$ and $\mathrm{Na_3Cu_2SbO_6}$ are shown by diamond and triangle symbols, respectively. Quoted from [38].

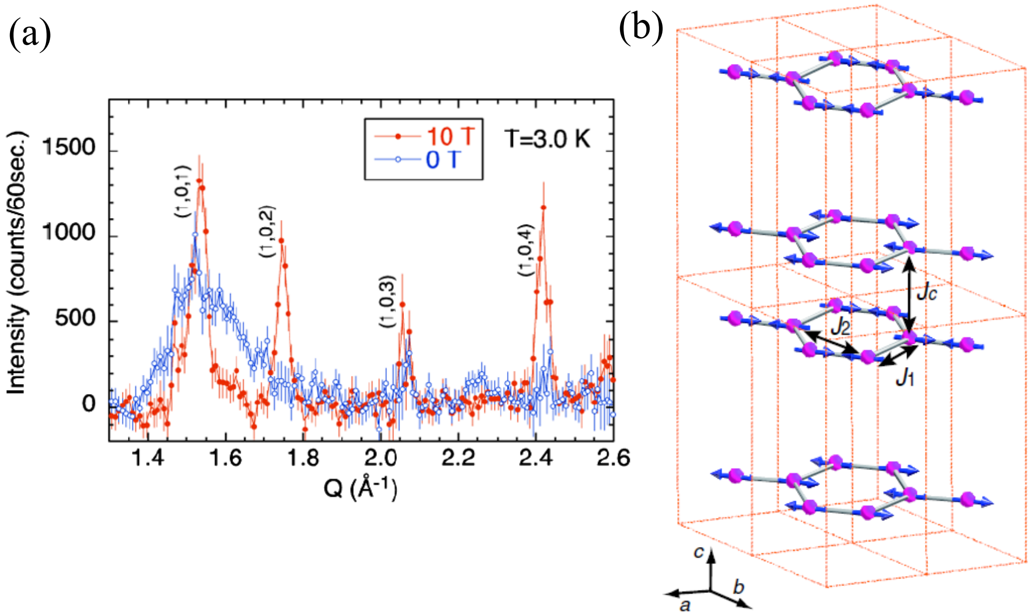

Figure 1-2-3: (a) Neutron powder diffraction patterns from $Bi_3Mn_4O_{12}(NO_3)$ at 0 T and 10 T and at 3.0 K. At 10 T, the broad magnetic peak is suppressed and sharp magnetic Bragg peaks appear. (b) Magnetic structure in the magnetic field-induced phase. Mn^{4+} ions in $2 \times 2 \times 2$ unit cells are represented. The magnetic moments lie in the *ab* plane, although the direction of the magnetic moments in the plane cannot be determined uniquely. J_1, J_2, and J_c indicate the nearest-neighbor, the next-nearest-neighbor exchange interactions, and the exchange interaction between the two adjacent honeycomb planes, respectively. Quoted from [44].

In contrast to the extensive theoretical investigations performed on HLAs, few inorganic honeycomb-lattice compounds have been reported to date. For example, in $In_3Cu_2VO_9$, the $Cu^{2+}(S = 1/2)$ ions form a honeycomb lattice that is well separated by InO_6 and VO_5 layers, thereby providing a clear two-dimensional character [39, 40]. This compound exhibits conventional Néel-type collinear AF long-range order (LRO) below 20 K [41]. As the second example, $Na_3Cu_2SbO_6$ possesses a honeycomb lattice of Cu^{2+} ($S = 1/2$) ions, but its magnetic properties are interpreted in terms of a spin-gapped antiferromagnetic-ferromagnetic bond alternating chain [42]. Another example is $Bi_3Mn_4O_{12}(NO_3)$ (Mn^{4+} ion, $S = 3/2$) which shows a disordered ground state at low temperatures [43] and an unusual field-induced LRO revealed by the neutron scattering experiment [44]. Figures 1-2-3(a) and 1-2-3(b) display the neutron powder diffraction pattern and the magnetic structure of $Bi_3Mn_4O_{12}(NO_3)$, respectively. Sharp magnetic Bragg peaks were observed when the external magnetic field was 10 T, whereas no such peaks were not observed at 0 T. The magnetic field versus temperature phase diagram of the frustrated HLA with NNN interaction for $J_2/J_1 = 0.18$ corresponding to the ratio in $Bi_3Mn_4O_{12}(NO_3)$ was calculated by Shimokawa and Kawamura as shown in Fig. 1-2-4 [45]. Above the temperature of $T/J_1 = 0.03$, a spin liquid state called the Pancake liquid is realized in zero magnetic field, and a field-induced AF short-range correlation develops by applying magnetic fields. Therefore, the field-induced AF LRO in $Bi_3Mn_4O_{12}(NO_3)$ was suggested to appear in this field-induced AF area with the help of interlayer interactions. These various magnetic properties in honeycomb-lattice compounds result not only from distant exchange interactions but also from the difference in the NN exchange interactions.

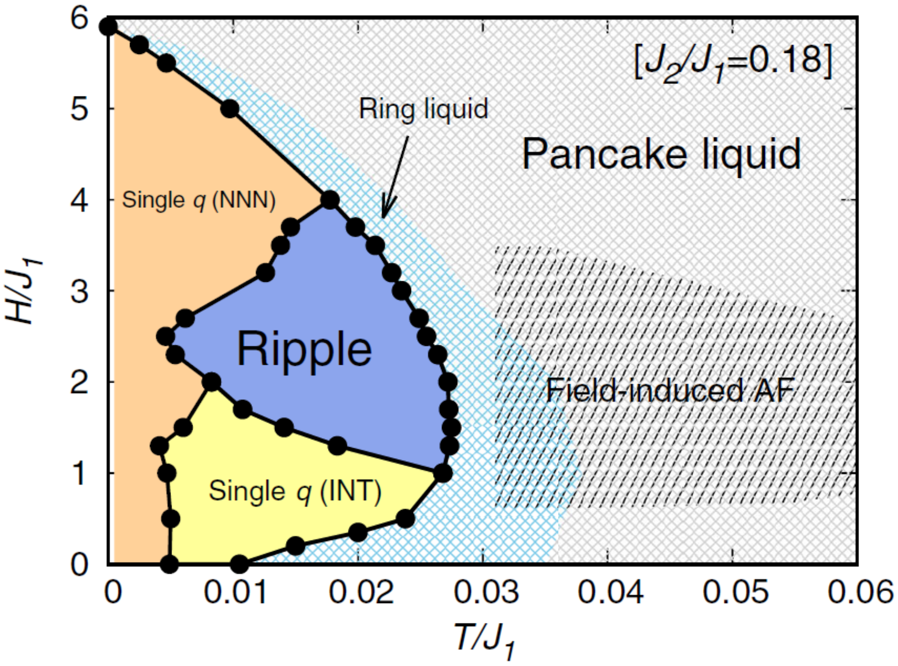

Figure 1-2-4: Phase diagram of a frustrated HLA for $J_2/J_1 = 0.18$ obtained by Monte Carlo simulations, where J_1 and J_2 are the NN and the NNN exchange constants, respectively. Above about $T/J_1 = 0.03$, the field-induced AF short-range correlation develops in magnetic fields. Quoted from [45].

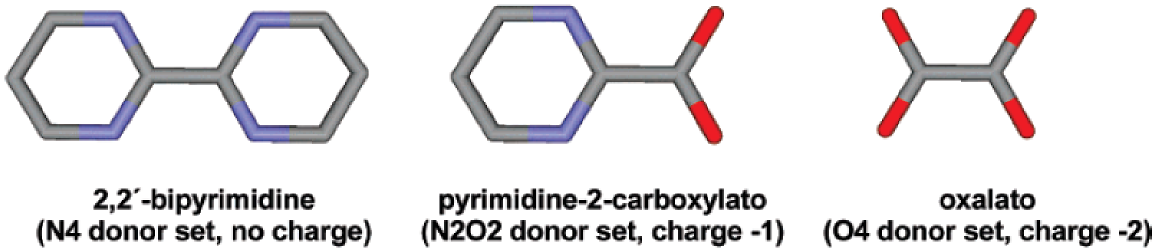

Figure 1-2-5: Schematic view of bridging ligands of 2,2′-bipyrimidine, pyrimidine-2-carboxylate, and oxalate. Quoted from [54].

Recently, a honeycomb lattice with bond-dependent exchange interactions J_x, J_y, and J_z has been extensively studied as a Kitaev model. Importantly, the Kitaev model has an exactly solvable spin liquid ground state [46], and gapless or gapped Majorana fermion excitations are expected to occur, depending on the parameters under the condition $J_\mathrm{x}+J_\mathrm{y}+J_\mathrm{z} = 1$. Since the theoretical study by Jackeli and Khaliullin [47], this Kitaev model has been expected to be realized in some Ir oxides and α-RuCl$_3$ [48, 49].

Using various types of organic (e.g. 2,2′-bipyrimidine, abbreviated as bpym) or inorganic (e.g. oxalate, abbreviated as ox) bridging ligands, a number of honeycomb-lattice molecule-based magnetic materials have been synthesized [50–53]. Pymca (pyrimidine-2-carboxylate) is an appropriate bridging ligand between bpym and ox that can be considered as one-half bpym and one-half ox, as shown in Fig. 1-2-5, to build a honeycomb-lattice structure. Honeycomb-layered metal complexes $[M_2(\mathrm{pymca})_3]\mathrm{OH}\cdot\mathrm{H_2O}$ (M=Fe^{2+}, Co^{2+}) were synthesized and their magnetic properties were investigated [54]. Later, we will report on these honeycomb-lattice compounds.

In this thesis, we study two kinds of low-dimensional antiferromagnets, the $S = 1/2$ 1D Ising-like antiferromagnet $\mathrm{BaCo_2V_2O_8}$ and the $S = 1/2$ 2D HLA $\mathrm{Cu_2(pymca)_3(ClO_4)}$ in high magnetic fields. The purposes and the details of the studies on these compounds will be described in Sect. 3 ($\mathrm{BaCo_2V_2O_8}$) and Sect. 4 ($\mathrm{Cu_2(pymca)_3(ClO_4)}$). In the next section, experimental apparatus and methods of these studies will be given.

2 Experimental Apparatus and Methods

In this study, we carried out magnetic susceptibility, magnetization, ESR, specific heat, and magnetostriction measurements on $BaCo_2V_2O_8$ and $Cu_2(pymca)_3(ClO_4)$. Some of the experimental apparatuses were commercially available, while the others were homemade. This chapter describes the details of the experimental apparatuses, especially homemade ones.

2-1 Magnetic Field Generation Method

The magnetic field generation methods are related to two types of magnetic fields, namely a pulsed magnetic field and a static magnetic field. The static magnetic field of about 1 T is generated with a permanent magnet. The generation of a magnetic field larger than 1 T is basically performed by an electromagnet. Examples of magnets for a static magnetic field are a water-cooled magnet ($\sim$ 33 T), a superconducting magnet ($\sim$ 32 T [55]), and a hybrid magnet ($\sim$ 45 T), which is composed of a water-cooled and a superconducting magnets. Magnets to generate a pulsed magnetic field are roughly divided into two types: destructive type and non-destructive type. Examples of the former magnetic field generation method include a single-turn coil method ($\sim$ 200 T), and two magnetic-field compression methods, namely, an electromagnetic flux compression ($\sim$ 1200 T [56]), and explosive flux compression ($\sim$ 2000 T).

A non-destructive multilayer pulse magnet devised and developed by Professor Koichi Kindo (The Institute for Solid State Physics, The University of Tokyo) was used to generate the magnetic field in this study. This is called a Kindo-pulse magnet. It is necessary to flow a large current in order to generate a high-magnetic field. The pulsed high-magnetic field used in this study is generated by instantaneously releasing the electrostatic energy stored in the capacitor as an electric current to the coil. When a large current flows in the coil, a huge electromagnetic stress is applied to the coil in the direction of outward expansion and vertical contraction. In addition, a large current generates a large Joule-heat and causes a temperature rise. Therefore, the wire used as the material of the coil is required to have high tensile strength and to be as low resistance as possible. CuAg (24 wt%) (cross-section area: 2×3 mm^2, tension strength: approximately 900 MPa) wire is used to satisfy the above requirements, and is wound in multiple layers to form a coil. Furthermore, the outside of the coil is reinforced with a high-strength Maraging steel cylinder to prevent deformation of the magnet due to electromagnetic stress as shown in Fig. 2-1-1(a). We employed nondestructive short pulse magnets with the duration time of $\sim$ 7 ms for magnetization and ESR measurements. The bore diameters of these magnets are 11 mm, 18 mm, or 22 mm. The magnet is immersed in liquid N_2 to reduce the electric resistance and to cool the magnet after the magnetic field is generated. The magnet is driven by the capacitor bank system as shown in Fig. 2-1-2. The magnet current is supplied sinusoidally by the capacitor bank, which can store charge energy of up to 1.5 MJ (20 kV, 7.5 mF), through the discharge of air-gap-type switch (start switch in Fig. 2-1-2). After a half of the period, the current is dumped into the crowbar circuit using a crowbar switch in Fig. 2-1-2 to avoid an additional Joule heating of the magnet. The magnitudes of the pulsed magnetic field depending on the number of capacitor banks and the changing voltage are shown in Fig. 2-1-1(b). We can control the duration time by changing the number of the capacitor banks (at most six banks). The duration time is proportional to $\sqrt{LC}$, where L and C are the inductance of the pulse magnet and the capacitance of the capacitor banks, respectively. In this study, we used pulse magnets capable of generating magnetic fields of up to 70 T.

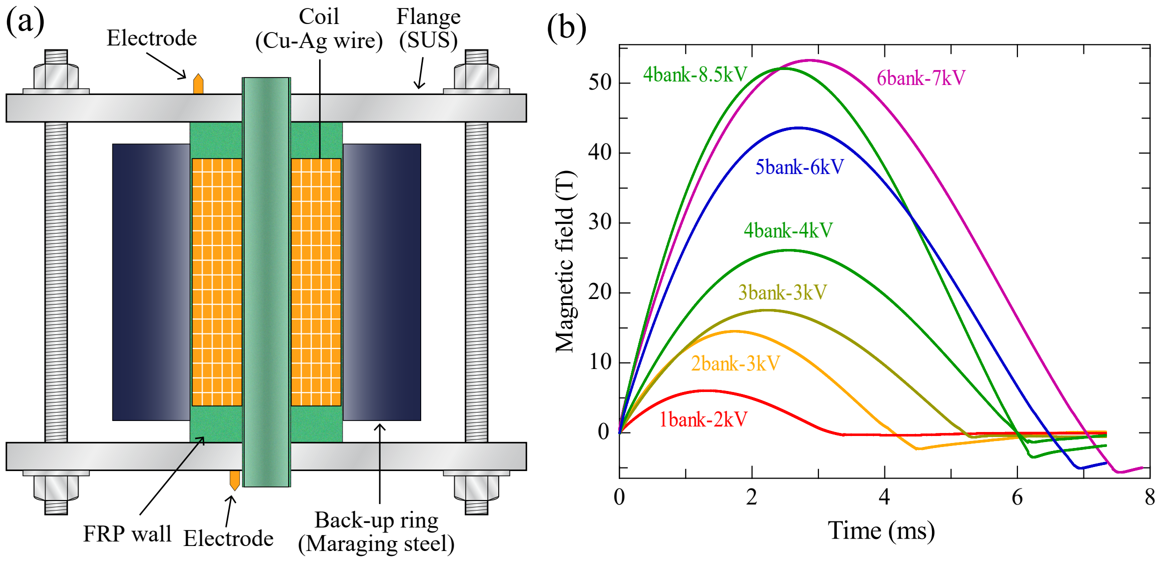

Figure 2-1-1: (a) Schematic cut view of a pulse magnet. The magnet is held by stainless steel flanges. (b) Typical pulsed magnetic-field shapes generated by a pulse magnet. These are produced by using six banks with 7 kV voltage, five with 6 kV, four with 8.5 kV, four with 4 kV, three with 3 kV, two with 3 kV, and one with 2 kV, respectively.

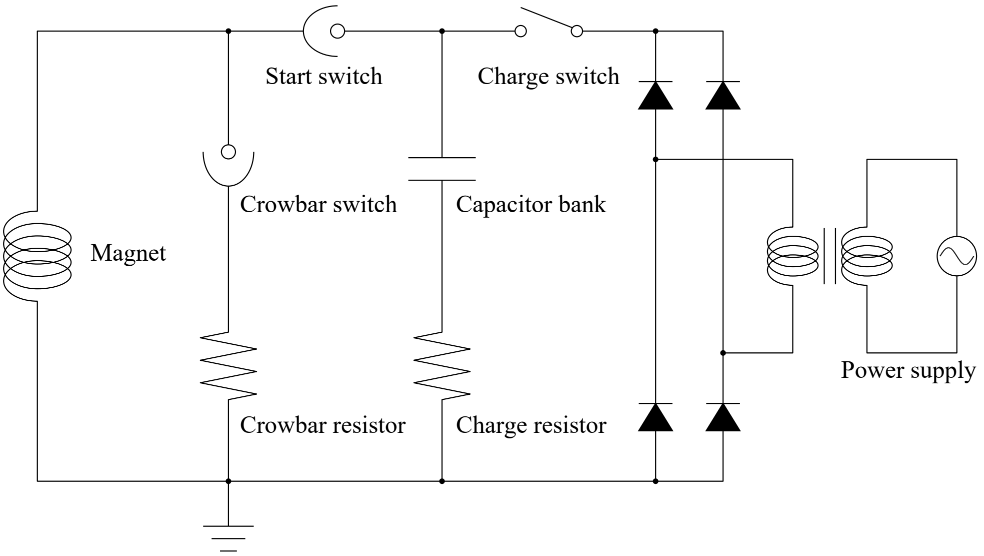

Figure 2-1-2: Schematic view of the circuit of pulse field generation system using the capacitor bank.

2-2 Magnetic Measurements (Susceptibility, Magnetization)

2-2-1 Magnetic Susceptibility and Magnetization Measurements in Static Magnetic Fields

Magnetic susceptibility χ ($= M/H$ where M magnetization and H magnetic field, 0.1 T) and magnetization up to 7 T were measured with a commercial SQUID magnetometer (MPMS-XL7, Quantum Design, USA). The measurements were conducted in the temperature range 1.9 K–350 K.

2-2-2 Magnetization Measurements in Pulsed Magnetic Fields

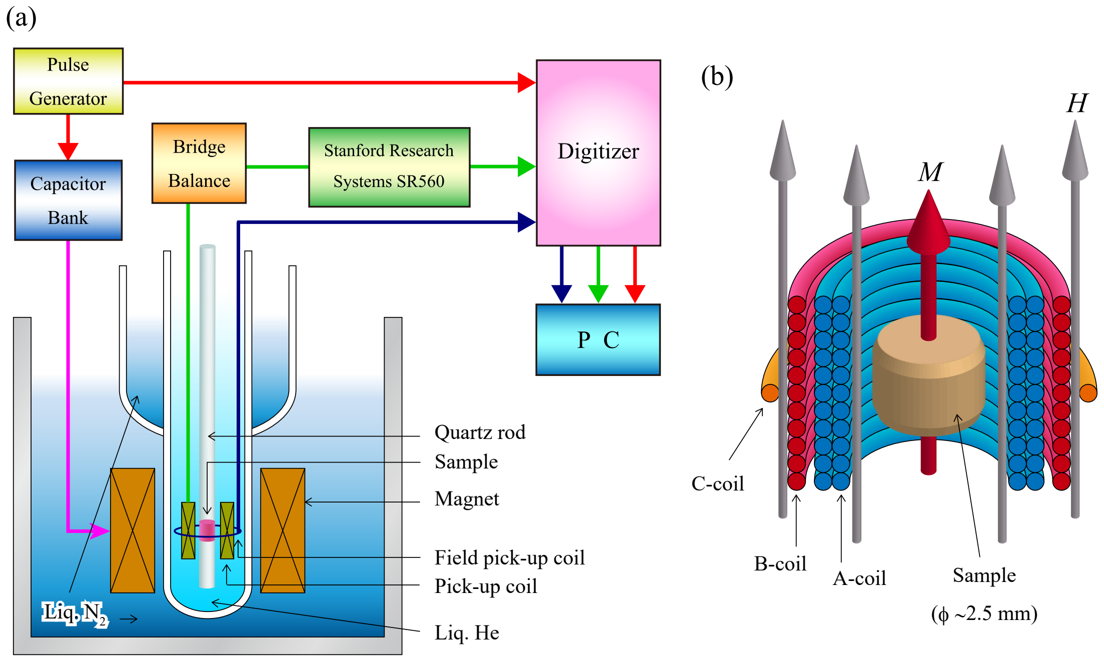

Figure 2-2-1: (a) Block diagram of pulsed field magnetization measurement system. (b) Cut view of a co-axial type pick-up coil system (M: magnetization and H: magnetic field).

We performed high-field magnetization measurements with a pulse magnet by an induction method using a pick-up coil up to almost 70 T at 1.4 K and 4.2 K. Figure 2-2-1(a) depicts the block diagram of the high-field magnetization measurement system in pulsed magnetic fields. The technique of reducing the background flux change due to a transient field, which is usually $10^4 \sim 10^6$ times larger than the flux change caused by the magnetization of the target sample, is shown schematically in Fig. 2-2-1(b). The A-coil picks up the magnetic flux changes and the external field while the B-coil is wound oppositely to the A-coil in order to compensate the background flux change. A fine adjustment is established with the one turn C-coil. Considering the field duration and frequency response, the A-coil is wound with 80 turns on a 3.0 mm diameter Bakelite pipe. The B-coil is wound with 40 turns coaxially on the A-coil on a 4.3 mm diameter in opposite direction to the A-coil. The C-coil is wound with one turn coaxially on the others. The cross section of the B-coil is twice as large as that of the A-coil so as to receive the same amount of external flux in the two coils. In this way, we can obtain only an induced voltage coming only from a magnetization of the sample. We obtain the magnetization signals as $\mathrm{d}M/\mathrm{d}t$. The field and magnetization pick-up coils were calibrated by a single crystal of $\mathrm{MnF_2}$ as the standard specimen using the known values of the spin-flop transition field and the slope of the magnetization above the transition. The measurements at low temperatures down to 1.4 K were performed by pumping liquid ^{4}He. Magnetization up to 7 T measured by MPMS was used for calibration of the magnetization obtained in the pulsed-field measurement.

2-3 Electron Spin Resonance (ESR) Measurements

Three types of the ESR measurement systems were used in this study. One is an X-band ESR apparatus, which is a commercial ESR spectrometer (Bruker, USA) for the precise measurement of the temperature dependent ESR spectra at 9.3 GHz. The second one is a multi-frequency ESR apparatus that consists of a superconducting magnet, a vector network analyzer and Gunn oscillators as microwave sources. The last one is a high-field multi-frequency ESR apparatus that is composed of a pulse magnet, an InSb detector, and microwave sources such as a far infrared (FIR) laser, Gunn oscillators and a backward wave oscillator. The latter two ESR apparatuses, which are home-made, are described below.

2-3-1 ESR Measurements in Static Magnetic Fields

The ESR measurements in static magnetic fields were performed up to 14 T at 1.5 K. ESR measurement system in static magnetic fields consists of a 16 T superconducting magnet (Oxford Instruments, UK) and a vector network analyzer (MVNA-8-350, AB Millimeter, France) with high frequency ESA(External Source Association)-1 and ESA-2 extensions up to 700 GHz as shown in Fig. 2-3-1. Normally, the superconducting magnet is cooled down to 4.2 K with liquid He and used in the magnetic field range of up to 14 T. When using a λ-refrigerator, magnetic field up to 16 T can be generated. A variable temperature insert (VTI) is used to change the temperature of the sample space from 1.5 K to 300 K. The sample space temperature is monitored by using a calibrated cernox resister thermometer placed close to the sample, and is controlled by a heater of Manganin-wire. In the region of 30 GHz–150 GHz, the optical element is irradiated with electromagnetic waves from the internal source of MVNA, and the multiplied waves generated there are used for the measurements. In the region above 150 GHz, the output power of the multiplied wave is weakened by the above method, and thus the Gunn oscillators Gunn1: 68 GHz–82 GHz and Gunn2: 82 GHz–102 GHz, which have a high transmission frequency band, are used. Since the frequency of the electromagnetic wave transmitted from the Gunn oscillator is unstable, feedback control is performed with reference to the stable electromagnetic waves from MVNA internal source to fix the transmission frequency. MVNA detects the microwaves through the sample. Since not only the amplitude but also the phase of the ESR signal measured with the MVNA, the resonance magnetic field can be precisely determined even if the dispersion component of the ESR signal is mixed with the absorption one and the absorption waveform is deformed. The Gunn oscillator A of ESA-1 sends its emitted microwave frequencies F_A into the Schottky multiplier (SM). Non-linear effects due to the Schottky diode create harmonic frequencies $m \times F_{\mathrm{A}}$ (m: integer), and one of these harmonics is selected for the experiments. At the same time, the Gunn oscillator B of ESA-2 sends its emitted microwave frequencies F_{B} into the the Schottky Harmonic Mixer (SHM), which also creates harmonic frequencies $m \times F_{\mathrm{B}}$. Then the difference frequency $m \times (F_{\mathrm{A}} - F_{\mathrm{B}})$, which can be easily extracted and amplified, is detected. The ESR spectra for two different frequencies (dual frequency option) can be observed at the same time when we have receivers for two frequencies $m \times (F_{\mathrm{A}} - F_{\mathrm{B}})$ and $(m-1) \times (F_{\mathrm{A}} - F_{\mathrm{B}})$ which are usually radio frequencies (the order of 10 MHz). Microwaves are injected into the sample in a cryostat which is made of stainless steel light pipes with the diameter of 8 mm. A thin stainless steel jacket is used to avoid the noise from a bubbling of liquid He. The microwaves for the frequency from about 30 GHz to about 700 GHz can be generated almost continuously. Both Faraday ($k \parallel H$, k: light vector) and Voigt ($k \perp H$) configurations can be used and are selected according to the setting depends on the shape and the crystallographic directions of the sample.

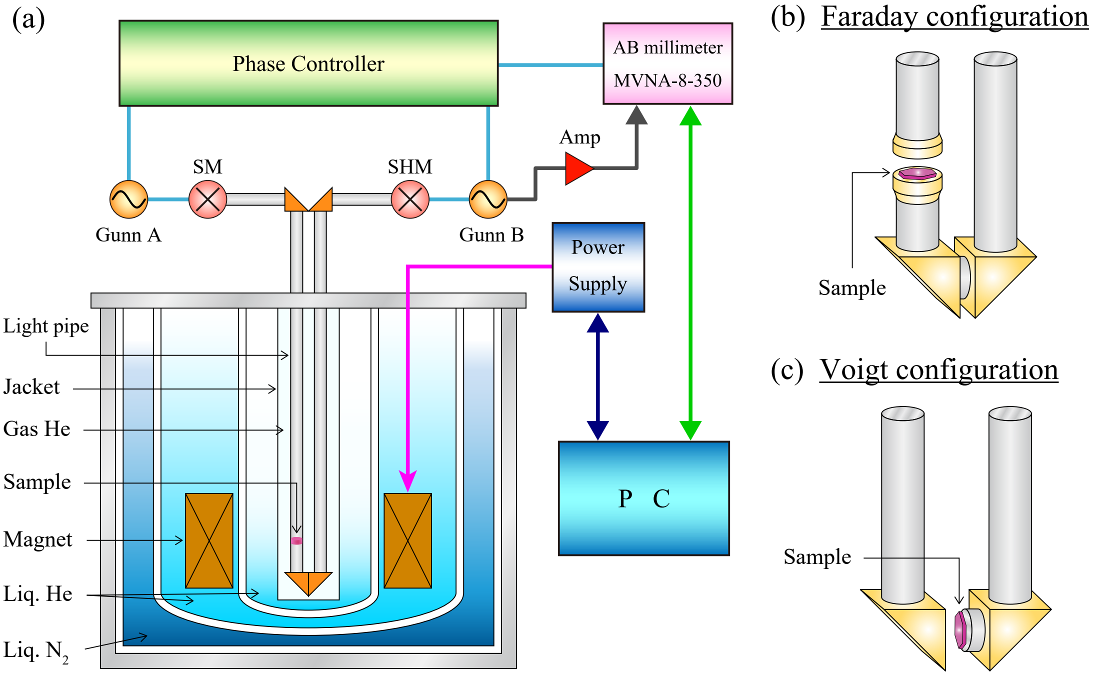

Figure 2-3-1: (a) Block diagram of ESR measurement system in static magnetic fields, which is composed of a vector network analyzer and a 16 T superconducting magnet. Sample setting for (b) Faraday and (c) Voigt configurations.

2-3-2 ESR Measurements in Pulsed Magnetic Fields

We performed the ESR measurements in pulsed magnetic fields of up to 53 T at 1.4 K. Figure 2-3-2 shows the block diagram of the ESR measurement system in pulsed magnetic fields which is composed of a nondestructive short pulse magnet, an InSb hot electron bolometer (QMC Instruments Ltd., UK), and a variety of light sources, such as a FIR laser (Edinburgh Instruments, UK), Gunn oscillators, and a backward wave oscillator (CDP Systems Corp., Russia). Microwaves at frequencies from about 300 GHz to about 2.0 THz are generated with a FIR laser, which is excited by a CO_2 pumping laser and produces many various frequencies by changing molecular gases such as a methanol and formic acid, and those at frequencies below 300 GHz are obtained by using several Gunn oscillators with doubler (75, 90, 110, 130, 150, 180, 220, 260 GHz) and a backward wave oscillator (BWO) (250 GHz–500 GHz). ESR signals are detected with an InSb hot electron bolometer which is magnetically tuned to offer optimized sensitivity over the maximum possible range of frequencies between millimeter and sub-millimeter wavelengths. Microwaves are injected into the sample in a cryostat which is made of stainless steel light pipes with the diameter of 4 mm. The light pipe itself acts as a jacket and avoids the noise from a bubbling of liquid He. The measurements are performed at low temperatures down to 1.4 K by pumping liquid ^{4}He. In pulsed field ESR measurements, a powder of 2,2-Diphenyl-1-picrylhydrazyl (DPPH) with $g = 2.0036$ (g-factor), which is a kind of free radical molecule with unpaired electrons, is used as a magnetic field calibration standard. Like the static field ESR system, both Faraday and Voigt configurations can be used.

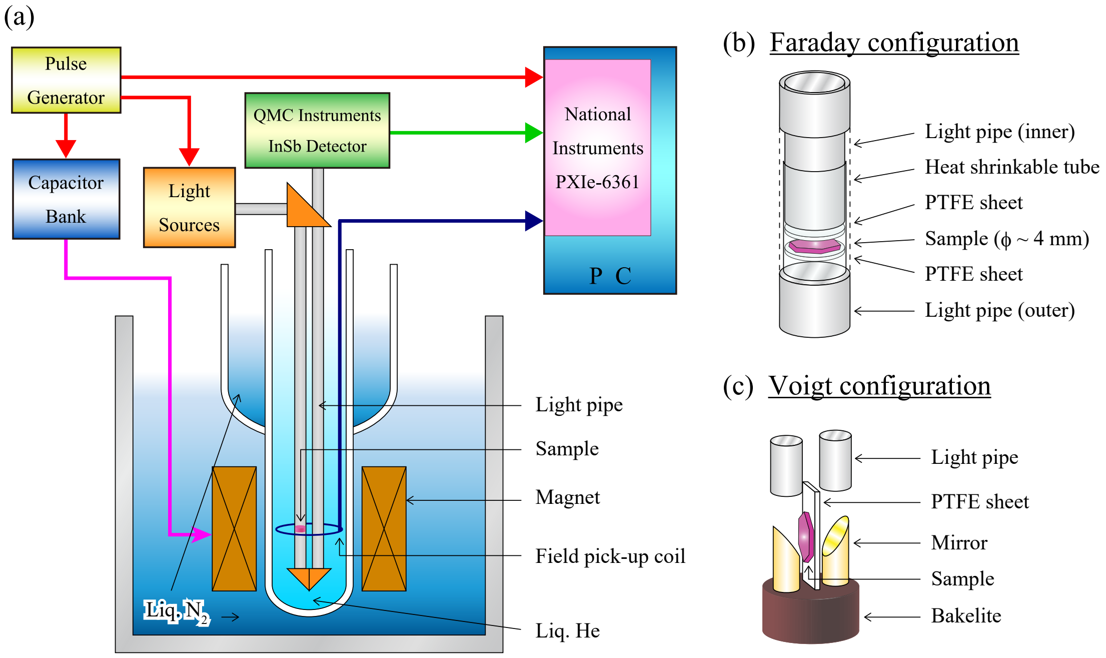

Figure 2-3-2: (a) Block diagram of pulse field ESR measurement system. (b) Faraday and (c) Voigt configurations in the pulse field ESR measurements.

2-4 Specific Heat Measurements

Two types of the specific heat measurement system were used in this study. One is a commercial Physical Properties Measurement System with a ^{3}He refrigerator (PPMS, Quantum Design, USA) using a relaxation method at temperatures down to 0.6 K. The other consists of a homemade cryostat down to 1.4 K and a superconducting magnet up to 9 T by the thermal relaxation method.

In Fig. 2-4-1(a), a schematic diagram of the sample setting on the addenda in a homemade cryostat is depicted. The size of the addenda is 5 mm square and the thickness is 0.05 mm. The addenda is hung by wires to avoid thermal contact with the surroundings as much as possible. These hanging wires double as the wiring to the heater and thermometer on the back of the addenda, as shown Fig. 2-4-1(b).

Figure 2-4-2 shows the sequence for performing the specific heat measurements. Assuming that the current passing through the heater is I_0 and the temperature at that time is T_0, when the current of $I_0 + \Delta I$ is passed through the heater, the temperature rises accordingly. After Δt, the current passing through the heater returns to I_0, and thus the temperature begins to drop from $T_0 + \Delta T$. The specific heat can be obtained by fitting the curve obtained after this time with a function that takes the relaxation into consideration. After the measurement at temperature T_0 is completed in this way, the current is set to I_1 so that the temperature becomes T_1. After that, when the temperature becomes stable at T_1, the above measurement sequence is performed. By repeating these procedures, the temperature dependence of the specific heat can be obtained.

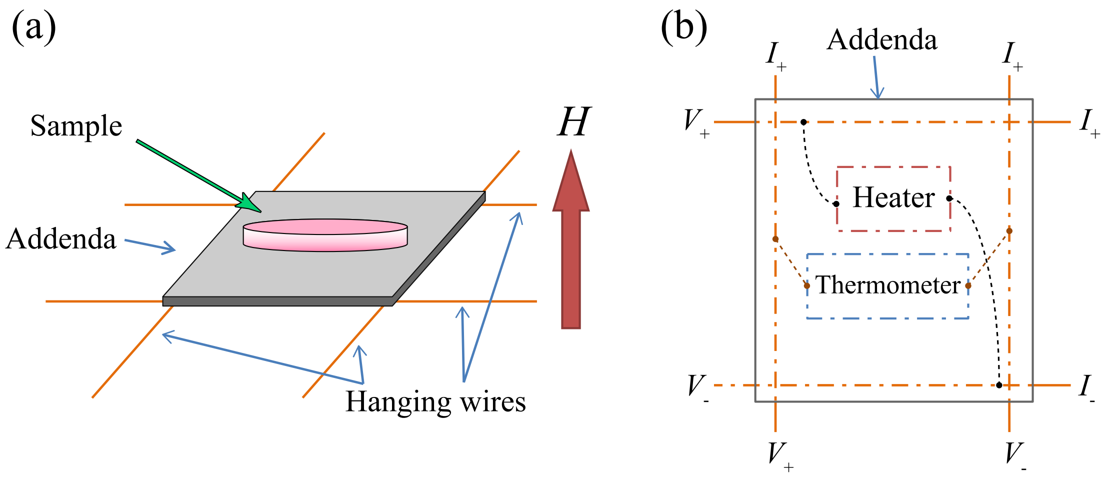

Figure 2-4-1: (a) Schematic diagram of the sample setting for the specific heat measurements. The cell is installed in the cryostat into the superconducting magnet. (b) Wiring diagram to the addenda. Those located behind the addenda are indicated by broken lines.

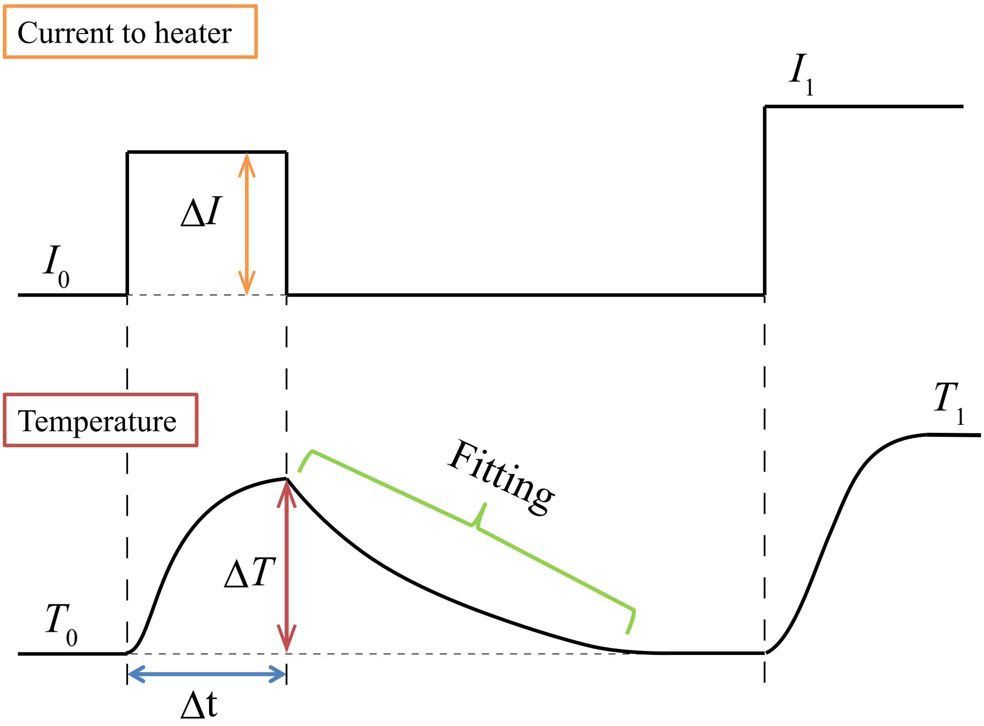

Figure 2-4-2: Sequence of the specific heat measurement by the relaxation method.

2-5 Magnetostriction Measurements

Magnetstriction data at 1.4 K in magnetic fields of up to 55 T were taken at the Institute for Solid State Physics, The University of Tokyo by using a pulse magnet, a capacitance bridge (1615A, General Radio, USA) and a home made dilatometer by a capacitance method [57]. Figure 2-5-1(a) draws a schematic view of the capacitance dilatometer for the magnetostriction measurements. The cell inside the cryostat consists of a sample stage, a cylinder, a piston, and two electrodes. The sample with polished parallel-flat surfaces and the width of several millimeters is fixed to a sample stage with a diameter of 8 mm using the adhesive Stycast 1266. Then, a 6 mm-diameter gold-deposited quartz disc as an electrode is fixed on the opposite side of the sample. The other electrode is glued to the piston, and the two electrodes are placed inside the cylinder facing each other, and then the sample stage, the cylinder, and the piston are fixed by the Stycast. At this time, two Kapton sheets with the thickness of 12.5 μm are sandwiched between electrodes in order to maintain an appropriate gap. The Kapton sheets are removed when the adhesive becomes dried and hardened. After that, the cell is attached to the probe, and wiring is made and the setting is completed. In this device, the change in the electric capacitance between the electrodes caused by the change in the sample length in magnetic fields is detected with the capacitance measuring system as shown in Fig. 2-5-1(b). By this method, highly sensitive magnetostriction measurements with about $\Delta L/L \sim 10^{-6}$ is possible.

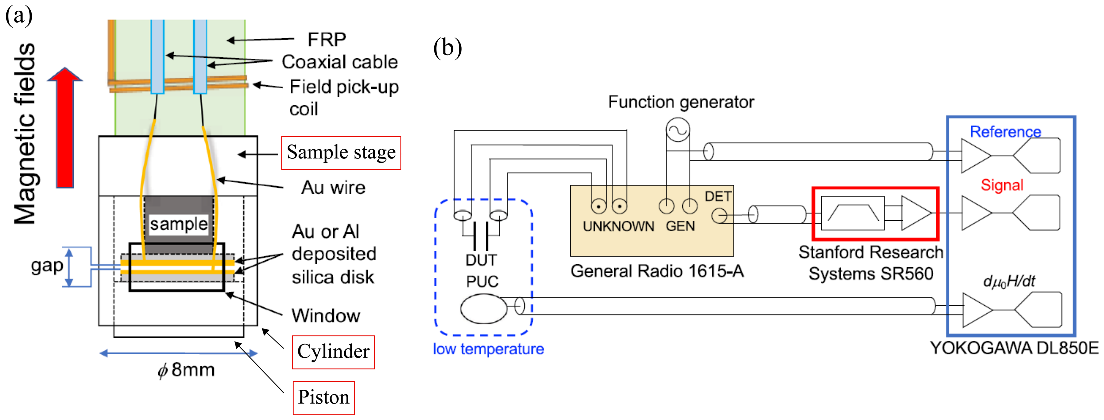

Figure 2-5-1: (a) Schematic illustration of the capacitance dilatometer for the magnetostriction measurements. (b) Schematic block diagram of the capacitance measuring system in pulsed fields. A sample, namely, a device under test (DUT) and a field pick-up coil (PUC) are located in a cryostat. Quoted from [57].

3 $S = 1/2$ Quasi-1D Antiferromagnet $BaCo_2V_2O_8$

3-1 Introduction

3-1-1 Fundamental Properties (Crystal Structure, Low-Field Magnetism)

$BaCo_2V_2O_8$ possesses a quasi-1D structure separated by nonmagnetic Ba^{2+} and V^{5+} ions as shown in Fig. 3-1-1, where edge-shared CoO_6 octahedra form a screw-chain rotating around the four-fold c-axis [25]. It belongs to a tetragonal system (space group $I4_1/acd$ with lattice constants $a = 12.4441(6)$ Å and $c = 8.4153(10)$ Å). Co^{2+} ions ($3d^7$) work as an effective spin $S = 1/2$ owing to the combined effects of a crystalline field and a spin-orbit coupling in octahedral surrounding, and the g-values show large anisotropy [35, 36]. Therefore $BaCo_2V_2O_8$ is usually regarded as an Ising-like chain. A magnetic phase transition occurs at 5.4 K at zero magnetic field [27]. On applying magnetic fields along the c-axis, a magnetic order to disorder transition was observed at a moderately low critical field around 4 T below approximately 2 K [27, 59], and an incommensurate spin-density-wave state was identified above the critical field below approximately 1 K [60–63], in agreement with the theory for the $S = 1/2$ quasi-1D Ising-like antiferromagnet. In subsequent studies on the effect of transverse magnetic fields, peculiar anisotropic behavior has been observed. The magnetization reaches the saturation near 40 T for $H \parallel [110]$. In sharp contrast, for $H \parallel [100]$, the magnetization is not saturated in magnetic fields of up to 50 T as shown later, and a phase transition

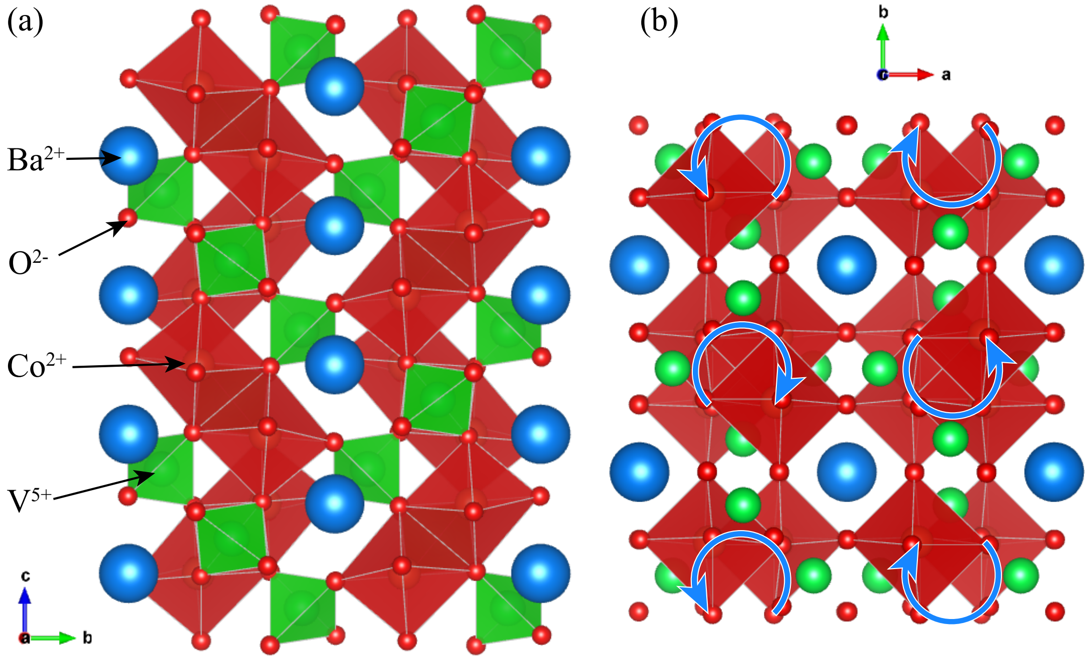

Figure 3-1-1: Crystal Structure of $BaCo_2V_2O_8$ [25], drawn by using the VESTA software program [58]. (a) The picture is the view projected from the a-axis to the bc-plane. (b) The picture is the view projected from the c-axis to the ab-plane. The arrows indicate the rotational directions of the screw chains when proceeding to the c-axis direction.

takes place near 10 T [64–66]. In order to understand these anisotropic behaviors, an effective spin model including four-site periodic effective fields was suggested [65]. Magnetic excitations were discussed based on the effective model [67, 68]. Moreover, the 1D quantum critical point (QCP) was found other than the 3D QCP [69, 70], and the E_8 particles were observed at the 1D QCP by neutron scattering and NMR experiments [71] and THz spectroscopy [72].

Figure 3-1-2(a) shows the temperature dependences of the magnetic susceptibility $\chi = M/H$ (where M is the magnetization and H is the external magnetic field) for $H \parallel c$ and $H \perp c$ at 1 T. The magnetic susceptibility for $H \parallel c$ shows a broad maximum near 30 K, which is typical of a low-dimensional antiferromagnet, and a steep decrease below $\sim$ 5 K indicates the magnetic phase transition from a disordered state to an ordered one for $H \parallel c$. In contrast, the magnetic susceptibilities for $H \perp c$ increase gradually with decreasing temperature and a small hump appears near 30 K, and then, a cusp is observed at approximately 5 K. Therefore, $\mathrm{BaCo_2V_2O_8}$ possess a large magnetic anisotropy and the c-axis is the easy-axis. Figure 3-1-2(b) displays the magnetization as a function of applied magnetic field parallel and perpendicular to the c-axis below 90 kOe at 2 K. When the magnetic field is applied perpendicular to the c-axis, the magnetization increases almost linearly with respect to the magnetic field, whereas an abrupt increase in the magnetization is observed at around 4 T when the magnetic field is applied parallel to the c-axis.

The temperature dependences of the specific heat at various magnetic fields are given in Fig. 3-1-3 [27, 28]. At zero magnetic field, the AF order occurs at the Néel temperature $T_{\mathrm{N}} = 5.4$ K. When a magnetic field is applied in the perpendicular direction to the c-axis, the phase transition temperature does not change so much with respect to the magnetic field, whereas the phase transition temperature decreases largely as the magnetic field increases when the magnetic field is applied parallel to the c-axis.

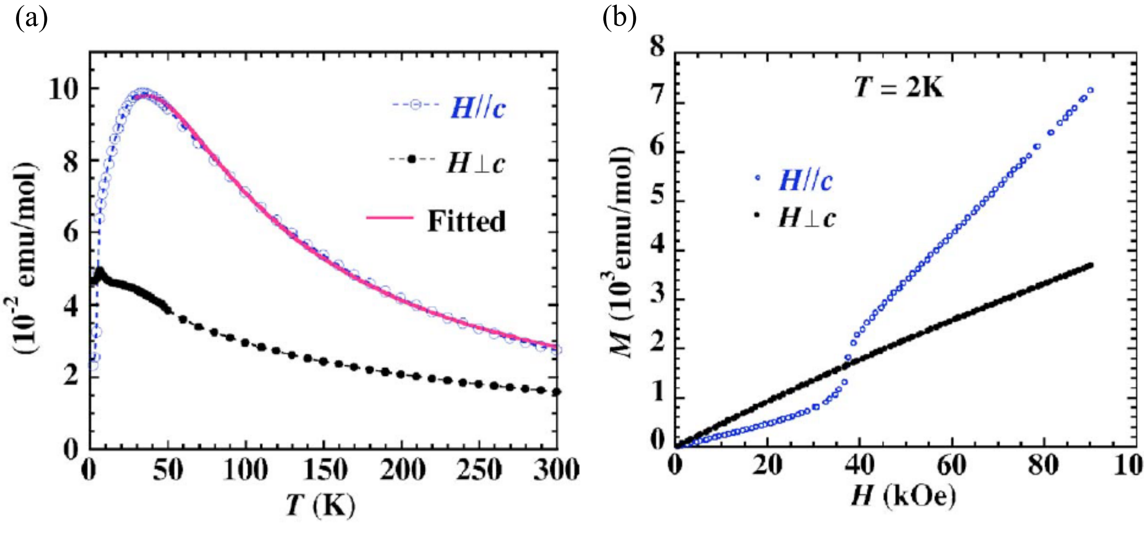

Figure 3-1-2: (a) Temperature dependences of the magnetic susceptibility $\chi(= M/H)$ for $H \parallel c$ and $H \perp c$ at 1 T. (b) Low field magnetization up to 90 kOe for $H \parallel c$ and $H \perp c$ at 2 K. Quoted from [27].

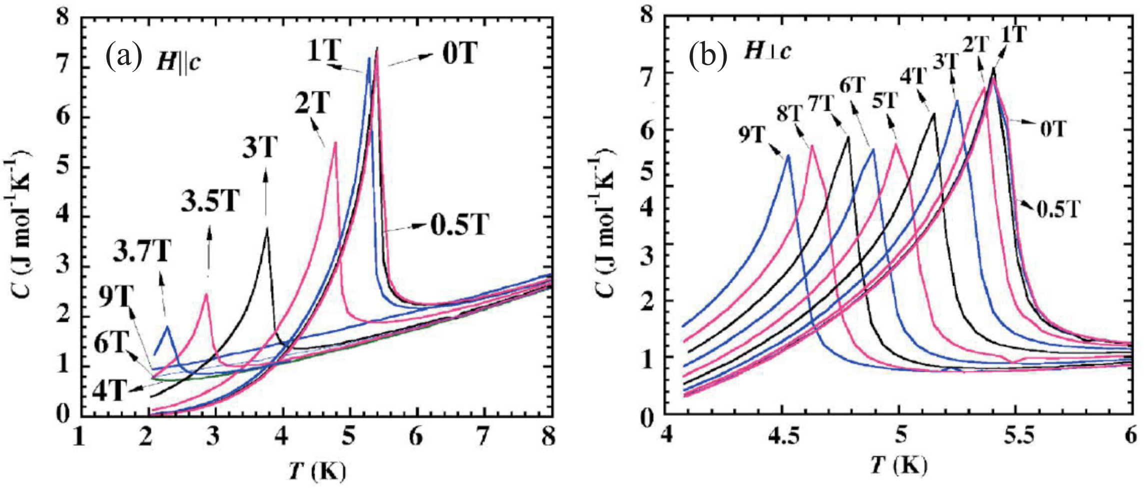

Figure 3-1-3: Temperature dependences of the specific heat at indicated various magnetic fields for (a) $H \parallel c$ and (b) $H \perp c$. Quoted from [27, 28].

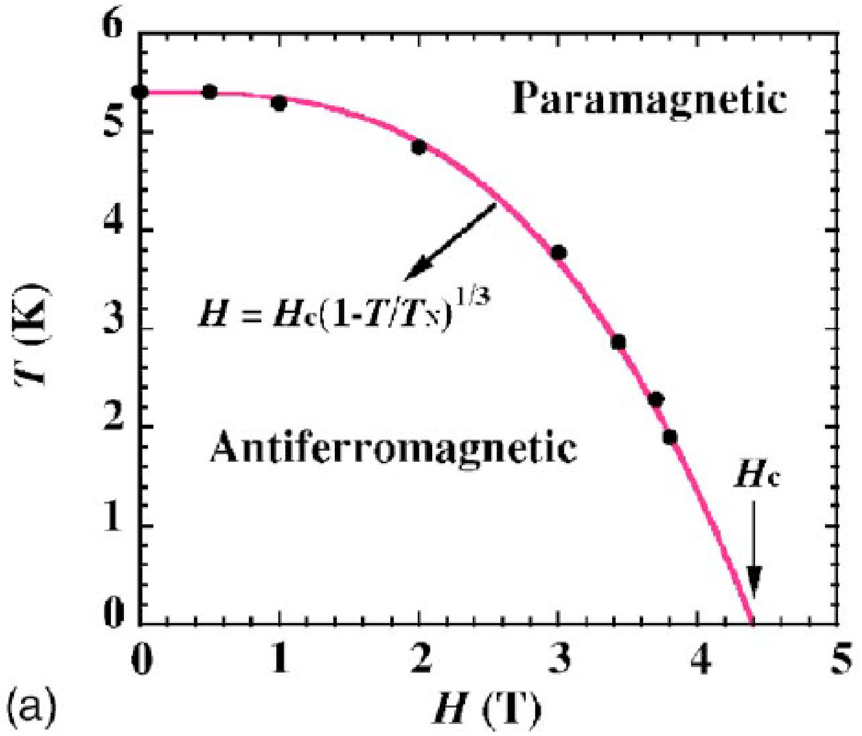

Figure 3-1-4: Magnetic phase diagram (temperature versus magnetic field) for $H \parallel c$. Quoted from [27].

Figure 3-1-4 represents the magnetic phase diagram (temperature versus magnetic field) for $H \parallel c$ obtained from the specific heat measurements. In $\mathrm{BaCo_2V_2O_8}$, the magnetic field parallel to the c-axis induces the phase transition from the ordered state to the disordered state below T_N. The solid line is the fitting curve using the formula $H = H_\mathrm{c}\,(1 - T/T_\mathrm{N})^{1/3}$ as indicated in the figure, and H_c is the critical field at $T = 0$ K.

3-1-2 High-Field Magnetism in Longitudinal Magnetic Fields

Figure 3-1-5 shows the high-field magnetization curve of $\mathrm{BaCo_2V_2O_8}$ at 1.3 K, measured in pulsed magnetic fields for $H \parallel c$ and the theoretical curve based on the Bethe ansatz exact theory [30]. Three peaks of the field derivative of the magnetization are observed. One of them, the transition magnetic field $H_\mathrm{c} = 3.9$ T, is consistent with the results of specific heat measurements in Ref. 27. The peak at $H_\mathrm{s} = 22.7$ T indicates the saturation magnetic field to the field-induced ferromagnetic phase, and the middle peak at $H_\mathrm{c}^{'} = 19.5$ T is the magnetic field where the magnetization is a half of the saturation value. The magnetization curve has a downward convex shape below H_s, implying that the influence of quantum fluctuations is strong. The linear increase of the magnetization above H_s is considered to the Van-Vleck paramagnetic contribution. This magnetization curve can be well explained by $S = 1/2$ 1D XXZ model. The effective spin Hamiltonian of the $S = 1/2$ 1D XXZ model is given by

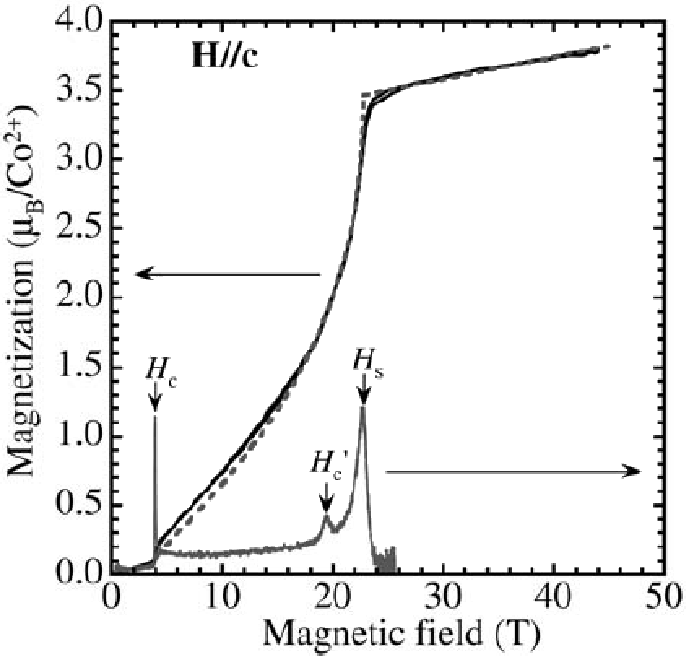

Figure 3-1-5: High field magnetization curve and the field derivative of the magnetization at 1.3 K for $H \parallel c$. Solid and dashed curves are experimental and theoretically calculated magnetization, respectively. Quoted from [30].

$$\mathcal{H} = J \sum_j \left\{ S_j^z S_{j+1}^z + \varepsilon \left(S_j^x S_{j+1}^x + S_j^y S_{j+1}^y \right) \right\} - g_z \mu_\mathrm{B} H_z \sum_j S_j^z \qquad (3\text{-}1\text{-}1)$$

where S_j^α is the spin-1/2 operator at site j for α (x or y or z) direction, J is the AF exchange constant between the nearest-neighbor spins, ε (< 1) is an Ising-like anisotropy parameter, μ_B is the Bohr magneton, g_z is the g-factor along the z-axis, and H_z is the external magnetic field applied along the z direction. The parameters used to reproduce the magnetization curve are $J/k_B = 65$ K, $\varepsilon = 0.46$, and $g_z = 6.2$.

The $\varepsilon - h$ phase diagram of the $S = 1/2$ 1D XXZ model in longitudinal magnetic fields at zero temperature was made from the theoretical study as shown in Fig. 3-1-6 [16,60], where ε is the above anisotropy parameter and h is the external magnetic field H_z normalized by the AF exchange constant J ($h = H_z/J$). From this phase diagram, we found that the ground state at zero field is a magnetically ordered Néel state. On applying the magnetic fields along the z-axis, a magnetic order to disorder transition takes place, passing through a TL spin liquid state to the field-induced ferromagnetic state. The field-induced TL spin liquid state is considered to be a quantum critical

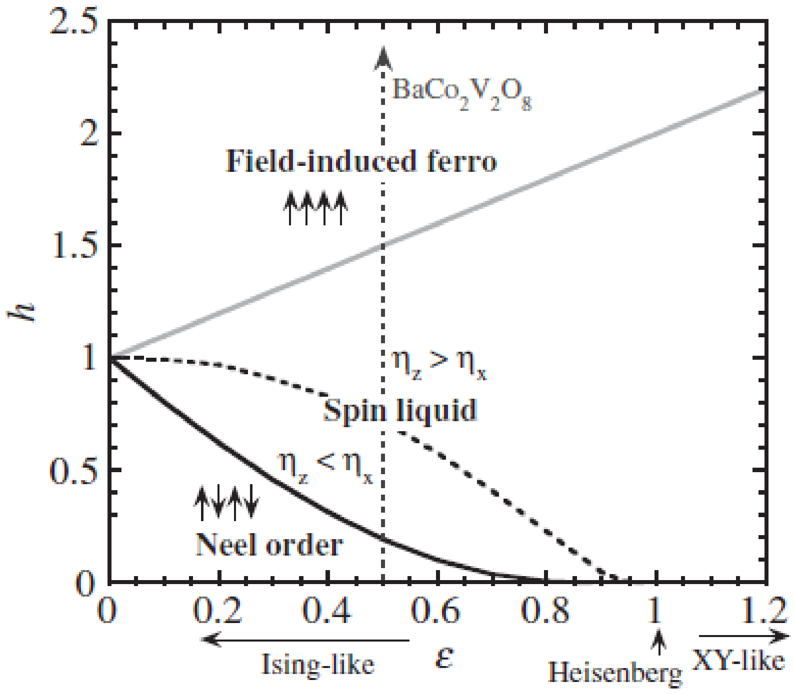

Figure 3-1-6: The magnetic field versus the anisotropic parameter ε phase diagram calculated in longitudinal magnetic fields. Quoted from [60].

state in which the spin correlation shows a power-law decay. The TL parameters η_z and η_x, which satisfy the relation $\eta_z\eta_x = 1$, are critical exponents that are characteristic of a TL spin liquid state and are related to the incommensurate correlation of the z component, expressed as $\langle S_0^z S_r^z \rangle - m^2 \simeq \cos(2k_F r)\, r^{-\eta_z}$ (m is the magnetization, $k_F = \pi(1/2 - m)$) and the staggered correlation of the x component, expressed as $\langle S_0^x S_r^x \rangle \simeq (-1)^r\, r^{-\eta_x}$, respectively. r is the distance between the spins S_0 and S_r. A schematic view of these components is shown in Fig. 3-1-7 [61]. In a TL spin liquid state of the $S = 1/2$ 1D Ising-like XXZ model, in a magnetic field applied along the z-axis direction, the incommensurate correlation is dominant in the low magnetic field region where $\eta_z < \eta_x$, while the staggered correlation is dominant in the high magnetic field region where $\eta_z > \eta_x$. Since BaCo$_2$V$_2$O$_8$ has $\varepsilon = 0.46$, the aforementioned correlation change must be realized when a magnetic field is applied along the c-axis as shown in Fig. 3-1-6.

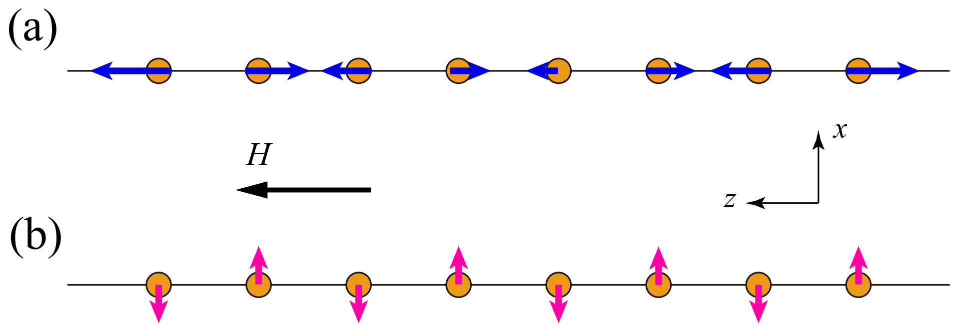

Figure 3-1-7: A schematic view of the spin correlations in the TL spin liquid state of the $S = 1/2$ 1D Ising-like antiferromagnet above H_{c}. (a) The incommensurate correlation of the z component. (b) The staggered correlation of the x component.

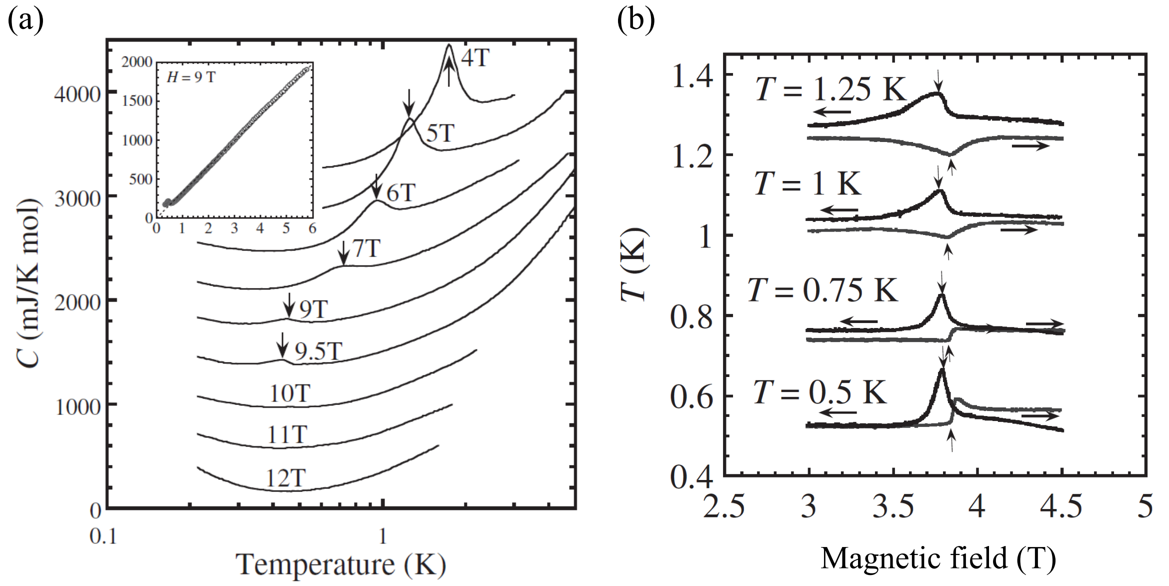

Figure 3-1-8: (a) Temperature dependence of the specific heat for $H \parallel c$ at designated magnetic fields. Each specific heat shifts up by 400 mJ/Kmol with decreasing field from 12 T. Inset shows an extended figure of the specific heat observed at 9 T. (b) The results of the magnetocaloric effect measurements by ascending and descending the magnetic field along the c-axis. Quoted from [60].

Figures 3-1-8(a) and 3-1-8(b) indicate the temperature dependence of the specific heat down to 0.2 K at designated magnetic fields, and the magnetocaloric effect down to 0.5 K when changing magnetic fields applied along the c-axis, respectively [60]. The magnetic phase diagram as shown in Fig. 3-1-9 was obtained from these experimental results. It was known that the field-induced phase transition occurs at about 4T, but as can be seen from the figure, a new phase was found to exist in the region below 1.8 K and above 4 T approximately. Neutron scattering experiments were performed to investigate the magnetic properties of this new phase as shown in Fig. 3-1-10 [61]. Up to 3.75 T, a single peak was observed at the position (4, 0, 3), which indicates a commensurate, whereas above 4 T, two peaks were observed at incommensurate

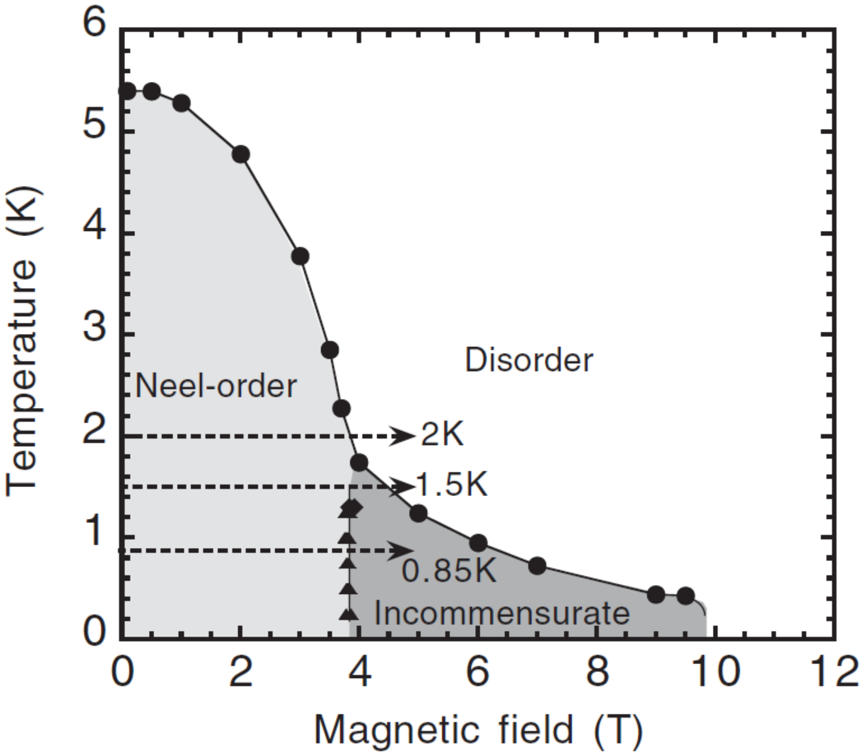

Figure 3-1-9: Magnetic phase diagram of $BaCo_2V_2O_8$ in the longitudinal magnetic fields. Neutron scattering experiments have been performed in magnetic fields at indicated temperatures shown by broken arrows. Quoted from [60].

positions that separate from the $l = 3$ position with increasing the magnetic field (Fig. 3-1-10(a)). Fig. 3-1-10(b) represents the plot of these peak positions with respect to the magnetic field, and the inset of Fig. 3-1-10(b) shows the plot of the magnetic field dependence of $2k_{\mathrm{F}}/\pi = (1 - m/m_s)$ (m_s is the saturated magnetization) using the distance from $l = 3$. This neutron scattering experiment shows that the new phase had an incommensurate correlation. This new phase must be the longitudinal incommensurate correlation predicted by theoretical studies on the $S = 1/2$ 1D XXZ model.

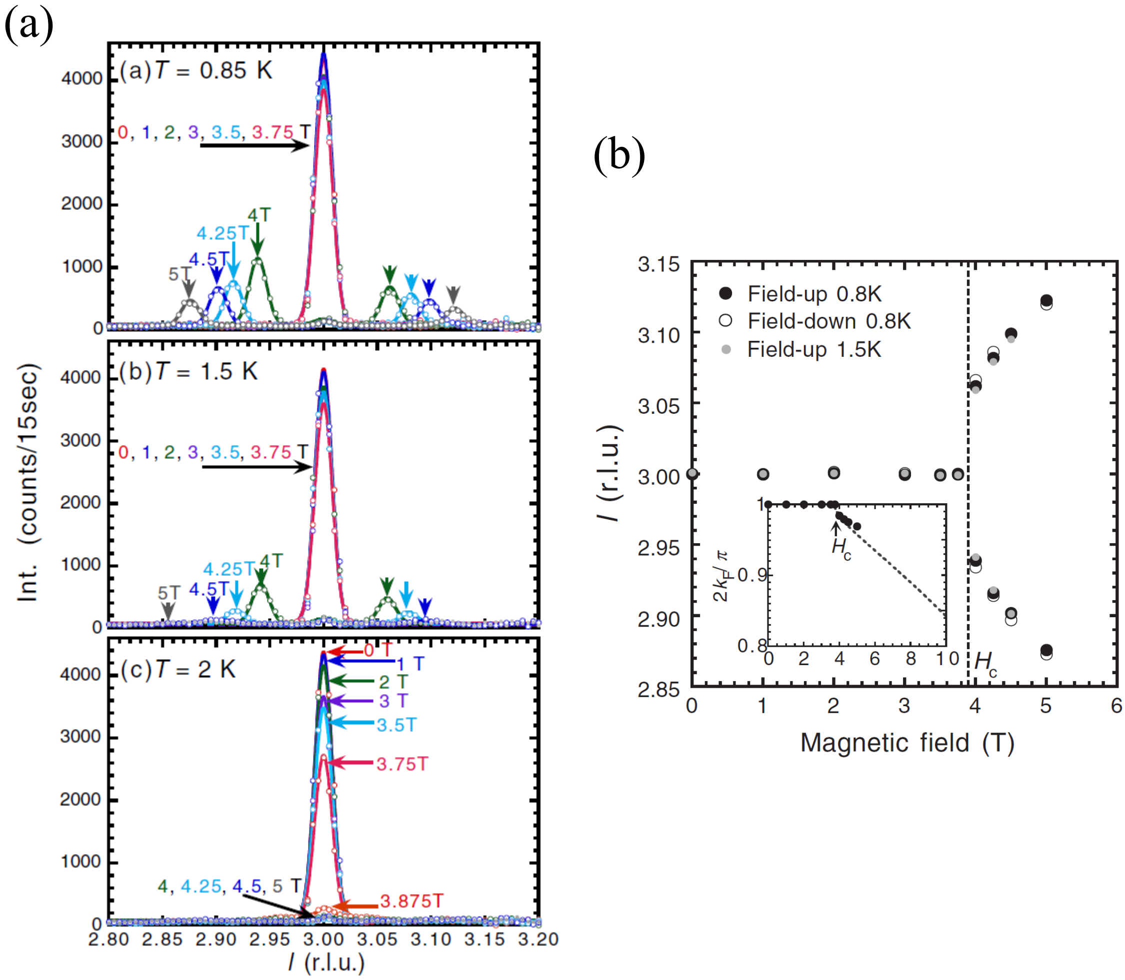

Figure 3-1-10: (a) Magnetic field dependence of neutron diffraction profiles of $(4, 0, l)$ scan measured at various temperatures. (b) Magnetic field dependence of the peak position of the observed neutron scan profile. Inset shows the field dependence of a normalized incommensurate modulation $2k_{\mathrm{F}}/\pi$. The broken line is the theoretical magnetization $1 - m/m_s$ curve obtained by the calculation based on the Bethe ansatz exact theory. Quoted from [61].

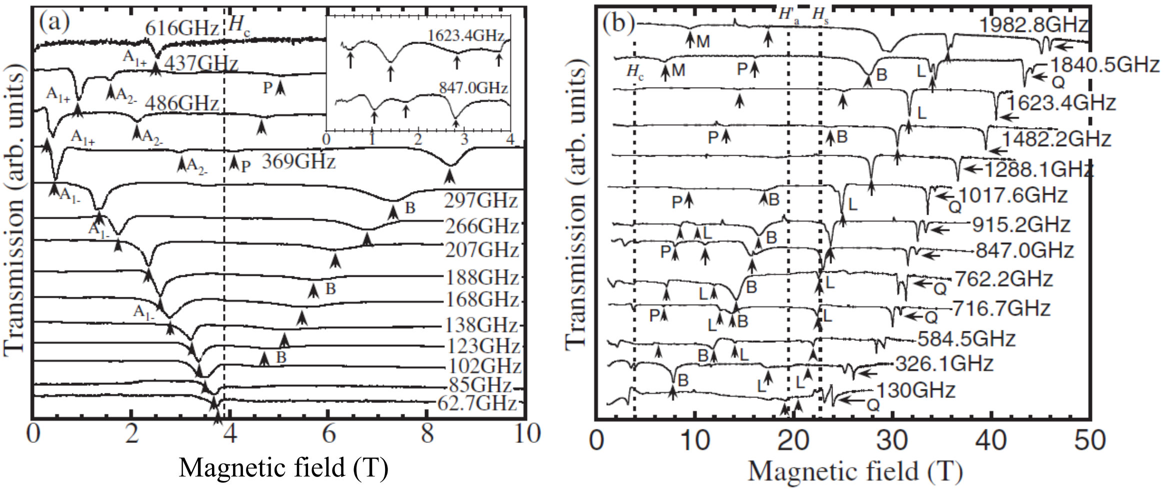

Figure 3-1-11: Frequency dependence of the ESR spectra observed in (a) static and (b) pulsed magnetic fields for $H \parallel c$. Quoted from [59].

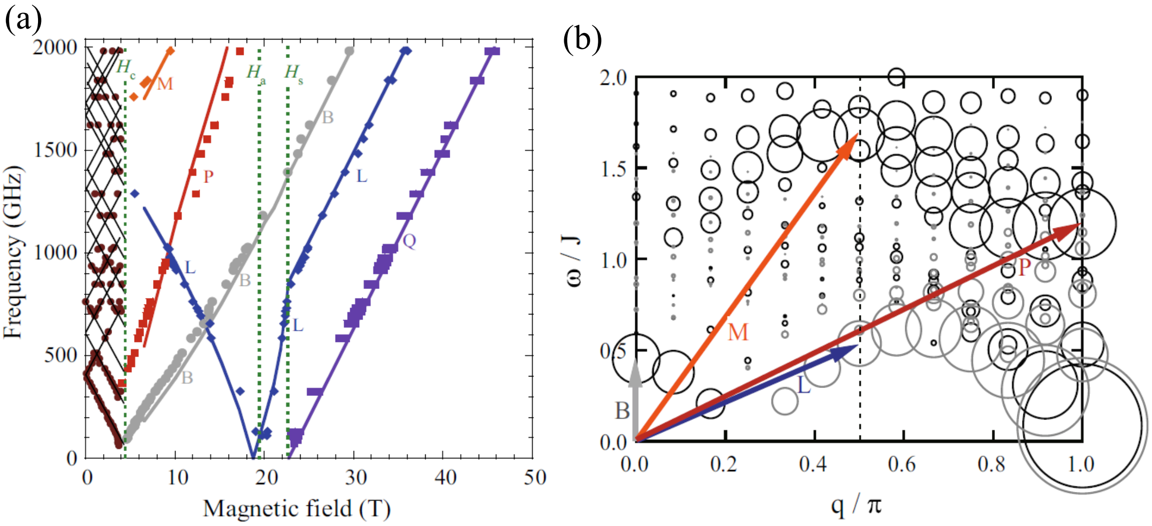

Figure 3-1-12: (a) Frequency versus resonance magnetic field plots of ESR along the c-axis. The thin solid lines below H_c are guide for the eyes. Above H_c, gray (B), orange (M), blue (L), and red (P) solid curves indicate theoretical excitation energies at the momentum $q = 0$ for B, $\pi/2$ for M and L, and π for P, as indicated by the arrows in (b). (b) DSSFs $S(q, \omega)$ calculated by the exact diagonalization for the total magnetization with 1/4 of the saturation value. Gray and black circles indicate $S^{+-}(q, \omega)$ and $S^{-+}(q, \omega)$, respectively. The size of the circle corresponds to the magnitude of the DSSF. Quoted from [59, 74]

Figures 3-1-11(a) and 3-1-11(b) depict the ESR spectra observed at various frequencies in static and pulsed magnetic fields applied parallel to the c-axis, respectively [59]. In Fig. 3-1-12(a), the plot of resonance magnetic fields indicated by the arrows in Figs. 3-1-11(a) and 3-1-11(b) against the frequencies is displayed. At zero magnetic field, there are discrete energy levels such as 400 GHz, 600 GHz, 750 GHz, etc. As shown in Fig. 3-1-13, these energy levels are generated because the excitation spinon band, which is a continuum in a pure one-dimensional antiferromagnet, is discretized by the interchain interaction and the discrete energy levels are called the Zeeman ladder [19, 73]. One ESR branch from the lowest mode of 400 GHz at zero field decreases as the magnetic field increases, and shows a softening at $H_c = 4$ T where a field-induced order-disorder transition occurs as represented in Fig. 3-1-14. The ground state and the excited ones of the $S = 1/2$ 1D Ising-like antiferromagnet below H_c represent a Néel order and spinon bands, in which spinon (domain walls) can propagate freely in the chain, as shown in Fig. 3-1-15. Above H_c, a pair of spinon (domain walls) propagate freely in the chain to destroy the magnetic order [73]. In addition, the resonance mode labeled L seems to show softening at H_a where the magnetization shows a value of 1/2 of the saturation magnetization, and the Q mode is observed above the saturation magnetic field H_s in Fig. 3-1-12(a). Other branches labeled B, P and M are also observed in Fig. 3-1-12(a). The modes observed below H_s are well consistent with the results of the dynamical spin structure factors (DSSFs) calculated by the exact diagonalization for the total magnetization with 1/4 of the saturation value as shown in Fig. 3-1-12(b).

Consequently, the experimental results of magnetization, ESR, and neutron scattering agree well with the theoretical results of numerical calculations, and thus $BaCo_2V_2O_8$ has been actively studied as a model material for the $S = 1/2$ 1D XXZ model.

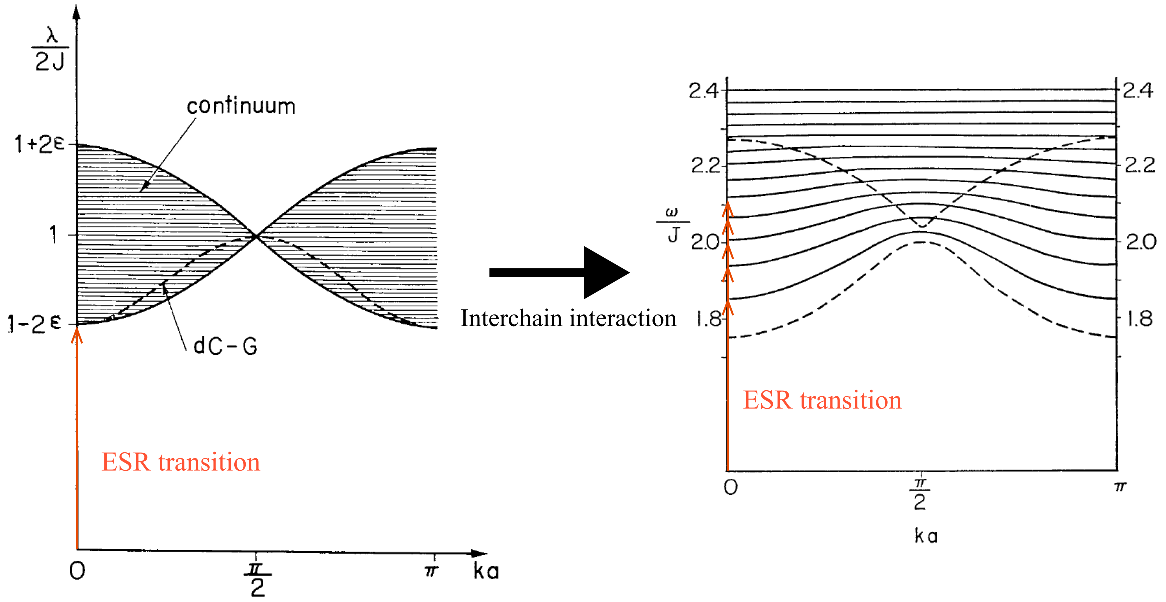

Figure 3-1-13: Magnetic excitation spectrum of the $S = 1/2$ 1D Ising-like antiferromagnet. In the case of a pure 1D chain, the magnetic excitation spectrum is a continuum (spinon band), but the continuum becomes discretized by the interchain interactions [19, 73]. The orange arrow indicates the corresponding ESR transition.

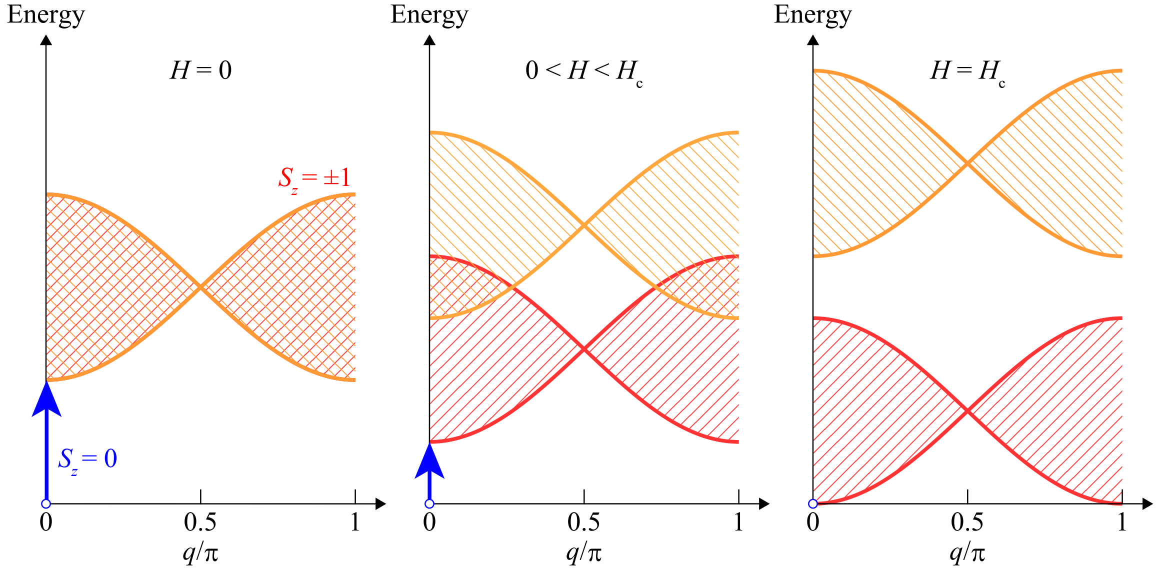

Figure 3-1-14: Spinon band excitations in magnetic fields. The blue arrow indicates the ESR excitation between the ground state and the lowest excited state. H_c is the critical field where the softening of the excited state occurs.

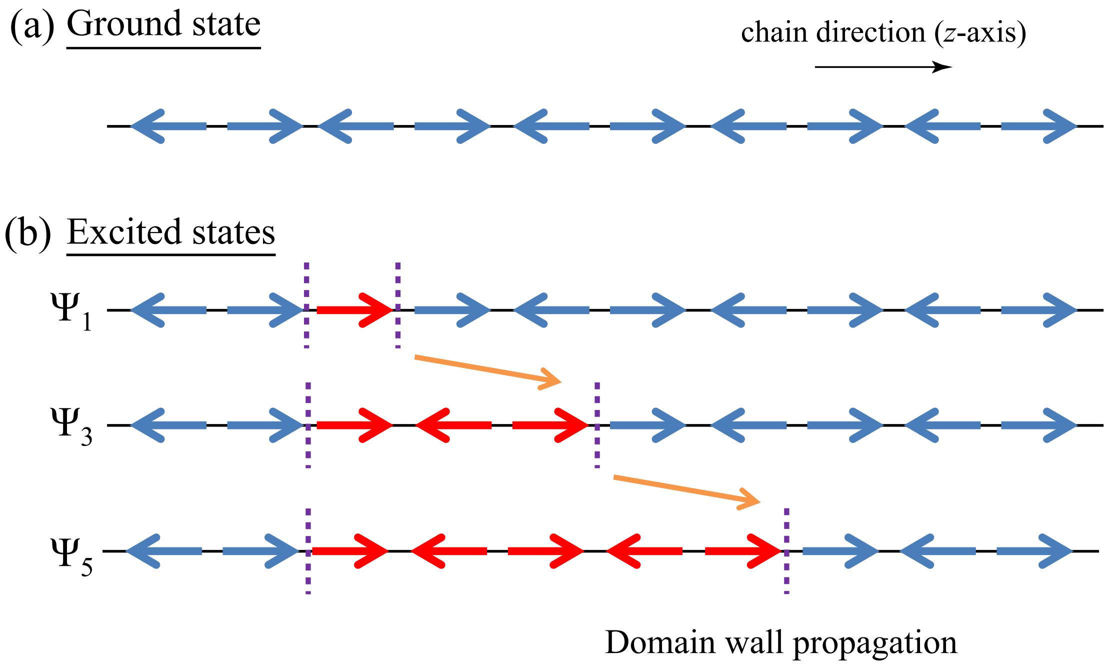

Figure 3-1-15: (a) Néel ordered ground state along the chain (z-axis in the Ising-like model). (b) Spinon (domain wall) excited states. Domain walls indicated by dotted lines propagate freely inside the chain to destroy the Néel order.

3-1-3 High-Field Magnetism in Transverse Magnetic Fields

In a simple one-dimensional XXZ antiferromagnet described by Eq. (1-1-1), the transverse magnetic field perpendicular to the chain causes the same effect in all directions perpendicular to the chain owing to its symmetry. It was not thought to be important to pay particularly attention to the direction of the transverse magnetic field at the early stage of the studies on $BaCo_2V_2O_8$ because of the tetragonal system. However, it was later found that the behavior was different depending on the magnetic field direction, [100] and [110]. Figures 3-1-16(a) and 3-1-16(b) display the temperature derivative of magnetic susceptibility at various fields and the field derivative of the magnetization curves at various temperature in transverse fields along the [100] direction [65]. The phase diagram made from the peaks seen in these figures is shown in Fig. 3-1-17. Previous specific heat results for $H \perp c$ [28] in Fig. 3-1-3(b) corresponds to the case for the magnetic field applying along the [110] direction. Looking at the phase diagram for $H \parallel [100]$ in Fig. 3-1-17, the phase boundary drops off sharply at around 10 T in response to the rapid suppression of the Néel order by the magnetic field, whereas for $H \parallel [110]$, the Néel order seems to be maintained up to higher magnetic field than 9 T. Such differences are also observed in the thermal expansion measurements (Fig. 3-1-18), the magnetostriction measurements, and the thermal conductivity measurements (Fig. 3-1-19) [64, 66].

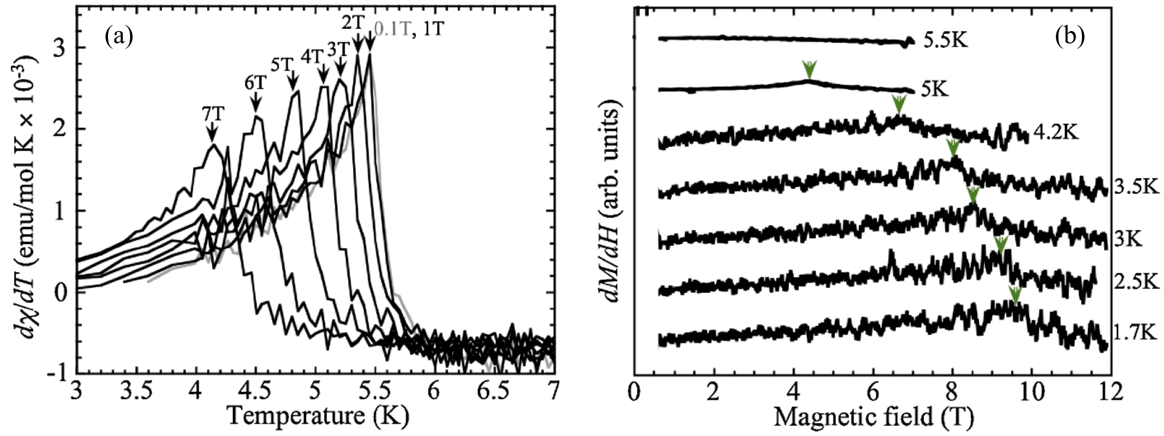

Figure 3-1-16: (a) Temperature derivative of magnetic susceptibility ($d\chi/dT$) and (b) field derivative of magnetization (dM/dH) curves, observed for $H \parallel [100]$. Quoted from [65].

The results of the magnetization measurements in transverse fields for [100] and [110] directions at 1.3 K are depicted in Fig. 3-1-20. In this figure, the contribution of the Van-Vleck paramagnetism is subtracted. For $H \parallel [110]$, the magnetization reaches the saturation value at 40.9 T, while for $H \parallel [100]$, the magnetization curve gently increases with rounding even above 50 T, and the magnetization does not saturate. In $BaCo_2V_2O_8$, the principle axes of CoO_6 octahedron deviates from the crystal axes as shown in Figs. 3-1-21(a)–(c). A rounding of the magnetization curve in a high magnetic field was also reported in quasi-1D $S = 1/2$ Heisenberg antiferromagnets such as Cu pyrimidine nitrate and Cu benzoate [75, 76], and the magnetization process was well reproduced by introducing effective staggered magnetic fields owing to the

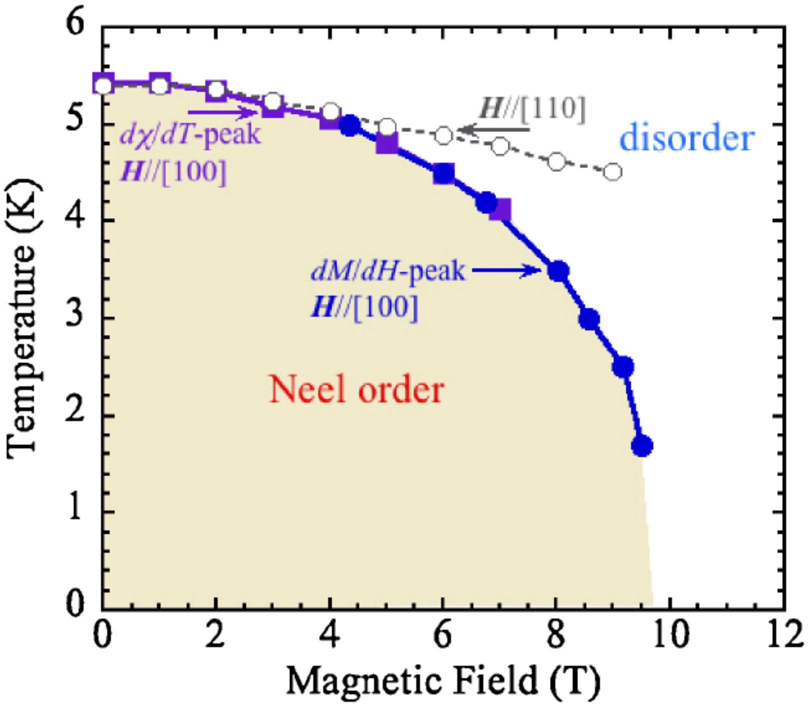

Figure 3-1-17: Phase diagram in different transverse fields along [100] and [110] directions [65]. Closed circles and squares are transition points obtained from the magnetization and magnetic susceptibility measurements for $H \parallel [100]$. Open circles are those from the previous specific heat measurements for $H \parallel [110]$ [28].

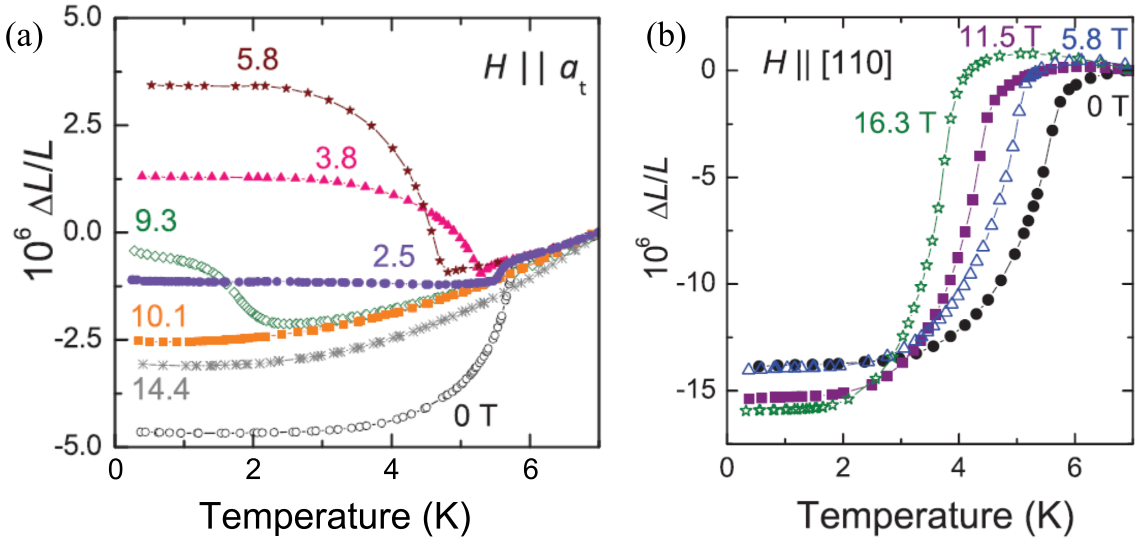

Figure 3-1-18: Temperature dependences of the thermal expansion for (a) $H \parallel [100]$ (a_t represents the a-axis in tetragonal system) and (b) for $H \parallel [110]$ at designated magnetic fields. The temperatures of the inflection point varies depending on the direction of the magnetic fields. Quoted from [66].

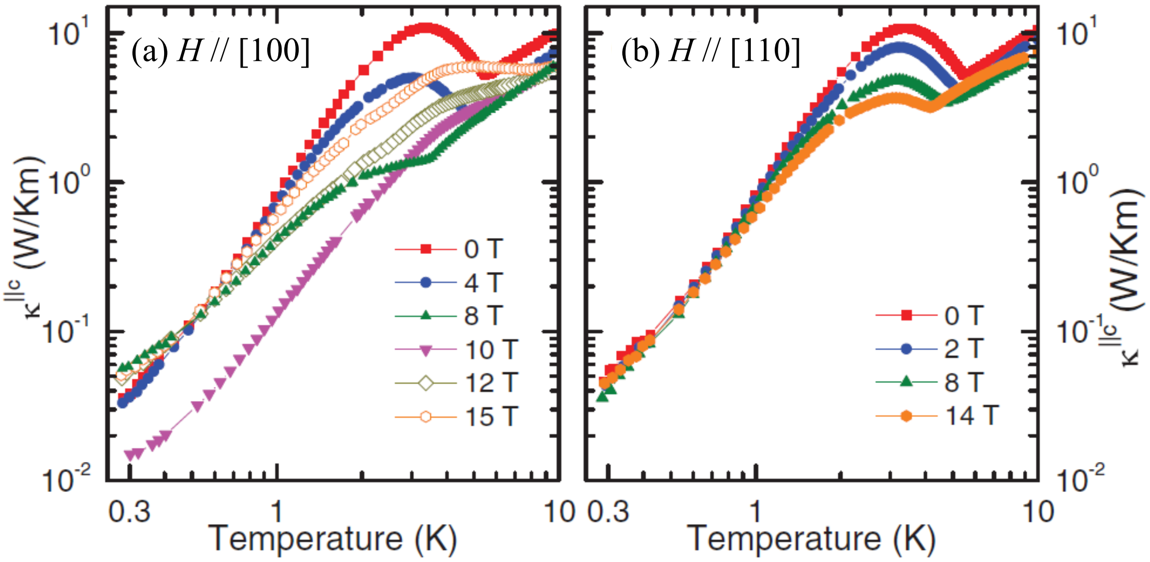

Figure 3-1-19: Temperature dependences of the thermal conductivity along the c-axis for (a) $H \parallel [100]$ and (b) for $H \parallel [110]$ at designated magnetic fields. The temperatures of the inflection point varies depending on the direction of the magnetic fields. Quoted from [66].

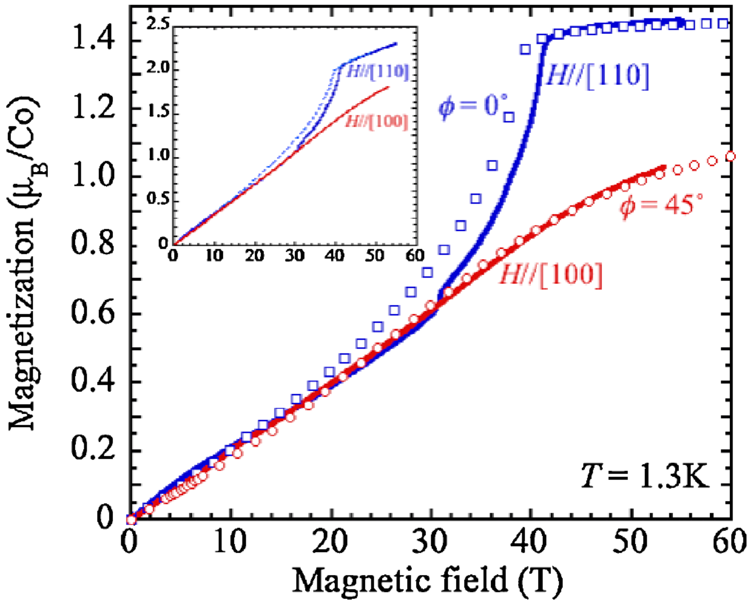

Figure 3-1-20: The solid lines show the experimental results, for which Van-Vleck contributions are subtracted, of the high-field magnetization measurements in transverse fields at 1.3 K. Open squares and circles represent the theoretical curves calculated using a Density Matrix Renormalization Group method with the effective fields for $\phi_1 = 45°$ and $\phi_1 = 0°$, respectively. In the inset, the experimental and the calculated results before subtracting the Van-Vleck contribution are shown. Quoted from [65].

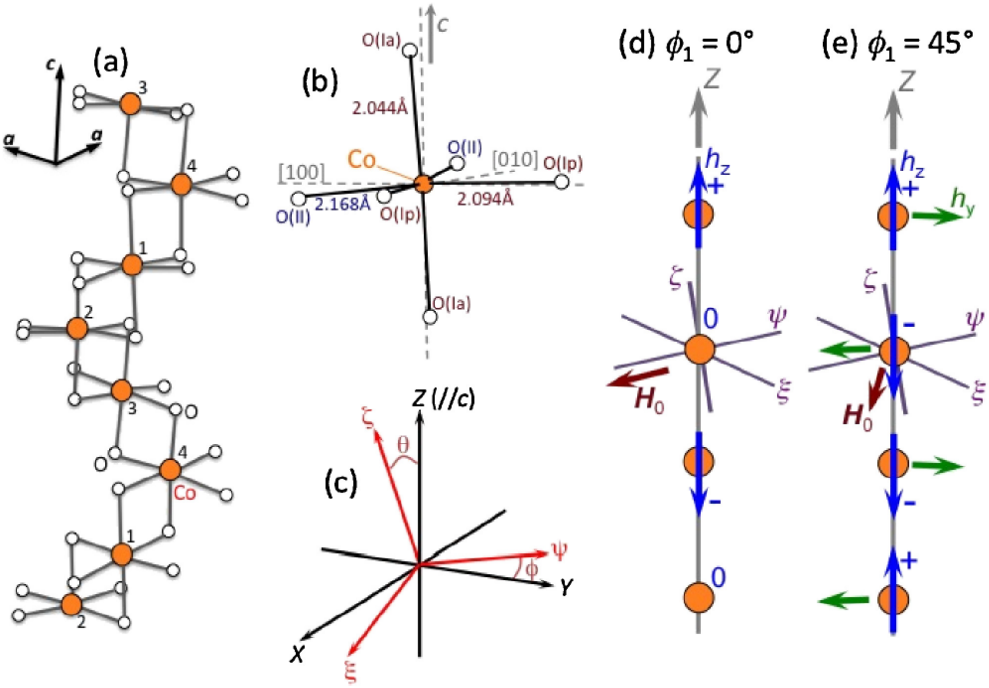

Figure 3-1-21: Schematic view of (a) Co$-$O chain and (b) CoO_6 octahedron in $BaCo_2V_2O_8$. (c) Relation between the XYZ and $\xi\psi\zeta$-coordinate systems. The effective fields h_Y and h_Z appear for (d) $\phi_1 = 0°$ and (e) $\phi_1 = 45°$. The directions of h_Y and h_Z are Y- and Z-axis directions, respectively. Quoted from [65].

alternation of local crystal structure around Cu^{2+} ion [76, 77]. It was also reported in the 1D Cu^{2+} compound $CuCl_2 \cdot 2\,((CD_3)_2SO)$ that the staggered magnetic fields suppress the AF order [78]. Thus, in $BaCo_2V_2O_8$, the model is suggested in which effective staggered magnetic fields arise from the local crystal structure as the four-step periodical arrangements of CoO_6 octahedra and affect the magnetization process in transverse fields for [100] and [110] directions. The effective spin Hamiltonian based on this model is written as,

$$\begin{aligned}\mathcal{H}_{\text{chain}} =& J\sum_j \left\{S_j^z S_{j+1}^z + \varepsilon\left(S_j^x S_{j+1}^x + S_j^y S_{j+1}^y\right)\right\} \\ & - \mu_{\text{B}}\sum_j \Bigg\{ g_{xx} H_0 S_j^x + h_y S_j^y \sin\left[2\phi_1 + \pi(j-1)\right] \\ & + h_z S_j^z \cos\left[\phi_1 + \frac{\pi(j-1)}{2}\right]\Bigg\}, \end{aligned} \tag{3-1-2}$$

where S_j^α, J, ε (< 1), μ_{B} are the same as in Eq. (3-1-1) and, g_{xx} is the g-factor along the x-axis, H_0 is the external magnetic field applied along the x direction, h_y and h_z are effective magnetic fields induced along the y and z directions, respectively. The effective magnetic fields, which appear in external magnetic fields for $\phi_1 = 45°$ and $\phi_1 = 0°$, are depicted in Figs. 3-1-21(d) and 3-1-21(e). (In these figures, the capital letters X, Y, and Z are used instead of small letters x, y, and z.) The angle ϕ_1 is the angle formed by ψ axis of the magnetic principle axis and the y axis in the xy-plane. The important point is that h_y takes the maximum absolute value for $\phi_1 = 45°$ while alternately changing direction, whereas it disappears for $\phi_1 = 0°$. The ratio of the external magnetic field to the internal effective magnetic field is defined as the parameters $C_y = h_y/g_{xx}H_0$ and $C_z = h_z/g_{xx}H_0$. They are calculated with the parameters $J/k_{\mathrm{B}} = 65$ K, $\varepsilon = 0.46$, $C_y = 0.4$, and $C_z = 0.1\sqrt{2}$. The g-values are $g_{xx} = 2.95$ for $\phi_1 = 0°$ and $g_{xx} = 2.95$ for $\phi_1 = 45°$. As a result, the experimental magnetization curves are reproduced well by the theoretical calculation.

3-1-4 Purpose of This Study

From these magnetic and thermal measurements in transverse magnetic fields along the [100] and [110] directions, it has been found that physical properties (magnetization, specific heat, magnetostriction, thermal expansion and thermal conductivity are different largely for these directions. To clarify the difference in the properties between these field directions, we investigate from the view point of spin excitations especially by high-field ESR. In the present paper, we report on magnetic properties of $\mathrm{BaCo_2V_2O_8}$ in transverse magnetic fields. The density-matrix renormalization group (DMRG) method is used to study the magnetic field dependences of the magnetization and the ESR spectra numerically. The elementary excitation associated with the lowest ESR branch is discussed in terms of the spinon using the Jordan-Wigner transformation as well.

3-2 Experiment and Calculation

3-2-1 Crystal Growth

Single crystal samples of $BaCo_2V_2O_8$ used in this study were grown by the floating-zone (FZ) method, as reported in detail in Ref. 79 but using Co_3O_4 instead of $CoC_2O_4 \cdot 2\,H_2O$. First, a polycrystalline sample of $BaCo_2V_2O_8$ was synthesized by the solid-state reaction. The starting materials $BaCO_3$ (99.99+%), Co_3O_4 (99.9%), and V_2O_5 (99.99%) were weighted in the stoichiometric proportions and well mixed. Next, the mixture in a Pt crucible was heated using the muffle furnace at 950 °C for 12 hours under air. Then, the mixture was pulverized well and compacted into pellets, and heated again at 950 °C for 60 hours on a Pt sheet under air. In both steps, it took 4 hours to raise the temperature to 950 °C, and after heating, it was naturally cooled to room temperature. The above sequence is shown in Fig. 3-2-1. The chemical reaction formula is described below,

$$3\,BaCO_3 + 2\,Co_3O_4 + 3\,V_2O_5 \longrightarrow 3\,BaCo_2V_2O_8 + 3\,CO_2 + O_2. \tag{3-2-1}$$

Co_3O_4 is composed of Co^{2+} and Co^{3+} ions, but at the temperature 900 °C or higher, it decomposes into CoO composed of Co^{2+} ions, and thus the temperature was set to 950 °C.

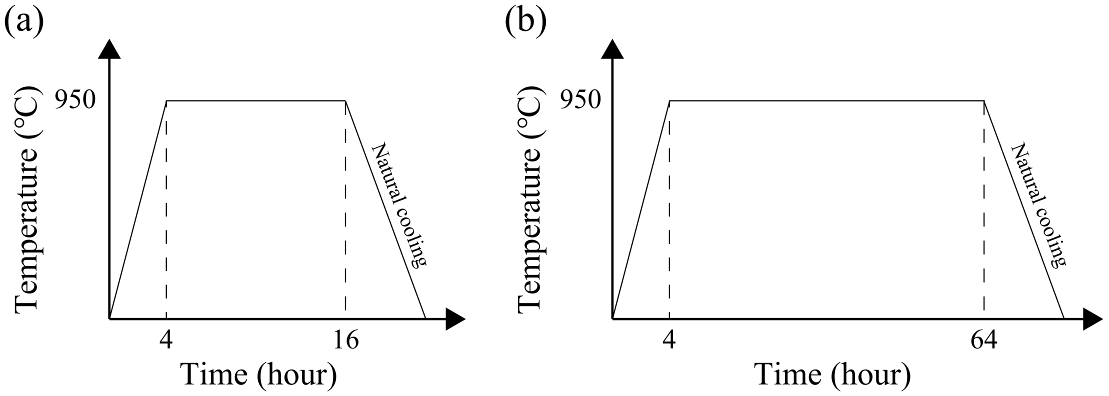

Figure 3-2-1: (a) First step of the solid state reaction sequence of $BaCo_2V_2O_8$. The muffle furnace was used for heating. (b) Second step of the solid state reaction. The mixture was compacted into pellets.

The synthesized powder sample (before FZ synthesis) was checked by X-ray diffraction (XRD) using Rigaku RINT-2000. Figure 3-2-2 shows an X-ray diffraction pattern compared with its simulation pattern taken by RIETAN-FP [80] through VESTA [58] as shown in Fig. 3-2-2. The characteristic peak was observed to compare with the simulation pattern, and no peaks from impurities were observed. Then, the powder was pressed into a rod under the hydrostatic pressure and sintered at 950 °C for 24 hours for use in the FZ furnace. Finally, single crystal growth was performed by a floating zone method as depicted in Fig. 3-2-3. The feed and seed rods were rotated at 30 rpm in opposite directions to stir the melt and make the temperature as uniform as possible. As grown single crystal rod about 4 mm in diameter and 50 mm in length was obtained by pulling the rod at the speed of 0.5 mm/h in a mixture of flowing oxygen (20%) and nitrogen (80%) at ambient pressure (see Fig. 3-2-4(a)).

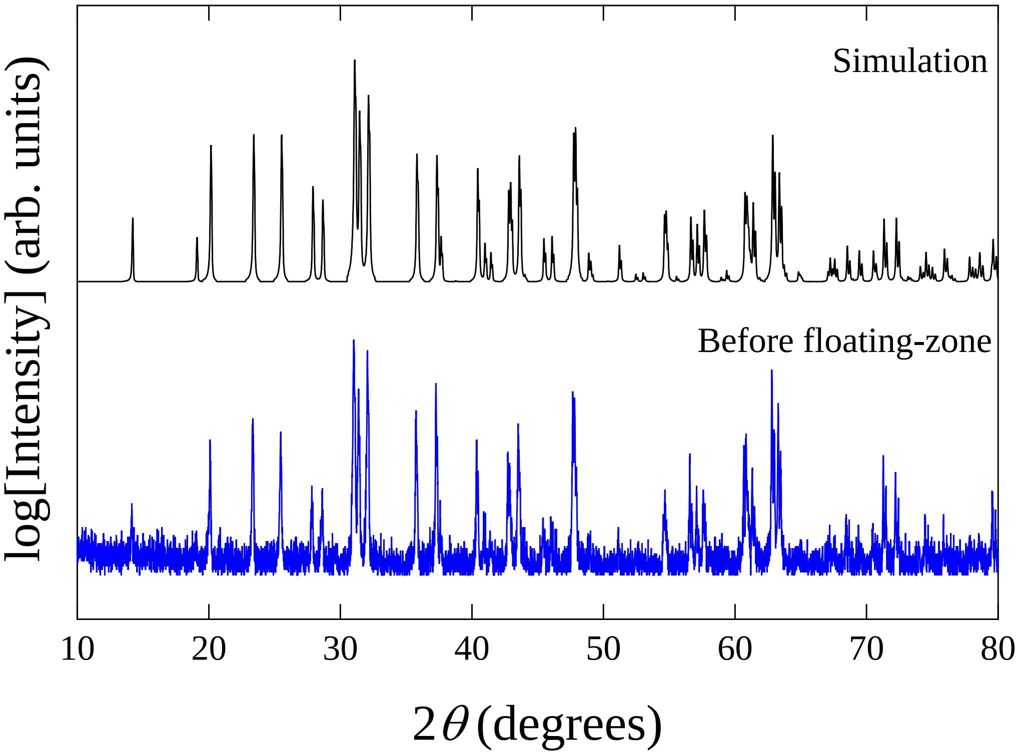

Figure 3-2-2: XRD pattern of a powder sample of $BaCo_2V_2O_8$ and the simulation result performed on RIETAN-FP [80].

We determined the crystal axes by the back-reflection Laue method compared to the simulation pattern using LauePt software [81] as shown in Fig. 3-2-5, and cut out the single crystal rod into blocks and plates (see Fig. 3-2-4(b)) by a diamond wire saw. Figure 3-2-6 shows the XRD patterns by Bruker D2 PHASER on the plate-shaped single crystal sample to confirm the surface directions. The quality of the single crystal samples were found to be high enough, because the Laue pattern was clear with no spot splitting, and the XRD pattern was in agreement with the simulation results. The block-shaped samples were used for magnetic susceptibility and magnetostriction measurements, and the plate-shaped samples were used for ESR and specific heat measurements.

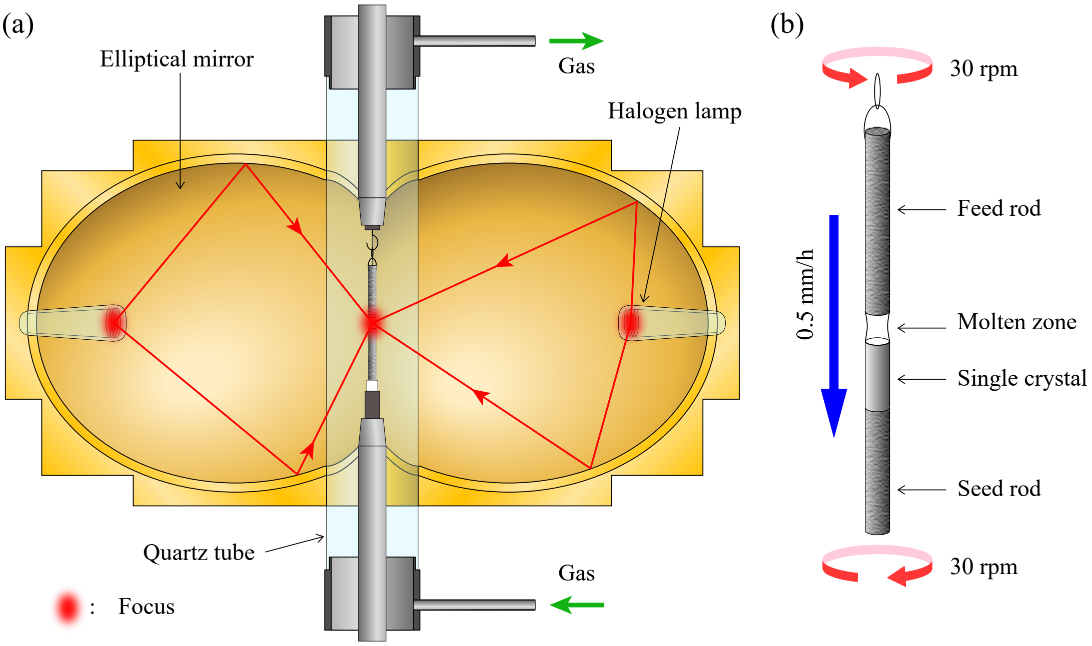

Figure 3-2-3: (a) Illustration of infrared image furnace for crystal growth. (b) Schematic view of crystal growth.

Figure 3-2-4: (a) Synthesized single crystal rod of $BaCo_2V_2O_8$ obtained by the FZ method. (b) Plate-shaped single crystal sample of $BaCo_2V_2O_8$ viewed from the c-axis.

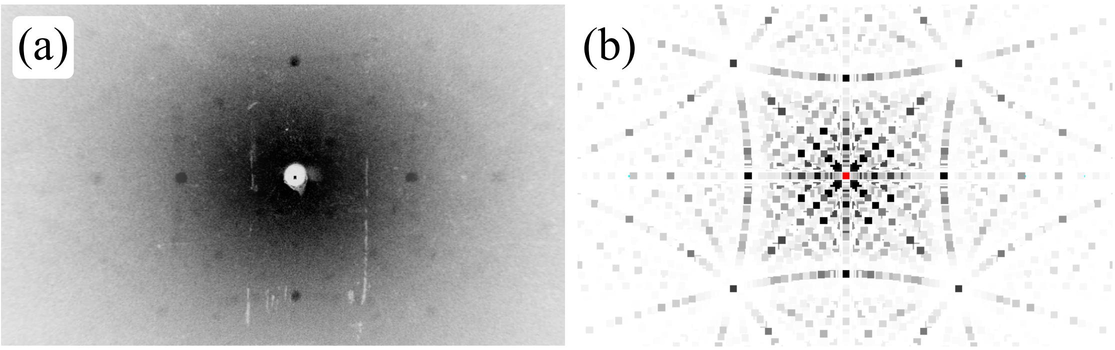

Figure 3-2-5: (a) Back-reflection Laue pattern taken from the (001) face of $BaCo_2V_2O_8$. (b) The simulated Laue pattern using LauePt software [81].

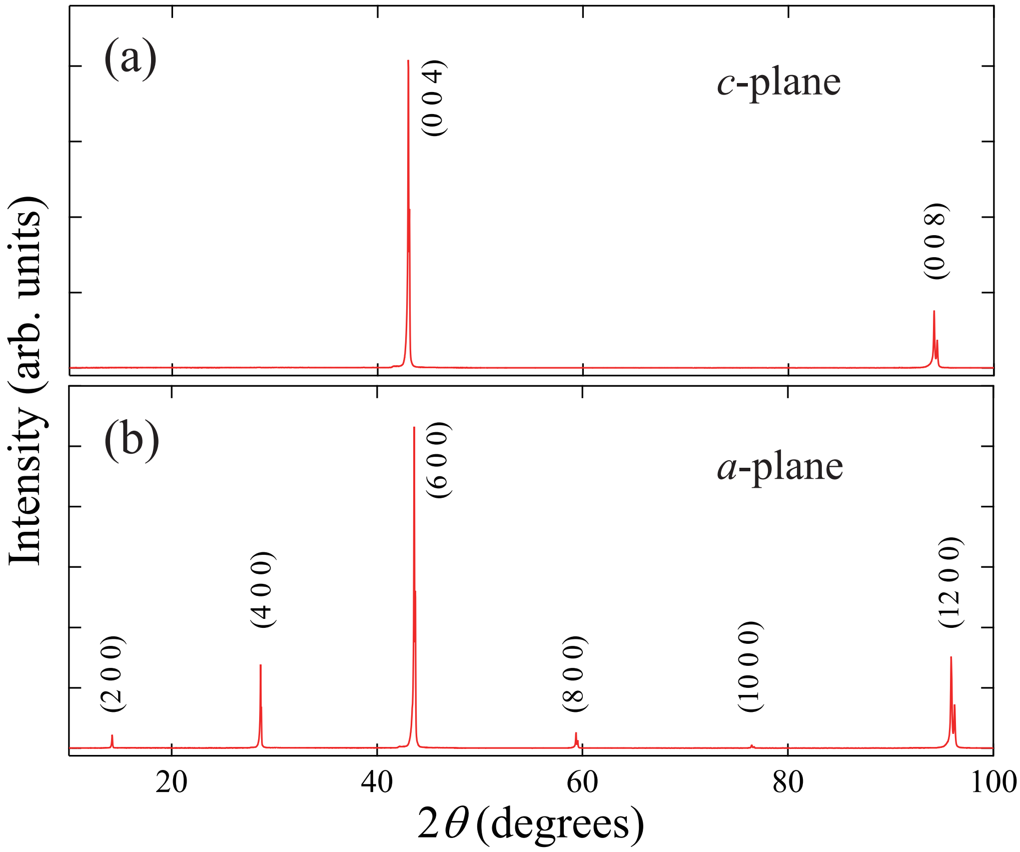

Figure 3-2-6: The XRD pattern of the plate-shaped single crystal samples of $BaCo_2V_2O_8$ from (a) *c*-plane and (b) *a*-plane. RIETAN-FP [80] was used for peak assignment.

3-2-2 Experimental Results

The temperature dependences of magnetic susceptibilities $\chi = M/H$ (where M is the magnetization and H is the external magnetic field) of $BaCo_2V_2O_8$ single crystals in magnetic fields along the [001], [100], and [110] directions of tetragonal symmetry at $\mu_0 H = 0.1$ T are depicted in Fig. 3-2-7. The broad peak of the susceptibility for $H \parallel [001]$(c-axis) is observed near 35 K, typical of a low-dimensional antiferromagnet. The susceptibility along the c-axis represents an abrupt decrease below 5 K, and those along the [100] and [110] directions overlap in most temperature regions with a peak at about 5 K, corresponding to the Néel temperature, but below T_N, the susceptibility of [100] direction has a slightly larger than that of [110] direction. These observations are the same as those reported in Refs. 27 and 28. The large magnetic anisotropy in magnetic susceptibility exists between $H \parallel [001]$ and the other directions. Since no rapid increase of the susceptibility at low temperature was observed in any magnetic field direction, it was assessed that there were few paramagnetic impurity.

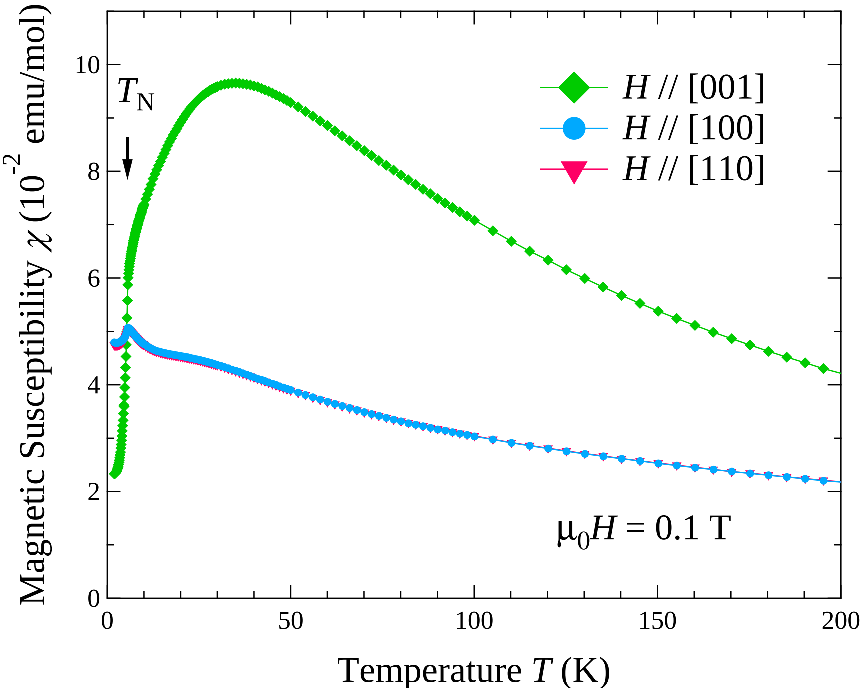

Figure 3-2-7: Temperature dependences of the magnetic susceptibilities of single crystals of $BaCo_2V_2O_8$. Squares, circles, and triangles represent [001], [100], and [110] directions of the external magnetic field, respectively.

Figures. 3-2-8(a) and 3-2-9(a) show the frequency dependence of the ESR absorption spectra in Voigt configuration at 1.4 K in pulsed magnetic fields and those at 1.5 K in static magnetic fields for $H \parallel [100]$ and $H \parallel [110]$, respectively. We observed several strong and weak signals with small splittings that are probably caused by magnetic domains due to the structural phase transition from tetragonal to orthorhombic symmetry at T_N [66]. The sharp peaks indicated by the plus signs are the signals of DPPH as a magnetic field calibration sample.

Figures 3-2-8(b) and 3-2-9(b) represent the frequency versus resonance-field plot

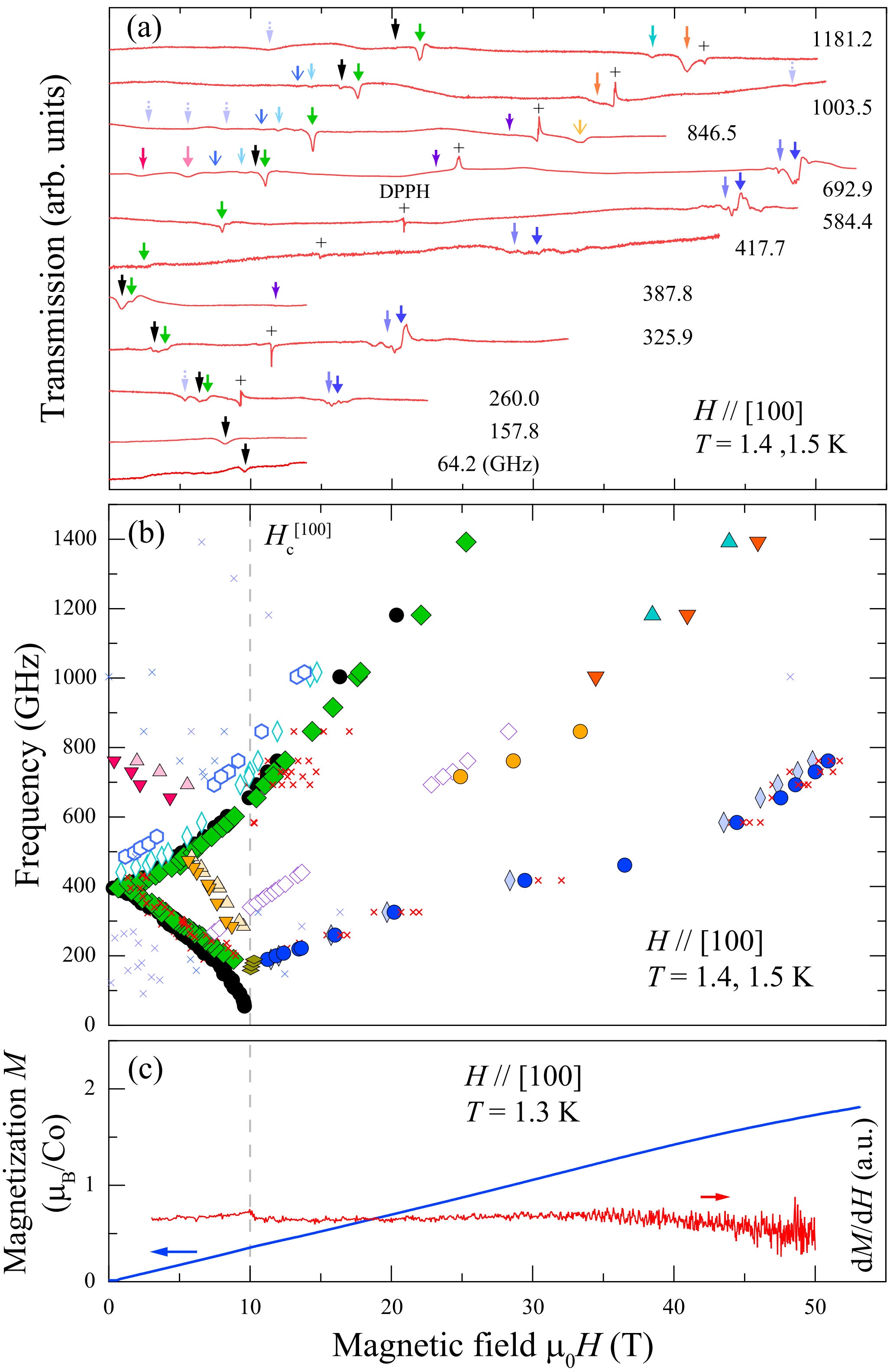

Figure 3-2-8: (a) ESR spectra at 1.4 K and 1.5 K for $H \parallel [100]$ in Voigt configuration. The sharp peaks indicated by the plus signs are the signals of DPPH. (b) Resonant frequency versus resonant field plot and (c) magnetization curve and the field derivative of magnetization ($\mathrm{d}M/\mathrm{d}H$) at 1.3 K, both for $H \parallel [100]$ [30]. $H_c^{[100]}$ is the magnetic field at an anomaly observed in $\mathrm{d}M/\mathrm{d}H$.

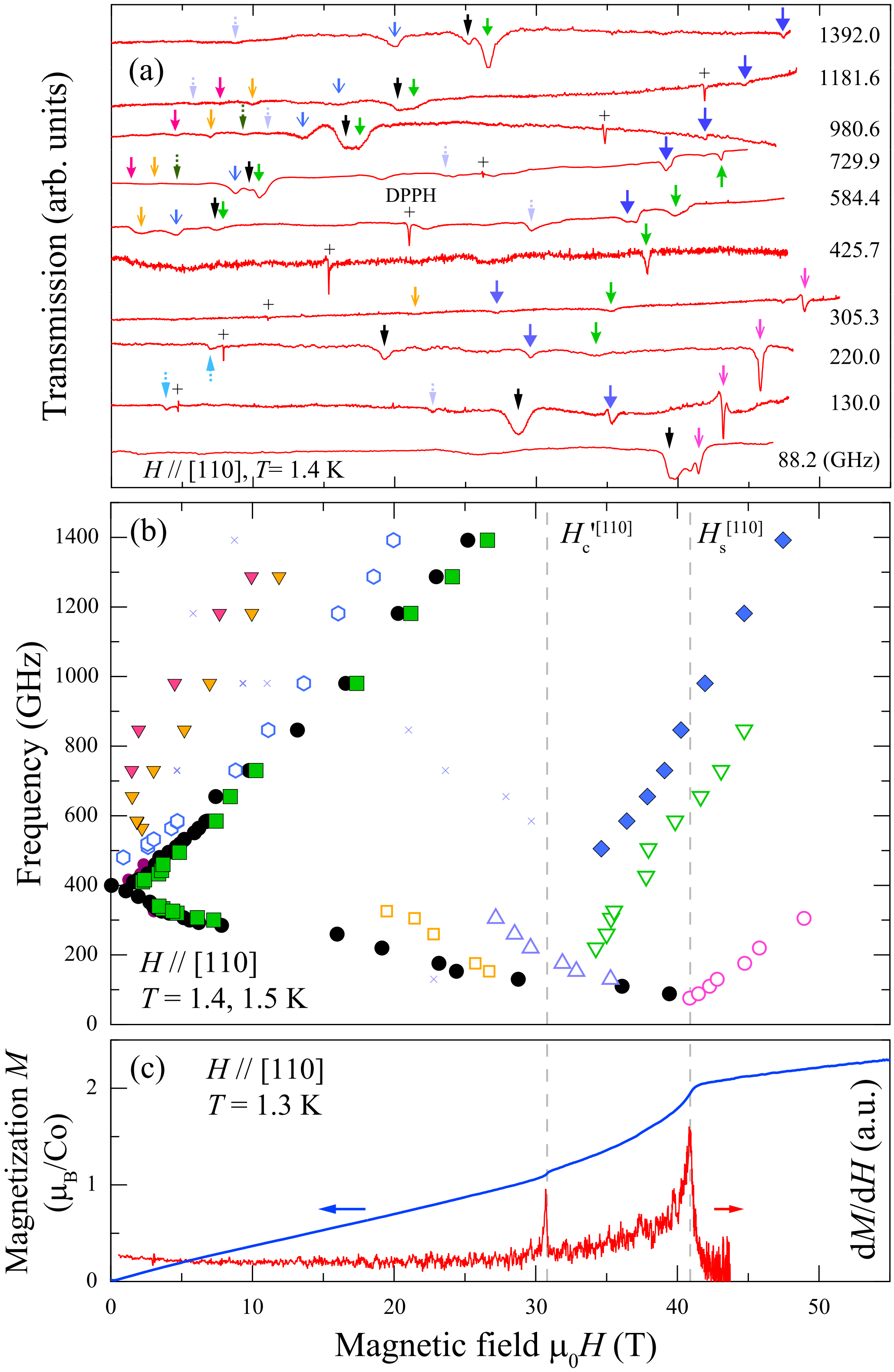

Figure 3-2-9: (a) ESR spectra at 1.4 K for $H \parallel [110]$ in Voigt configuration. The sharp peaks indicated by the plus signs are the signals of DPPH. (b) Resonant frequency versus resonant field plot and (c) magnetization curve and the field derivative of magnetization ($\mathrm{d}M/\mathrm{d}H$) at 1.3 K, both for $H \parallel [110]$ [30]. $H_c'^{[110]}$ and $H_s^{[110]}$ are the magnetic fields at anomalies observed in $\mathrm{d}M/\mathrm{d}H$.

for $H \parallel [100]$ and $H \parallel [110]$, respectively. The data points on probably the same ESR branch are indicated by the same colors and markers. Weak resonance signals are plotted by cross markers. The signals of DPPH are omitted and paramagnetic resonance lines are drawn instead. For comparison, the positions of the anomalies observed in the field derivative of magnetization ($\mathrm{d}M/\mathrm{d}H$) in Figs. 3-2-8(c) and 3-2-9(c), are shown as vertical dashed lines, where $H_\mathrm{c}^{[100]} = 10$ T, $H_\mathrm{c}'^{[110]} = 30.8$ T, and $H_\mathrm{s}^{[110]} = 40.9$ T. The lowest energy gap at zero magnetic field is observed at 400 GHz and two main ESR branches indicated by filled black circles appear from this gap. The upper ESR branches monotonically increase as the magnetic field increases for both [100] and [110] directions, whereas the lower ESR branches for $H \parallel [100]$ and $H \parallel [110]$ behave differently.

For $H \parallel [100]$, the lower mode decreases quickly with increasing magnetic field and exhibits softening near $H_\mathrm{c}^{[100]}$. Another lower ESR branch appearing from 400 GHz at zero magnetic field, indicated by filled green diamonds in Fig. 3-2-8(b), shows no softening of the mode but disappears near $H_\mathrm{c}^{[100]}$. An ESR branch with a finite gap turns up from about $H_\mathrm{c}^{[100]}$ and increases with changing its slope on further applying magnetic fields up to 53 T. In the field region below $H_\mathrm{c}^{[100]}$, numerous resonance modes with various zero field gaps are found to originate from a Zeeman ladder, and have been observed in previous studies [32, 59, 67]. Between the lowest and highest modes, we observed some additional modes and one of them marked by open rhombuses appears from 300 GHz at about 10 T. This linear mode is not a paramagnetic resonance due to a paramagnetic impurity because there is a finite gap at zero magnetic field when extrapolating linearly. For $H \parallel [110]$, as shown in Fig. 3-2-9(b), no softening of the excitation mode was observed and another mode marked by inverted triangles seems to show softening at around $H_\mathrm{c}'^{[110]}$ where an anomaly was observed in the magnetization curve and its $d\mathrm{M}/d\mathrm{H}$ (clear peak) as indicated in Fig. 3-2-9(c). This might be caused by the softening at a different q value like $\pi/2$ as observed in the ESR branches for $H \parallel [001]$ [59]. This matter will be discussed in the last paragraph on P.54.

The excitation mode that appears near 460 GHz (∼1.9 meV) in zero field indicated by open blue hexagons is observed in transverse magnetic fields ($H \parallel [110]$ and $H \parallel [100]$), and no such excitation mode appears in longitudinal magnetic fields ($H \parallel [001]$) [59]. This excitation mode is expected to be a longitudinal (fluctuation) mode and was observed by neutron scattering experiments [32, 68]. The longitudinal mode is associated with the domain-wall excitation caused by flipping an even number of spins in a domain and has a change in a total spin $\Delta S_z = 0$, which forbids the conventional ESR transition. This situation corresponds to the ESR for $H \parallel [001]$. On the other hand, a transverse mode is generated by flipping an odd number of spins, indicating that $\Delta S_z = \pm 1$, and the ESR transition is allowed. Here, we note that the longitudinal and transverse modes are separated when S_z is conserved, whereas they are mixed owing to the transverse magnetic fields. As a result, the ESR transition to the longitudinal mode is allowed in the transverse magnetic fields, leading to the excitation mode at 460 GHz.

The ESR spectra for $H \parallel [100]$ at designated temperatures below 4.2 K for the two frequencies as shown in Figs. 3-2-10(a) and 3-2-10(b). For simplicity, the ESR signals related to the phase transition at about $H_\mathrm{c}^{[100]}$ are indicated by black arrows, omitting the ESR signals unrelated to that. The resonance fields were determined

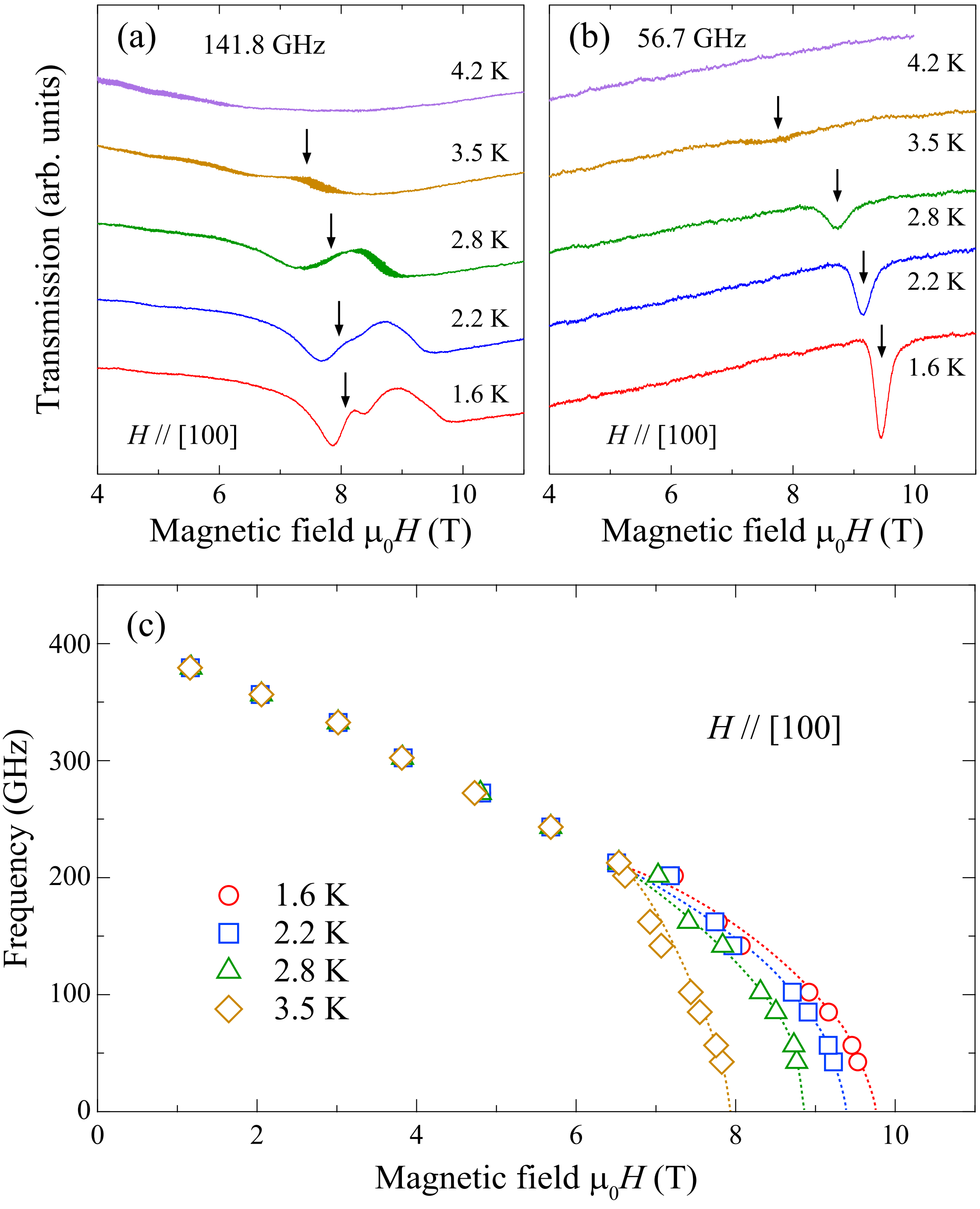

Figure 3-2-10: (a), (b) ESR spectra at designated temperatures below 4.2 K for $H \parallel$ [100]. The ESR signals which are related to the softening mode about $H_c^{[100]}$ are indicated by black arrows. Other signals are omitted for simplicity. (c) The frequency-magnetic field plot of the resonance fields for the softening mode. Dashed lines are guide for the eyes.

by analyzing the magnitude and the phase of the observed signals. Therefore, the resonance field does not correspond with the position where the transmission amplitude is smallest. At low frequencies, for example 56.7 GHz, the resonance field which belongs to the softening mode related to the phase transition changes largely with temperature, but as the frequency increases, for example 141.8 GHz, this change is gradual with temperature. Figure 3-2-10(c) shows the frequency versus resonance fields plot for the softening mode. The result indicates that the resonance fields at low frequencies vary with temperature, and the critical field decreases as the temperature rises.

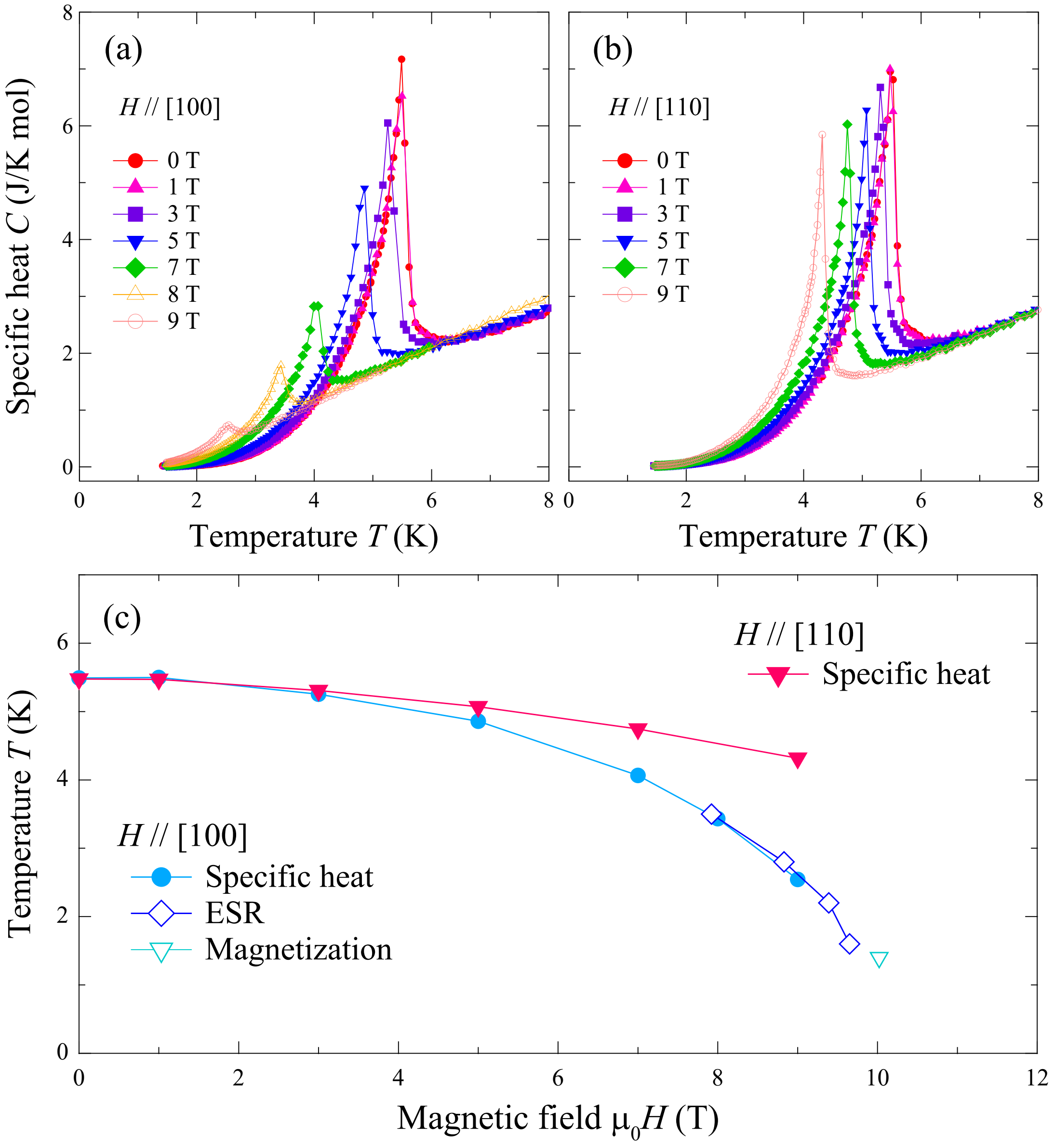

Figure 3-2-11: Temperature dependences of specific heat for (a) $H \parallel [100]$ and (b) $H \parallel [110]$. (c) Phase diagram obtained from specific heat, ESR, magnetization measurements.

Figures 3-2-11(a) and 3-2-11(b) demonstrate the temperature dependences of specific heat for $H \parallel [100]$ and $H \parallel [110]$ in designated magnetic fields. In both [100] and [110] directions, the temperature at the peak of the specific heat decreases as the magnetic field increases. However, the temperature at the peak decreases gradually for $H \parallel [110]$, whereas it drops rapidly toward $H_c^{[100]}$ for $H \parallel [100]$. The peak of the specific heat is λ-shaped, implying the second phase transition to a long-range ordered phase at low temperatures. Fig. 3-2-11(c) reveals the magnetic field versus temperature phase diagram which is assembled with the specific heat peaks and the extrapolated softening fields extracted from the resonance points at low frequencies as shown in Fig. 3-2-10(c) and the anomaly of the field derivative of magnetization in Ref. 65 are plotted. As you can see, the phase boundary of the long-range order is maintained up to the high field for $H \parallel [110]$, while a phase transition occurs near $H_c^{[100]}$ for $H \parallel [100]$.

3-2-3 Numerical Calculation Method

Regarding the effective spin Hamiltonian for $BaCo_2V_2O_8$ in transverse magnetic fields, it has been suggested that four-site periodic effective fields are induced due to the four-fold screw-chain structure [65]. That is, distorted CoO_6 octahedra tilt and magnetic principle axes of each Co^{2+} ion change with a four-site periodicity, so that the g-tensor has off-diagonal elements, leading to effective staggered fields perpendicular to the external magnetic field. Generated effective staggered fields depend on the external magnetic field direction. On applying the external magnetic field along the x direction, the staggered fields appear along both the y and z directions for $H \parallel [100]$, while the staggered field is generated only along the z direction for $H \parallel [110]$, as shown in Figs. 3-2-12(a) and 3-2-12(b). In addition to the above situations, the interchain interactions should be relevant in a real material. Hence, we include the effect of the interchain interactions as well. Thus the effective spin Hamiltonian is given by,

$$\mathcal{H} = \mathcal{H}_{\text{chain}} + \mathcal{H}_{\text{inter}}^{\text{MF}}, \tag{3-2-2}$$

where $\mathcal{H}_{\text{chain}}$ is the spin Hamiltonian (Eq. (3-1-2)) and $\mathcal{H}_{\text{inter}}^{\text{MF}}$ is a mean-field term representing the interchain interaction as explained below. In numerical calculations, we used the parameters in Ref. [65]: $J/k_{\text{B}} = 65$ K, $\varepsilon = 0.46$, $g_{xx} = 2.75$ and $\phi = \pi/4$ for $H \parallel [100]$, $g_{xx} = 2.95$ and $\phi = 0$ for $H \parallel [110]$, $C_y \equiv h_y/g_{xx}H_0 = 0.4$, and $C_z \equiv h_z/g_{xx}H_0 = 0.1\sqrt{2}$, which were evaluated so as to fit the magnetization curve. We also studied with several other values of C_y.

To discuss the effect of the interchain interaction in quasi-1D $BaCo_2V_2O_8$, we incorporated a weak Ising coupling between neighboring chains:

$$\mathcal{H}_{\text{inter}} = J_{\text{inter}} \sum_{j} \sum_{\langle \mu,\nu \rangle} S_{j,\mu}^z S_{j,\nu}^z, \tag{3-2-3}$$

where $S_{j,\mu}^z$ denotes the spin operator at site j in a chain μ. In a chain mean-field treatment, the coupling of a chain μ to its neighboring chains ν is approximated as

$$J_{\text{inter}} \sum_{j} \sum_{\nu} S_{j,\mu}^z S_{j,\nu}^z \simeq J_{\text{inter}} \sum_{j} \sum_{\nu} S_{j,\mu}^z \langle S_{j,\nu}^z \rangle. \tag{3-2-4}$$

By replacing $\langle S_{j,\nu}^z \rangle$ with m_j irrespective of ν, we finally obtain a mean-field Hamiltonian for a single chain,

$$\mathcal{H}_{\text{inter}}^{\text{MF}} = J' \sum_{j} m_j S_j^z, \tag{3-2-5}$$

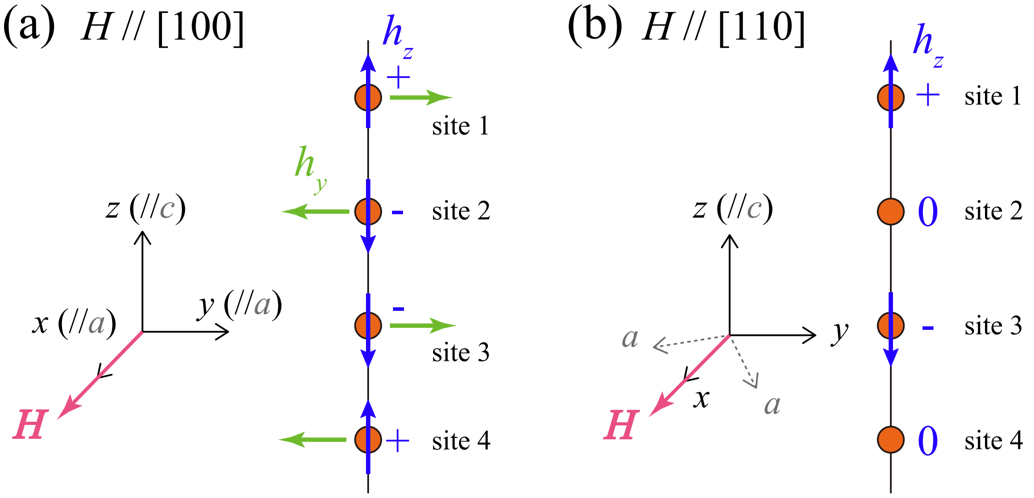

Figure 3-2-12: Schematic view of the effective staggered fields acting on the Co^{2+} ion site for (a) $H \parallel [100]$ and (b) $H \parallel [110]$ in $\mathrm{BaCo_2V_2O_8}$. The h_y and h_z represent the effective staggered fields along the y and z directions, respectively. The x-, y- and z-axes represent the coordinate system when the external magnetic field is applied along the x-direction. (a) The x-, y-, and z-axes correspond to the a-, a-, and c-axes of the tetragonal crystal system, respectively. (b) The x-axis is tilted by 45° relative to the a-axis in the c-plane.

where $J' = zJ_{\mathrm{inter}}$ and z is the number of neighboring chains, while m_j should be determined self-consistently. In a simple Néel state with $m_j = m(-1)^j$, the mean-field term is expressed by $-h_{\mathrm{eff}} \sum_j (-1)^{j+1} S_j^z$, while h_{eff} is determined self-consistently via $J'|\langle S_j^z \rangle| = h_{\mathrm{eff}}$. However, we note that the amplitudes of the staggered magnetic moments would not be equivalent at every site but show a four-site periodicity owing to the h_z term in Eq. (3-1-2). Thus, we assumed a four-site periodic structure for m_j and determined the modulated structure self-consistently.

We performed numerical calculations to examine the magnetic properties of the effective spin model in Eq. (3-2-2) by using the DMRG methods [82, 83]. All the calculations were done with the open boundary condition at zero temperature. Magnetic structures and magnetization data were obtained by standard static DMRG calculations. For magnetic excitations, we calculated the DSSFs given by

$$
\begin{aligned}
S^{\alpha}(q,\omega) = &-\frac{1}{\pi}\mathrm{Im}\langle \psi_{\mathrm{G}} | S_q^{\alpha\dagger} \frac{1}{\omega + E_{\mathrm{G}} - \mathcal{H} + \mathrm{i}\eta} S_q^{\alpha} | \psi_{\mathrm{G}} \rangle \\
&-\frac{1}{\pi}\frac{\eta}{\omega^2 + \eta^2}\langle S_q^{\alpha} \rangle^2,
\end{aligned} \tag{3-2-6}
$$

where S_q^{α} is the Fourier transform of the α component of the spin, q is the momentum, $|\psi_{\mathrm{G}}\rangle$ is the ground state, E_{G} is the ground-state energy, and η is a small broadening factor set to 0.05 in units of J. In the second term, we subtracted a Lorentzian peak at zero energy because of the contribution of a finite magnetic moment induced by the magnetic field. The spectral intensity of $q = 0$, $\pi/2$, and π were calculated by dynamical DMRG runs with 128 sites to compare with experimentally observed ESR spectra. The number of states kept in the renormalization steps was 40, and the truncation error was typically 10^{-3}–10^{-5}, which is sufficient for comparison with the experimental data.

3-2-4 Comparison with Numerical Results

A difference is observed between the spin excitations for $H \parallel [100]$ and $H \parallel [110]$. The magnetic excitation becomes soft at the transition field at about 10 T for $H \parallel [100]$, while no softening of the spin excitation occurs up to the saturation field for $H \parallel [110]$. Therefore, we study the spin excitation behaviors by numerical calculations.

First, we demonstrate the numerical results for $H \parallel [100]$. The observed transition field is about 10 T, but the transition field calculated with the parameters in Ref. 65, *e.g.* the staggered field parameter $C_y = 0.4$, was about 6 T. In the following, we consider two types of ingredients to adjust this transition field. The first one is the inclusion of interchain interactions J', and the second one is the change in the staggered field parameter C_y. Figures 3-2-13 and 3-2-14 display the calculated S_z component at the indicated different Co site and the calculated magnetization curves compared with the experimental one when J' ($C_y = 0.4$ fixed) and C_y ($J'/J = 0$ fixed) are changed, respectively. When the J' increases, the transition field also increases as shown in Fig. 3-2-13(a)–(d), but the magnetization curve hardly changes (Fig. 3-2-13(e)). Therefore, the calculated results with $J'/J = 0.02$ reproduce sufficiently the experimental results.

When J' is fixed to zero, the transition field increases with decreasing the C_y as indicated in Fig. 3-2-14(a)–(d). The magnetization curve does not change much in low magnetic fields below 20 T, but a remarkable change appears in high magnetic fields above 20 T. In this case, we need to take the $C_y = 0.25$ to meet the observed transition field in the low field region, while the parameter $C_y = 0.4$ is required to reproduce the magnetization curve in the high field region (Fig. 3-2-14(e)). The result of magnetostriction along the field direction as shown in the inset of Fig. 3-2-14(e) may be evidence for the crystal distortion to give rise to the change of C_y in the external magnetic field. Therefore, we take the $C_y = 0.25$ in the low magnetic field region.

As demonstrated above, two sets of parameters ($J'/J = 0.02$, $C_y = 0.4$) and ($J'/J = 0$, $C_y = 0.25$) bring about the transition field close to the observed one for $H \parallel [100]$. Accordingly, the magnetic excitation modes for $H \parallel [100]$ are calculated using these parameter sets. We also calculate the magnetic excitation modes up to the saturation field for $H \parallel [110]$ using the same parameters as above to confirm that no softening of the modes takes place below the saturation field as observed by experiment.

Calculated DSSFs at $q = 0$ as a function of magnetic field for $H \parallel [100]$ and $H \parallel [110]$ are shown in Fig. 3-2-15 with experimental energy modes extracted from Figs. 3-2-8(b) and 3-2-9(b). The calculated DSSFs indicate the average of the x and y components according to the experimental situation in Voigt configuration. Since the staggered magnetic field along the y direction disappears for $H \parallel [110]$, only the interchain interaction is taken into account in Figs. 3-2-15(b) and 3-2-15(d). As shown in Figs. 3-2-15(a) and 3-2-15(c), the calculated descending mode goes down toward the transition field at about 10 T, but the intensity for $J'/J = 0.02$ is more prominent. In addition, the calculated excitation mode above the transition field in Fig. 3-2-15(a) agrees well with the experimental one. Accordingly, the experimental results are reproduced better by introducing the interchain interaction J' rather than the change in

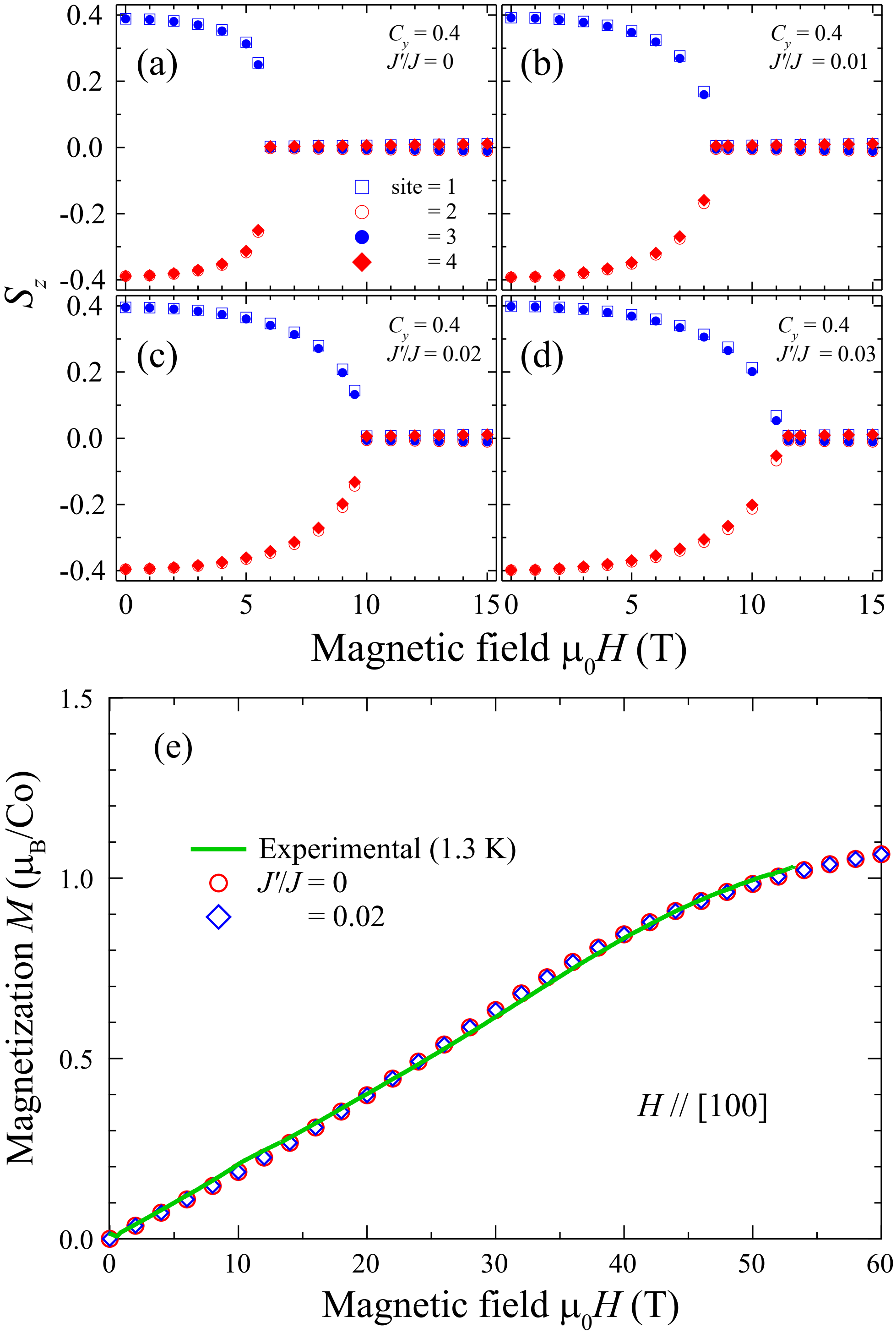

Figure 3-2-13: (a) – (d) Magnetic-field dependences of the z component of the spin (S_z) at each site, calculated for various J' values at $C_y = 0.4$. Open squares, open circles, closed circles, and closed diamonds denote the calculated S_z data for sites 1, 2, 3, and 4, respectively. (e) Magnetization curve obtained from the experiment where the van Vleck contribution is subtracted, and those from the theoretical calculations for $J'/J = 0$ and 0.02 at $C_y = 0.4$. μ_0 is the permeability of vacuum.

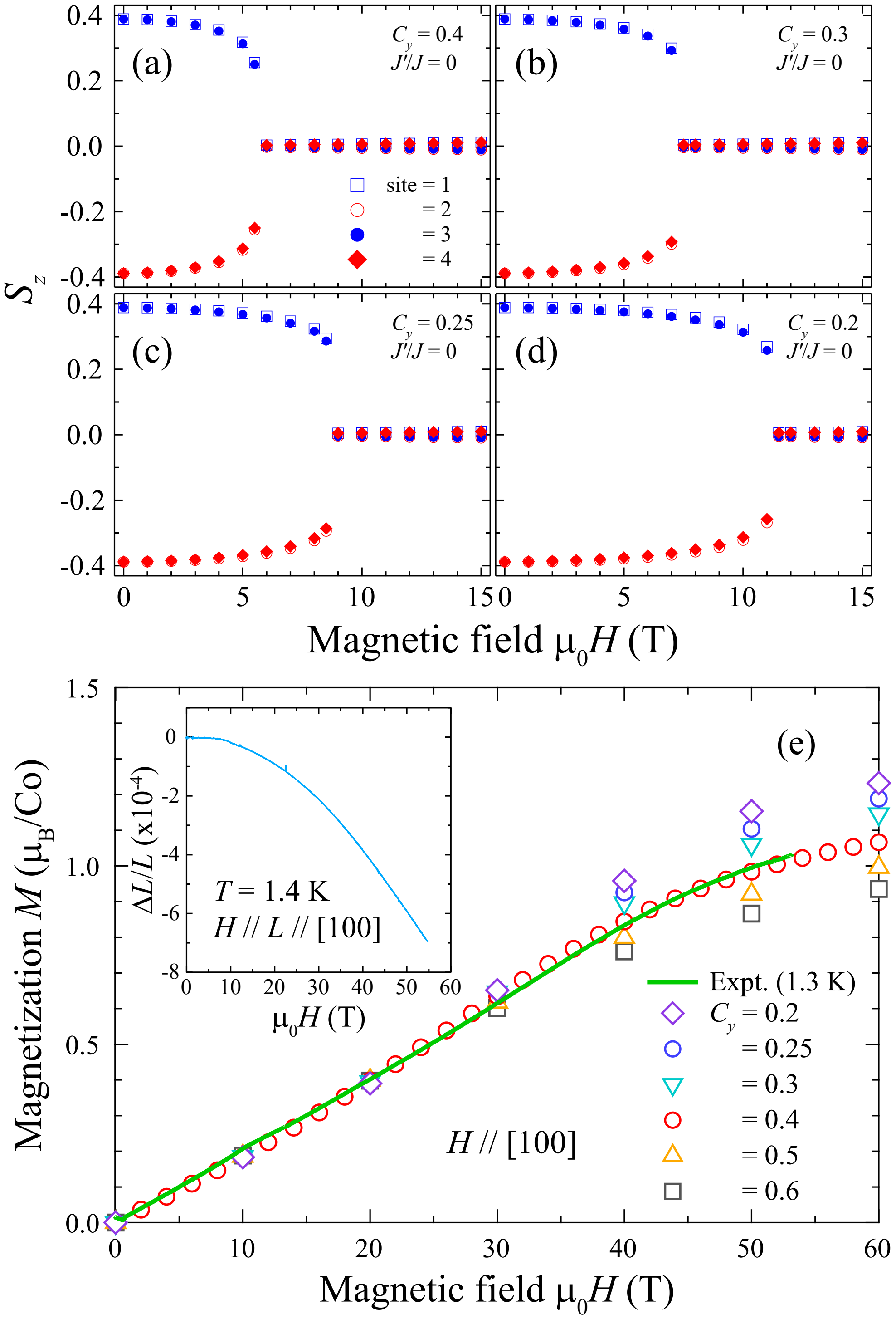

Figure 3-2-14: (a) – (d) Magnetic-field dependences of the z component of the spin (S_z) at each site, calculated for various C_y values at $J'/J = 0$. Open squares, open circles, closed circles, and closed diamonds denote the calculated S_z data for sites 1, 2, 3, and 4, respectively. (e) Magnetization curve obtained from the experiment where the van Vleck contribution is subtracted and those from theoretical calculations for various C_y values at $J'/J = 0$. The inset shows a high-field magnetostriction ($\Delta L/L$) curve for $H \parallel L \parallel [100]$. μ_0 is the permeability of vacuum.

the staggered field parameter C_y. When the interchain interaction is introduced, the transition field is about 10 T, but the transition field for $J'/J = 0$, namely pure 1D case, is about 6 T. This must be consistent with the NMR study on $\mathrm{BaCo_2V_2O_8}$, which shows a 1D quantum critical point at 6 T [71].

In the numerical results, the lowest excitation appears around 400 GHz at 0 T and does not exhibit softening until the saturation field around 40 T for $H \parallel [110]$. This is consistent with the experimental observation, although there are several differences between the numerical results and the experimental observations. The calculated DSSFs do not change much by the interchain interactions. For this direction ($H \parallel [110]$), the transition field coincides with the saturation field. The observed lowest mode decreases with increasing magnetic field below 10 T, while the calculated mode indicates nearly constant up to approximately 10 T and then increases gradually up to approximately 15 T. This behavior is largely different between experiment and calculation. In Fig. 3-2-16, we plot the x component of DSSF for (a) $J'/J = 0.02$ and (c) $J'/J = 0$ with the observed descending modes for $H \parallel [110]$ and its y component for (b) $J'/J = 0.02$ and (d) $J'/J = 0$ with the observed ascending modes for $H \parallel [110]$. As for the descending mode near zero field, the difference between experiment and calculation is considerably large. The reason for this difference in the descending mode and the x component of the DSSF is not clear at present.

As mentioned in Sect. 3-2-2, the energy mode marked by inverted triangles seems to show softening at around 30 T where an anomaly was observed in the magnetization curve (a peak of $\mathrm{d}M/\mathrm{d}H$). This is probably caused by the softening at a different q value like $\pi/2$ as indicated in Figs. 3-2-17(a) and 3-2-17(b). In addition, the observed ESR branch above approximately 40 T is reproduced by the y component of the DSSF in Fig. 3-2-17(d).

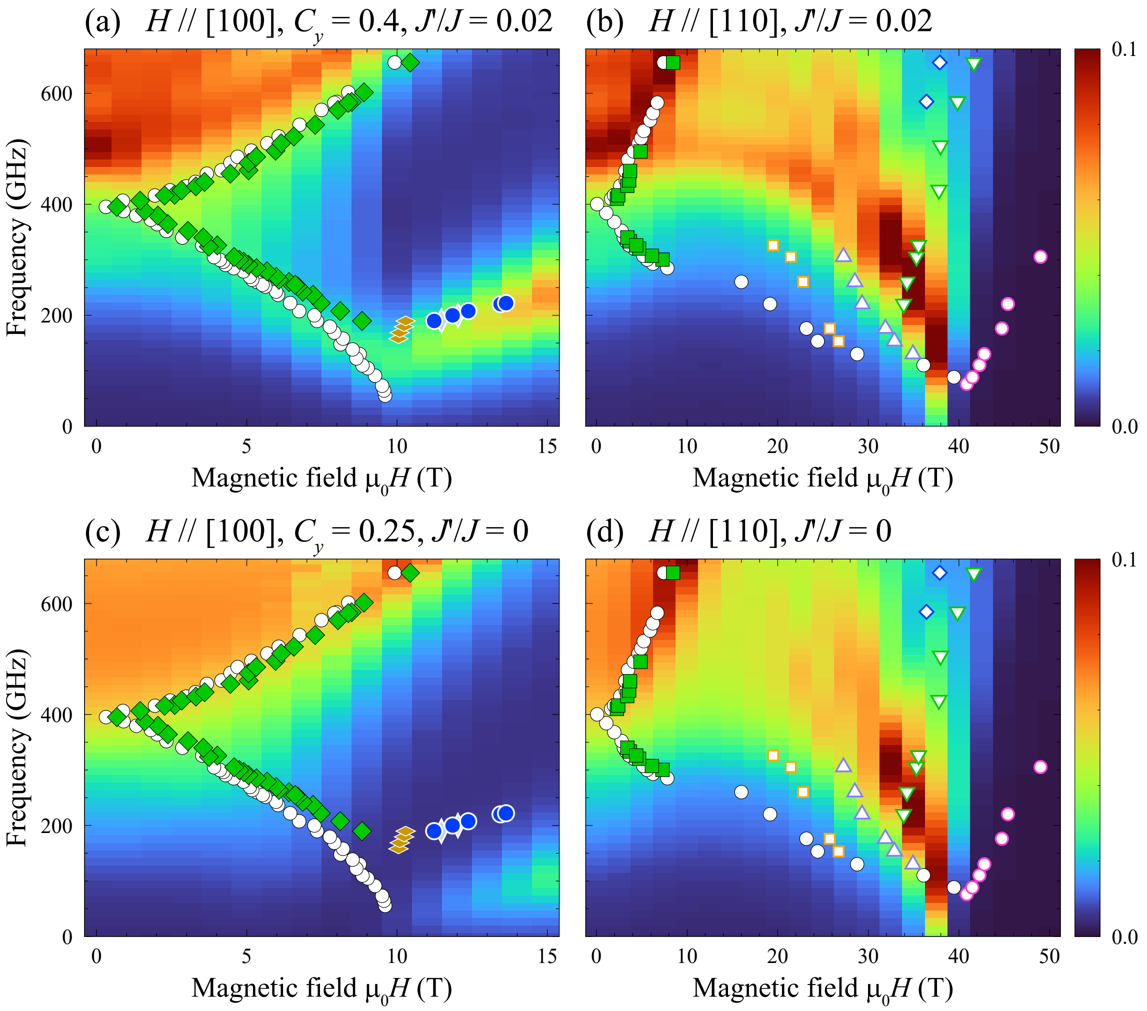

Figure 3-2-15: Frequency versus magnetic field diagram for the averaged DSSFs of the x and y components at $q = 0$ for $H \parallel$ [100] [(a) and (c)] and $H \parallel$ [110] [(b) and (d)] together with the main experimental ESR branches marked by symbols. μ_0 is the permeability of vacuum. The numerical results of the intensity are plotted with the scale given in the color bar. Between (a) and (c), different sets of values for C_y and J' are used in the calculations. For (b) and (d), the same J' values are used as in (a) and (c), respectively.

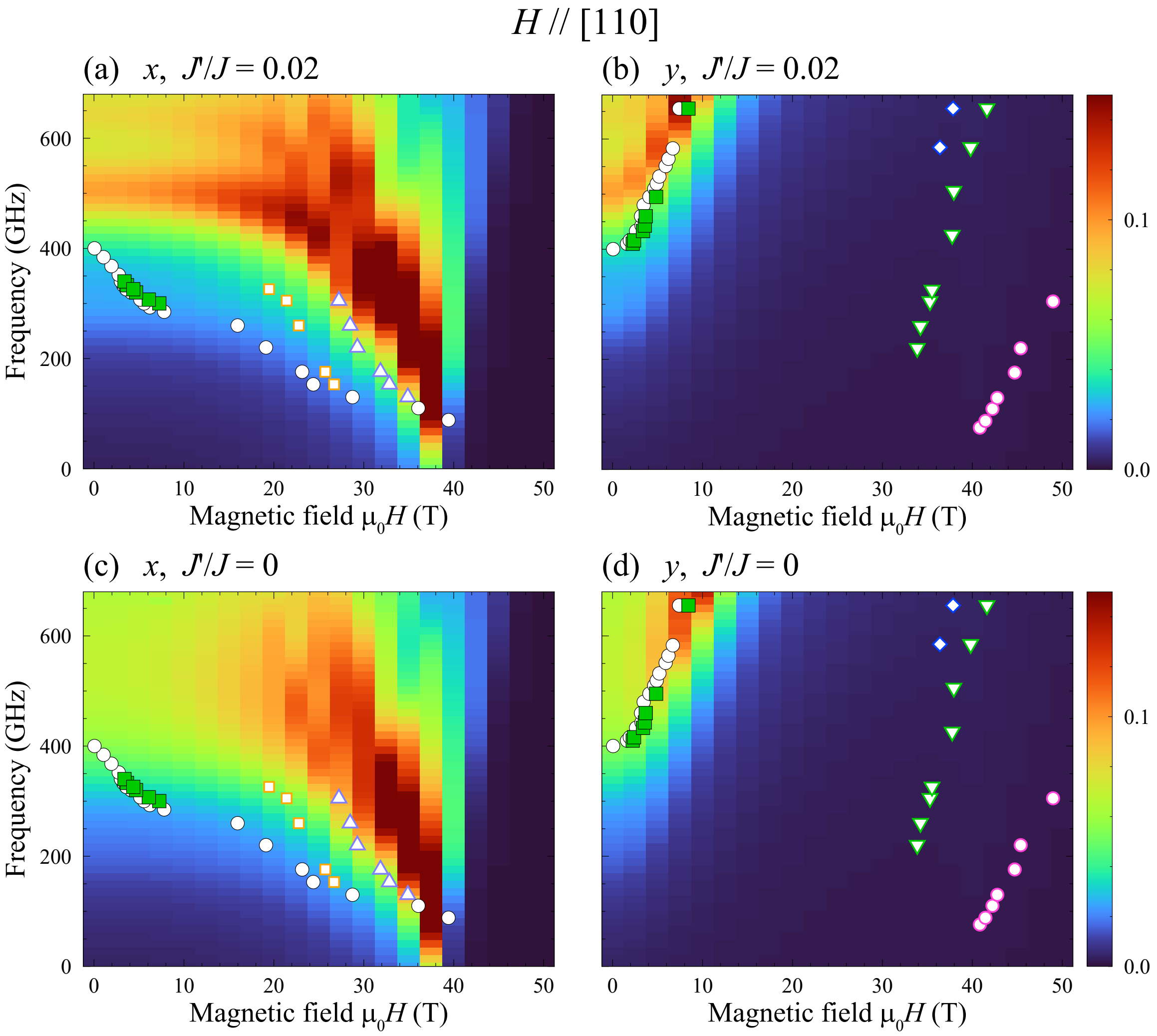

Figure 3-2-16: Frequency versus magnetic field diagram for the x [(a) and (c)] and y [(b) and (d)] components of the DSSFs at $q = 0$ for $H \parallel [110]$ together with the main experimental ESR branches marked by symbols separately for descending modes and ascending ones with increasing magnetic fields. μ_0 is the permeability of vacuum. The numerical results of the intensity are plotted with the scale given in the color bar. Between (a) and (c), different sets of values for J' are used in the calculations. For (b) and (d), the same J' values are used as in (a) and (c).

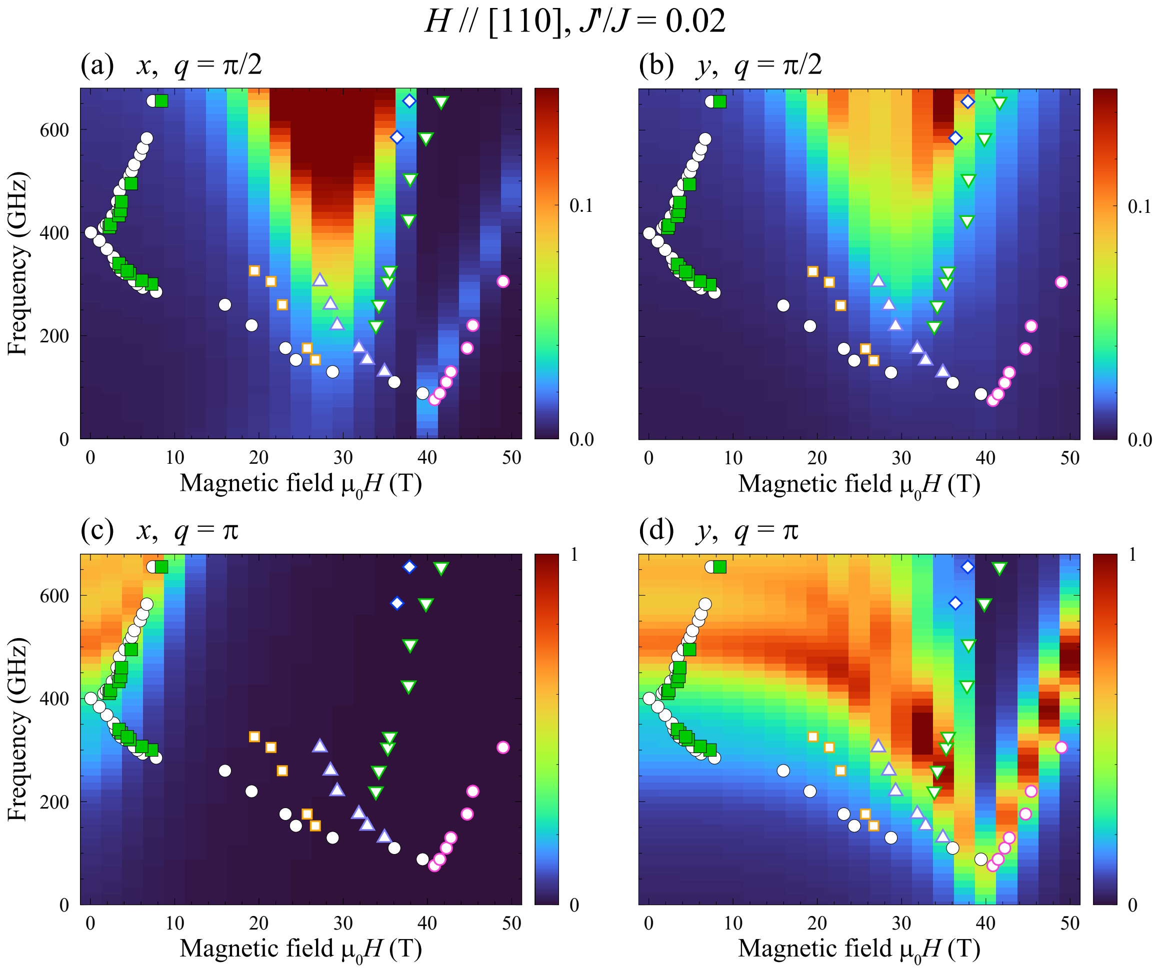

Figure 3-2-17: Frequency versus magnetic field diagram for the x [(a) and (c)] and y [(b) and (d)] components of the DSSFs at $q = \pi/2$ and π for $H \parallel [110]$ together with the main experimental ESR branches marked by symbols. μ_0 is the permeability of vacuum. The numerical results of the intensity are plotted with the scale given in the color bar.

3-3 Discussion

We observed that a longitudinal AF order is quickly suppressed by a transverse staggered field, and that the transition to a disordered state occurs at a relatively low critical field, compared with the transition to a disordered state due to a transverse uniform field. This difference is intuitively understandable in terms of the combined effects of the transverse field and transverse exchange interaction. The transverse staggered field induces a transverse staggered moment, while the transverse exchange interaction develops transverse AF correlations. In other words, they cooperate to stabilize a transverse AF configuration, indicating that the system easily attains the disordered state with the transverse AF configuration. On the other hand, the transverse uniform field induces a transverse uniform moment, competing with the transverse exchange interaction that yields transverse AF correlations. Therefore, a higher field is required to realize a disordered state with a transverse ferromagnetic configuration.

It is worth noting that, even though the critical field differs substantially between the cases $H \parallel [100]$ and $H \parallel [110]$, we observed a descending mode in the $q = 0$ excitation with increasing transverse field for both field directions. This descending mode is in fact characteristic of the transverse Ising model (see Appendix I for theoretical details). To understand this point, it is useful to recall the XY model, whose excitations are described by particle-hole excitations of spinless fermions (spinons) via the Jordan-Wigner transformation. Applying a longitudinal field to the XY model produces a shift in the chemical potential of spinons, leading to a change in the excitation spectrum. The same analysis should be applied to the transverse Ising model after rotating the spin coordination to align the field direction to the z-axis [17,84]. It turns out that the spinon band is composed of particle and hole bands, whose mixing produces an excitation gap. The transverse field shifts the energies of these bands in opposite directions and they eventually split above a critical field. Meanwhile, the excitation gap shrinks, closes at the critical point, and subsequently increases. This scenario holds in the present XXZ model with effective staggered fields, while the critical field depends on ε and C_y. The difference between $H \parallel [100]$ and $H \parallel [110]$ is attributed to the presence of C_y. Indeed, taking into account Eq. (A1-9) in Appendix I, the critical field for $H \parallel [100]$ should decrease with increasing C_y, consistent with observations in Fig. 3-2-14.

Finally, we discuss the difference in the disordered states above the transition field between two different field directions, namely, longitudinal $H \parallel [001]$ and transverse $H \parallel [100]$. Above the transition field for $H \parallel [001]$, a TL spin liquid state appears [60], where the linear dispersion moves on the momentum axis and the gapless momentum is related to the magnetization. Figure 3-3-1 shows the DSSF $S(Q, E)$ calculated by the DMRG method using the Hamiltonian of Eq. (3-1-2) with the parameters in Ref. 65 for $H \parallel [100]$ [67]. Here, $S(Q, E)$ and $S(q, \omega)$ are identical. Since no interchain interaction is included in this calculation, 10 T is located above the transition field H_{c} (6 T). Focusing on the spectra at 10 T, the spin gap opens at any Q value in each component. Figure 3-3-1(g) and 3-3-1(h) indicate the intensities of DSSFs at $Q = 0$ for S_x and at $Q = \pi$ for S_z, respectively. Both pictures clearly show a peak at a finite energy, evidencing for the spin gap opening. Therefore, for $H \parallel [100]$, above H_{c} a disordered state is not a TL spin liquid and may be close to a field-induced ferromagnetic state or a paramagnetic state. This difference in behavior for these different field directions is remarkable.

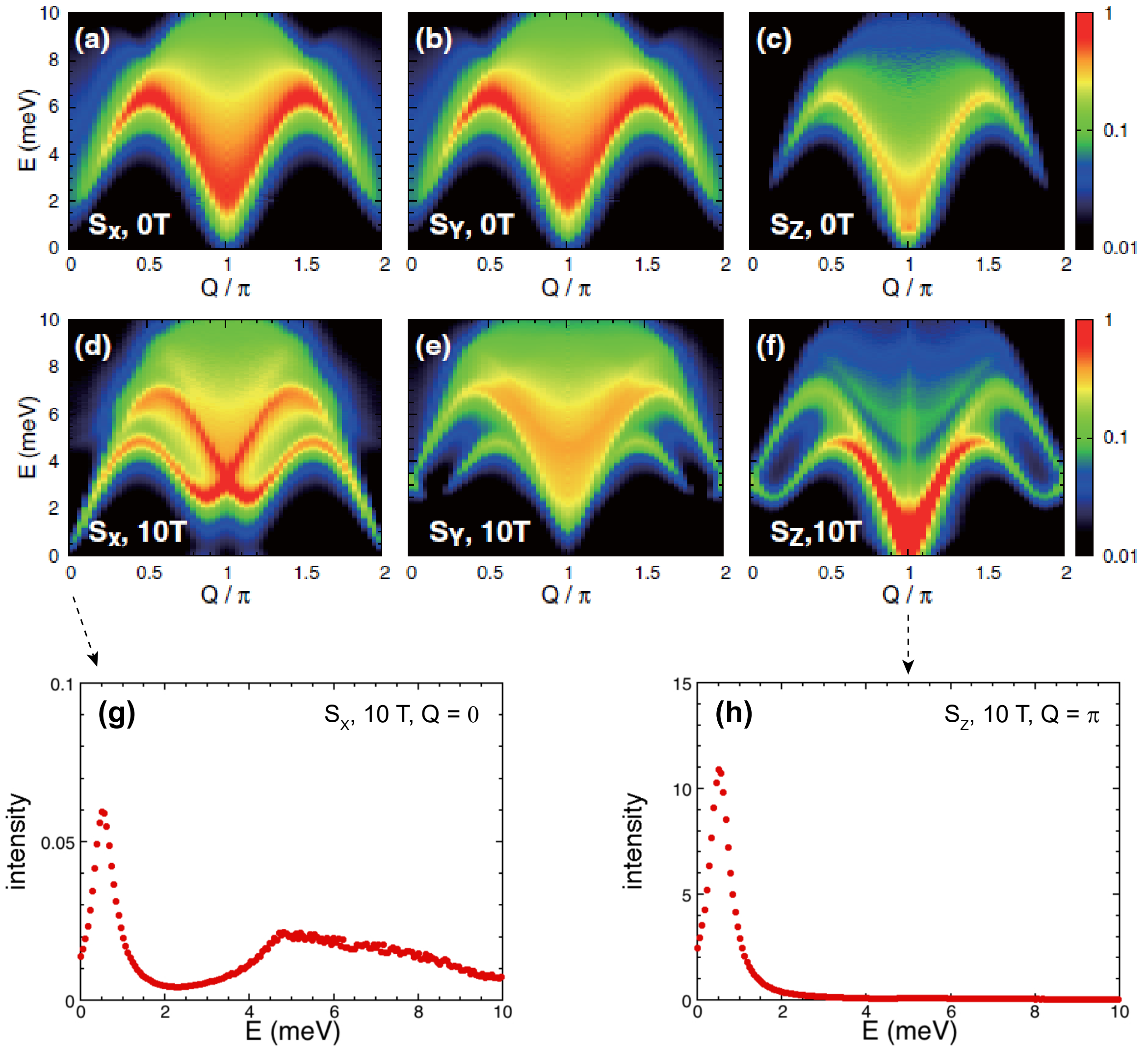

Figure 3-3-1: Each component of the DSSF $S(Q,E)$ calculated by the DMRG method using the Hamiltonian (Eq. (3-1-2)) with the parameters in Ref. 65 for $H \parallel [100]$. (a)–(c) and (d)–(f) are at 0 T and 10 T as located above the transition field (6 T), respectively. (g) and (h) represent the intensity of the x component of $S(Q,E)$, S_x, at $Q = 0$ and that of the z component of $S(Q,E)$, S_z, at $Q = \pi$ both at 10 T as a function of energy E (meV), respectively. In each panel, a peak appears at a finite energy, indicating that the spin gap opens at any Q value by combining with the energy dispersions in all the figures at 10 T ((d)–(f)). (a)–(f) are Quoted from [67]. (g) and (h) are Quoted from [85].

3-4 Conclusion

In summary, we have performed magnetic susceptibility, high-field multi-frequency ESR, specific heat, and the magnetostriction measurements on the $S = 1/2$ quasi-1D Ising-like antiferromagnet $\mathrm{BaCo_2V_2O_8}$ in the transverse fields $H \parallel [100]$ and $H \parallel [110]$.

A softening of the lowest ESR branch was observed near $H_\mathrm{c} = 10$ T as the order-disorder transition field for $H \parallel [100]$, whereas no softening was observed up to the saturation field for $H \parallel [110]$. The observation of this softening at H_c was reproduced by DMRG calculations of DSSF $S(q, \omega)$ at $q = 0$ using two parameter sets, one with the staggered magnetic field parameter $C_y = 0.4$ and the interchain interaction $J'/J = 0.02$, and the other with $C_y = 0.25$ and $J'/J = 0$.

The magnetization curve for $H \parallel [100]$ can be reproduced using $C_y = 0.4$, regardless of the interchain interaction. The change in C_y at low fields for the latter case is considered from a large change in magnetostriction. The agreement between the experiment and the calculation is satisfactory in the former case. We have discussed elementary excitation within a spinon context by using the Jordan-Wigner transformation. The descending mode observed in the ESR measurements is regarded as the lowest particle-hole spinon excitation.

We compared the main ESR branches for $H \parallel [110]$ with the calculated DSSFs $S(q, \omega)$ at $q = \pi/2$ and π. The DSSFs at $q = \pi/2$ seem to be related to the ESR branches which show softening at around 30 T where an anomaly was observed in the field derivative of the magnetization. In addition, the observed ESR branch above approximately 40 T is reproduced in the DSSF at $q = \pi$.

Finally, we discussed the disordered state above the transition field for $H \parallel [100]$. Above the transition field for $H \parallel [001]$, a TL spin liquid state is realized, whereas a disordered state above the transition field for $H \parallel [100]$ may be close to a field-induced ferromagnetic state or a paramagnetic state, because the spin gap opens at any q from the calculated DSSFs $S(q, \omega)$.

4 $S = 1/2$ Honeycomb-Lattice Antiferromagnet $Cu_2(pymca)_3(ClO_4)$

4-1 Introduction

4-1-1 Fundamental Properties of $M_2(pymca)_3(ClO_4)$ (M=Fe, Co, Ni, Cu)

As mentioned in the last part of Sect. 1-2-2, the pymca (pyrimidine-2-carboxylate) is used as an appropriate organic bridging ligand to construct a honeycomb-lattice magnet by connecting transition-metal ions. Since the exchange interactions in molecule-based magnets are caused via bridging ligands, the dimensionality and the topology of the magnets strongly depend on the nature of bridging ligands. Therefore, the selection of appropriate bridging ligand is important for the fabrication of honeycomb-lattice magnets. The oxalate (ox, ${C_2O_4}^{2-}$) and pyrimidine groups have been used extensively in the construction of magnets with interesting structural features (three-dimensional, layered and chain structures). For example, the bimetallic oxalate compound $N(C_5H_{11})_4MnFe(ox)_3$ has a honeycomb-lattice structure of Mn and Fe ions bridged by ox groups and behaves as a two-dimensional (2D) ferrimagnet [86]. The pymca is structurally analogous to the ox and pyrimidine bidentate bridging ligand.

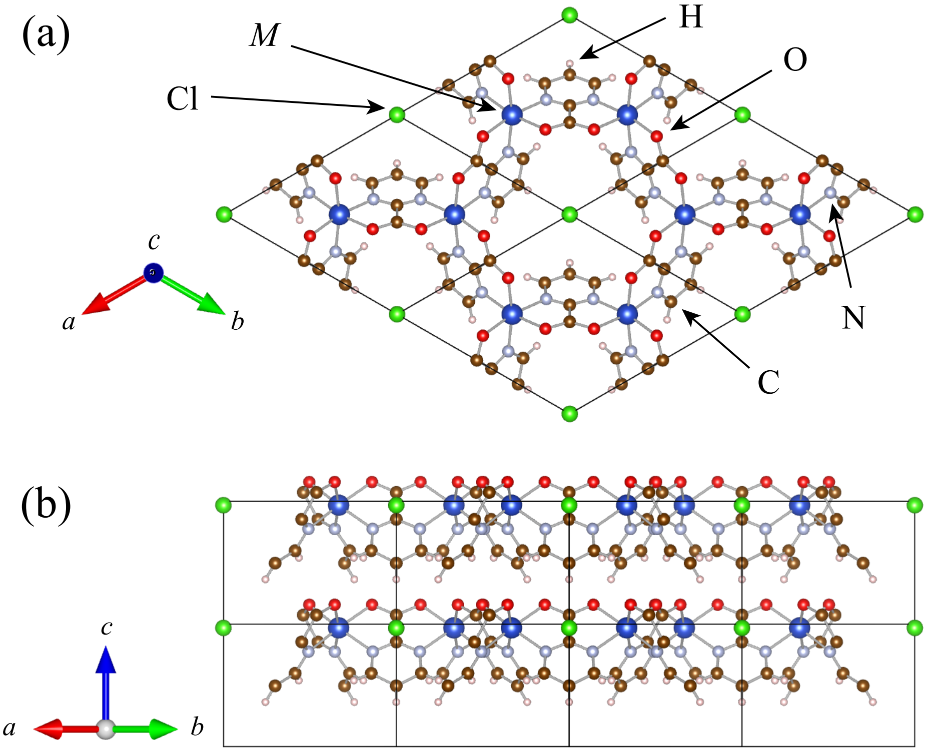

Figure 4-1-1: Crystal structure of $M_2(pymca)_3(ClO_4)$ (M=Fe,Co,Ni,Cu) [87,88], drawn by using the VESTA software program [58]. The picture is the view projected (a) from the c-axis to the ac-plane, and (b) from the direction perpendicular to the c-axis. Oxygen atoms on ${ClO_4}^-$ are omitted for clarity. The black thin solid lines indicate the unit cells. As will be described later, a new crystal structure has been proposed for $Cu_2(pymca)_3(ClO_4)$.

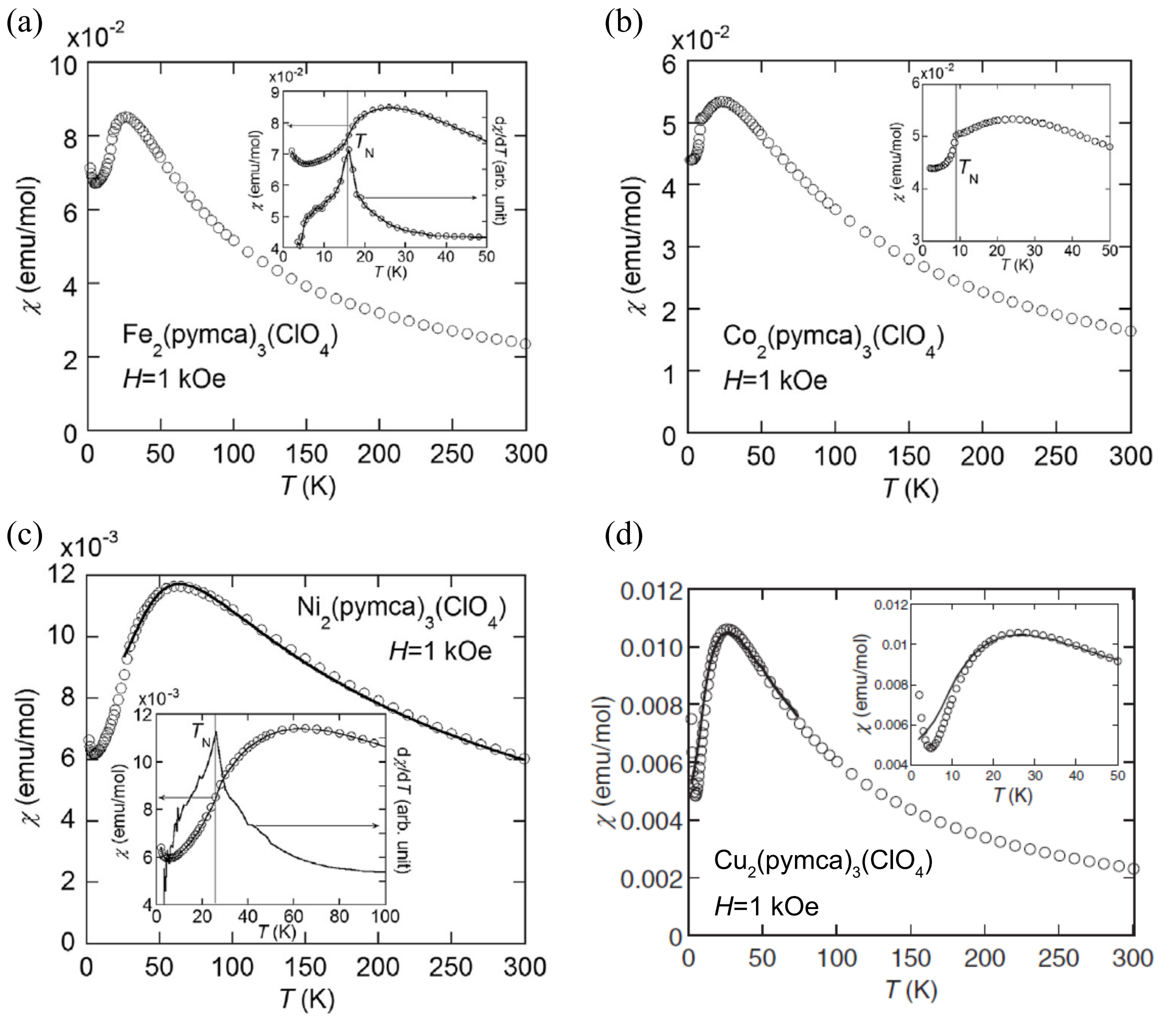

Figure 4-1-2: Temperature dependences of the magnetic susceptibility for M_2(pymca)$_3$(ClO$_4$) (M= (a)Fe, (b)Co, (c)Ni, (d)Cu) polycrystalline samples. The solid lines in (c) and (d) represent the calculated susceptibilities for the $S = 1$ and $S = 1/2$ honeycomb-lattice Heisenberg antiferromagnets with the fitting parameters shown in Table 4-1-1. Quoted from [87, 88].

Honda *et al.* reported the structures and the magnetic properties of M_2(pymca)$_3$(ClO$_4$) (M=Fe, Co, Ni, and Cu) [87, 88]. All these compounds except for Cu compound crystallize in a trigonal crystal system, space group P31m at room temperature, and their crystal structures are honeycomb-lattice layers stacked along the c-axis as shown in Fig. 4-1-1. Cu$_2$(pymca)$_3$(ClO$_4$) was first recognized as the same trigonal crystal system, but later its structure was found to be more complex as described in the next subsection. In 2D honeycomb-lattice systems, spin quantum number and anisotropy of magnetic ions play important roles in magnetic ordering.

Figure 4-1-2 show the temperature dependences of the magnetic susceptibilities on polycrystalline samples of the aforementioned four compounds [87, 88]. These exhibit a round maximum, which is characteristic of low-dimensional antiferromagnets. In Figs. 4-1-2(c) and 4-1-2(d), the solid lines indicate the calculated susceptibilities for the $S = 1$ and $S = 1/2$ honeycomb-lattice Heisenberg antiferromagnet model. The

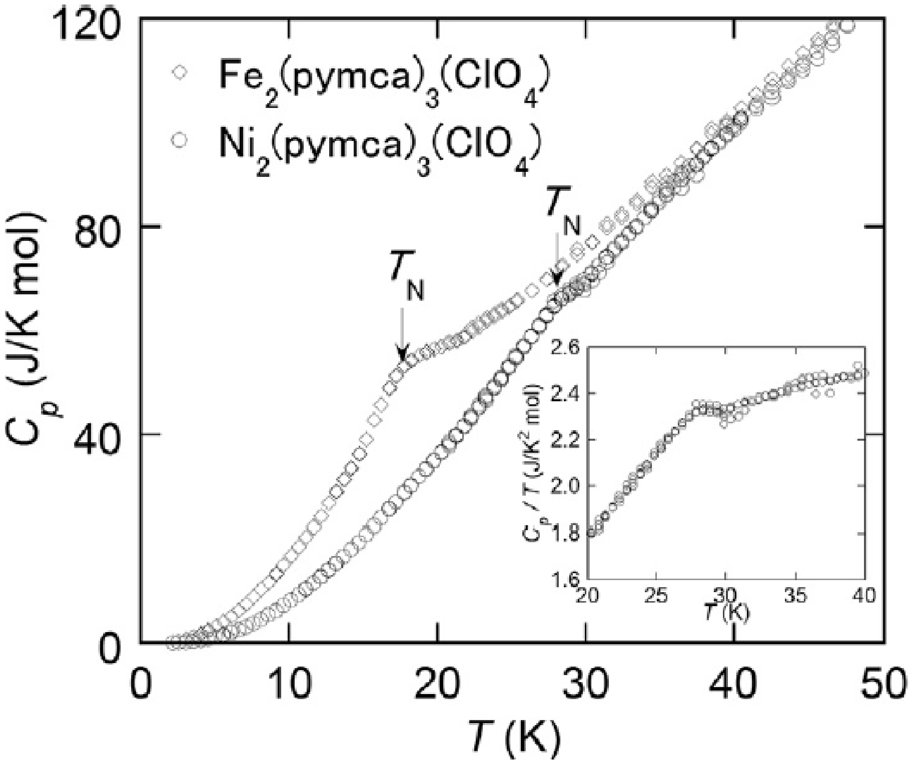

Figure 4-1-3: Temperature dependences of the specific heat for Fe(pymca)$_3$(ClO$_4$) and Ni(pymca)$_3$(ClO$_4$) in zero field. The inset displays the expanded figure of low temperature part near the AF transition for the Ni compound. Quoted from [88].

Table 4-1-1: Magnetic parameters for Fe$_2$(pymca)$_3$(ClO$_4$), Co$_2$(pymca)$_3$(ClO$_4$), Ni$_2$(pymca)$_3$(ClO$_4$), and Cu$_2$(pymca)$_3$(ClO$_4$) [87,88].

	Fe$_2$X$^{a)}$	Co$_2$X	Ni$_2$X	Cu$_2$X
C (emu/K mol)	7.30	6.44	2.43	0.77
Θ_{CW} (K)	−50.1	−74.1	−120.2	−26.8
J/k_{B} (K)	–	–	44.0	37
T_{N} (K)	17.5$^{c)}$	8.9$^{b)}$	28.0$^{c)}$	–

a) X stands for (pymca)$_3$(ClO$_4$)
b) Determined by magnetic susceptibility measurements
c) Determined by specific heat measurements

spin Hamiltonian based on this model is written as,

$$\mathcal{H} = J \sum_{j} \boldsymbol{S}_j \cdot \boldsymbol{S}_{j+1} - g\mu_{\mathrm{B}} H \sum_{j} \boldsymbol{S}_j \tag{4-1-1}$$

where $\boldsymbol{S}_j$ is Heisenberg spin in the honeycomb layer, J is the intralayer nearest-neighbor exchange constant, μ_{B} is the Bohr magneton, and g is the g-factor of the transition metal ions. Using $S = 1$, $J/k_{\mathrm{B}} = 44.0$ K, and $g = 2.18$ for the Ni compound, and $S = 1/2$, $J/k_{\mathrm{B}} = 37$ K, and $g = 2.08$ for the Cu compound, the model calculations provide reasonable reproduction of the experimental data.

The magnetic susceptibility of the Co compound has a clear bend at 8.9 K showing an AF transition. The Fe and Ni compounds also have AF transitions at 17.5 K and 28.0 K, respectively, from the specific heat measurements as shown in Fig. 4-1-3 [88]. While, unlike the three honeycomb compounds, the Cu compound shows no magnetic LRO down to 2 K from the magnetic susceptibility measurements in Fig. 4-1-2(d), although distant exchange interactions are not expected from its crystal structure. The magnetic parameters of the four honeycomb-lattice compounds are shown in Table 4-1-1.

4-1-2 Crystal Structure of $\mathbf{Cu_2(pymca)_3(ClO_4)}$

Normally, the orbital correlation energy is an order of magnitude larger than the spin exchange interaction, and thus an orbital ordering at a high temperature is accompanied by cooperative Jahn–Teller distortion. On the contrary, if the orbital energy is reduced to the same scale as the spin exchange interaction, leading to a novel spin-orbital entangled state, a possible quantum spin-orbital liquid.

As mentioned above, the crystal structure of $\mathrm{Cu_2(pymca)_3(ClO_4)}$ was initially regarded as a regular honeycomb-lattice, and the magnetic order was not confirmed down to 2 K. Thus $\mathrm{Cu_2(pymca)_3(ClO_4)}$ is expected to be the second example of a quantum spin-orbital liquid material composed of $\mathrm{Cu^{2+}}$ ions, followed by 6H-$\mathrm{Ba_3CuSb_2O_9}$ [89–93]. However, its structure, derived from synchrotron radiation X-ray diffraction data, was determined to be a rhombohedral system (space group $R3c$ with lattice constants $a = 16.6120(9)$ Å, $c = 35.486(4)$ Å) as being a distorted honeycomb-lattice at 100 K [94]. More specifically, it contains two crystallographically inequivalent Cu sites (denoted Cu1 and Cu2), separated by atomic distances 5.5932(11), 5.5112(12), and 5.5083(15) Å as shown in Fig. 4-1-4. From this finding, there are three types of hexagonal ring in the honeycomb layer. The latter two Cu-Cu distances are close to each other. Therefore, this compound can be regarded as magnetically weakly coupled hexagons.

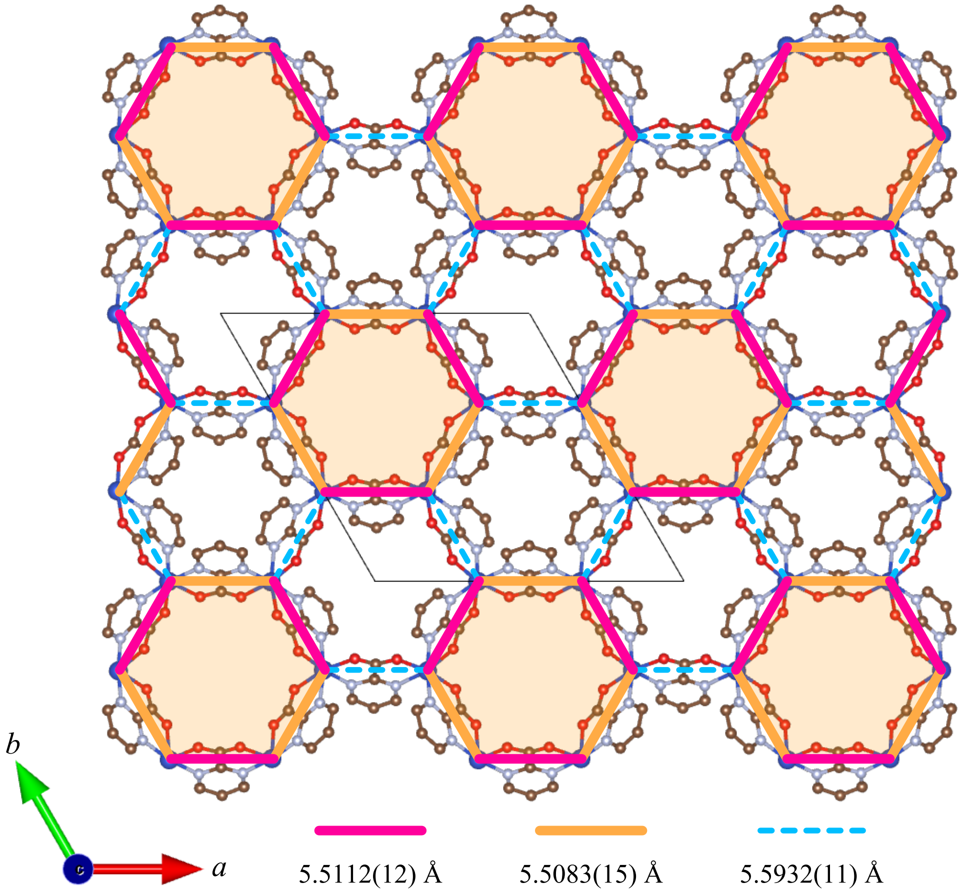

Figure 4-1-4: Schematic drawing of honeycomb-layer of $Cu_2(pymca)_3(ClO_4)$ determined by synchrotron radiation X-ray diffraction analysis at 100 K [94]. Hydrogen atoms and ClO_4^- ions are omitted for clarity. The black thin solid line indicates the unit cell. Three kinds of Cu−Cu distances are drawn by different colors.

4-1-3 Purpose of This Study

It was found that $Cu_2(pymca)_3(ClO_4)$ does not possess a regular honeycomb-lattice structure and shows no AF LRO down to 2 K. Therefore, we would like to evaluate the exchange interactions between the neighboring Cu ions and clarify the reason why this compound exhibits no LRO down to 2 K by magnetic measurements in high magnetic fields.

4-2 Experiment and Calculation

4-2-1 Sample preparation

Polycrystalline $Cu_2(pymca)_3(ClO_4)$ samples used in this study were provided by Associate professor Z. Honda at Saitama University. This compound was synthesized by a hydrothermal reaction of 2-cyanopyrimidine (2-cp) with Copper(II) perchlorate hexahydrate ($Cu(ClO_4)_2 \cdot 6\,H_2O$). By putting the materials into a Teflon-lined autoclave as depicted in Fig. 4-2-1(a), and sealing the autoclave and heating them at 383 K in an electric furnace for 24 hours under autogenous pressure followed by slow cooling to room temperature, the hydrolysis of 2-cp and the consequent formation of polynuclear pymca bridging were caused. As a result, $Cu_2(pymca_3(ClO_4)$ samples were synthesized [87]. The chemical reaction formula is given below,

$$3\,(2\text{−cp}) + 2\,Cu(ClO_4)_2 + 6\,H_2O \longrightarrow Cu_2(pymca)_3(ClO_4) + 3\,NH_4ClO_4. \qquad (4\text{-}2\text{-}1)$$

By this procedure, it is possible to grow a very small single crystal as shown in Fig. 4-2-1(b), but since it is too small to be used in the following experiments, polycrystalline samples which were characterized by XRD were used.

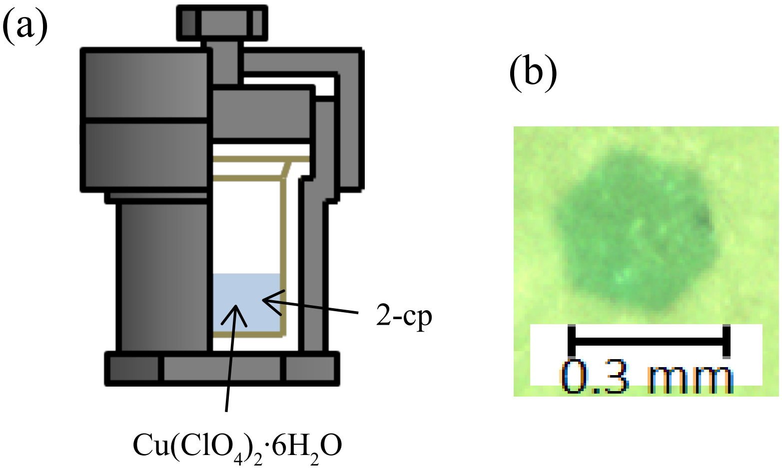

Figure 4-2-1: (a) Schematic view of a Teflon-lined autoclave for hydrothermal synthesis. Copper(II) perchlorate hexahydrate ($Cu(ClO_4)_2 \cdot 6\,H_2O$), 2-cyanopyrimidine (2-cp), and H_2O were put into an autoclave, sealed and heated in an electric furnace. (b) Photo of a single crystal of $Cu_2(pymca)_3(ClO_4)$. In the experiments, polycrystalline samples were used because of the tiny single crystals.

4-2-2 Experimental Results

Figure 4-2-2 represents the temperature dependence of the magnetic susceptibility $\chi = M/H$ (where M is the magnetization and H is the external magnetic field) of a polycrystalline $Cu_2(pymca)_3(ClO_4)$ sample (open squares) measured at $\mu_0 H = 0.1$ T between 1.9 and 300 K using a superconducting quantum-interference device (SQUID) magnetometer (Quantum Design MPMS XL-7). The magnetic susceptibility shows a broad maximum near 25 K and a steep increase below 5 K, reflecting the susceptibility from a paramagnetic impurity. To obtain the intrinsic magnetic susceptibility of

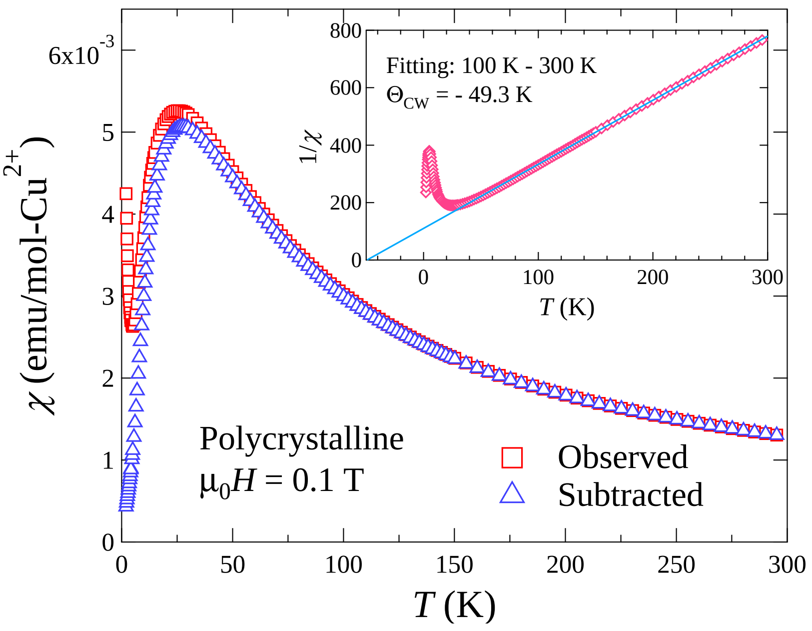

Figure 4-2-2: Temperature dependence of magnetic susceptibility $\chi\,(= M/H)$ and inverse magnetic susceptibility (inset) of a polycrystalline sample of $Cu_2(pymca)_3(ClO_4)$. The open squares and triangles represent the measured magnetic susceptibility and the magnetic susceptibility subtracted the paramagnetic-impurity contribution, given by the Curie term from the measured data, respectively. In the inset, the solid line is a linearly-fitted result from 100 K to 300 K, as the Curie-Weiss law.

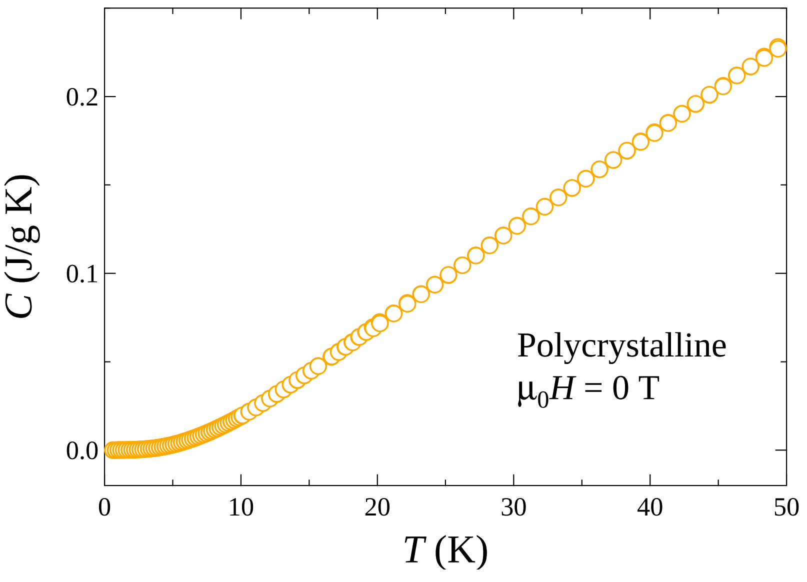

Figure 4-2-3: Temperature dependence of the specific heat C of a polycrystalline sample of $Cu_2(pymca)_3(ClO_4)$ in zero field down to 0.6 K.

the sample, we subtracted the paramagnetic-impurity component, given by the Curie term, from the measured magnetic susceptibility (open squares). For this calculation, we assumed the paramagnetic component with $S = 1/2$ expressed as $\alpha C/T$, where C is the Curie constant with the g-value (2.13) determined by multi-frequency ESR as described below, and thus the impurity concentration is extracted as $\alpha = 1.8$ %. The resulting intrinsic magnetic susceptibility shows a monotonic decrease toward zero upon cooling from 20 K. From the Curie-Weiss fitting of the reciprocal susceptibility between 100 K and 300 K, we obtained the Weiss temperature $\Theta_{\mathrm{CW}} = -49.3$ K as shown in the inset of Fig. 4-2-2, indicating that AF interactions are dominant in this compound. Figure 4-2-3 indicates the temperature dependence of the specific heat (open circles) measured in zero magnetic field, using a Quantum Design PPMS measurement system by the relaxation method. No anomalies and no peaks were observed down to 0.6 K, thus providing no evidence for a long-range magnetic order.

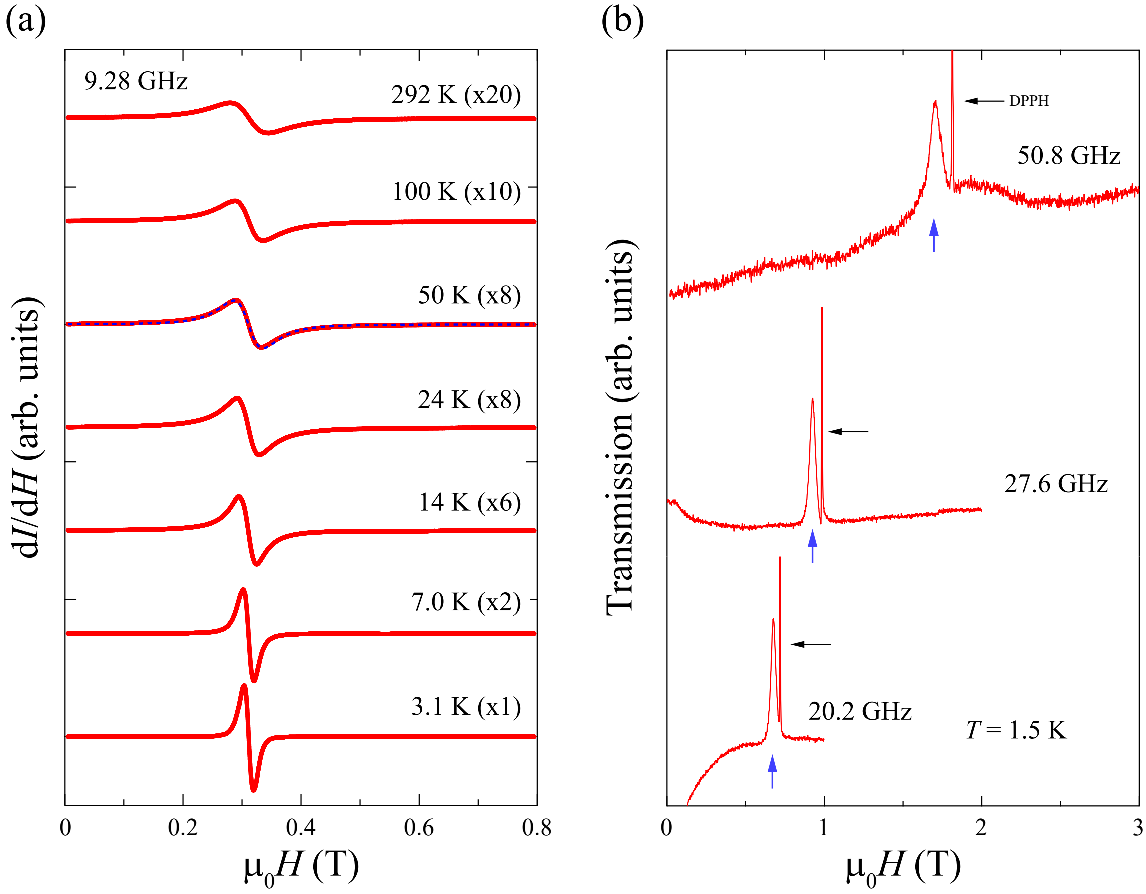

Figure 4-2-4: (a) X-band spectra of a polycrystalline $Cu_2(pymca)_3(ClO_4)$ sample measured at designated temperature. The blue dashed line at 50 K indicates a fit to a single Lorentzian function. The numbers with a cross inside the parentheses next to the temperatures represent scaling factors to improve the readability of the spectra. (b) ESR spectra of a polycrystalline $Cu_2(pymca)_3(ClO_4)$ sample at 1.5 K. The blue arrows represent the ESR resonance fields. The sharp peaks indicated by the black arrows are signals from DPPH.

X-band ESR spectra for a polycrystalline $Cu_2(pymca)_3(ClO_4)$ sample at the speci-

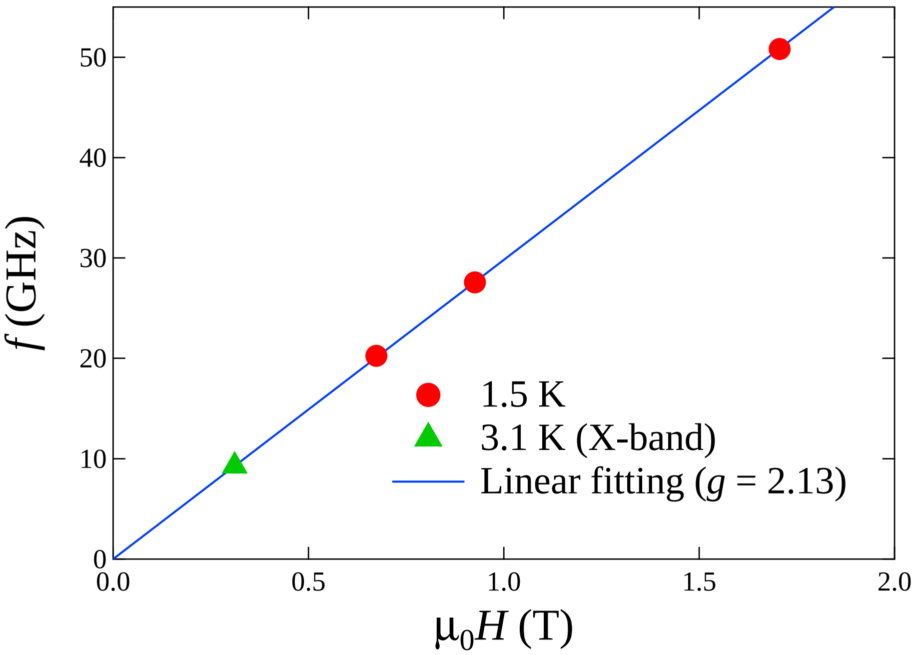

Figure 4-2-5: Resonant-frequency versus resonance-magnetic-field plot of a polycrystalline $Cu_2(pymca)_3(ClO_4)$ sample. The red circles and the green triangle represent the resonance points at 1.5 K and 3.1 K, respectively. The blue solid line is the result of linear fit with $g = 2.13$.

fied temperatures, which were obtained by using an X-band ESR spectrometer (Bruker EMX) with a He-flow cryostat (Oxford Instruments), are shown in Fig. 4-2-4(a). The blue dashed line at 50 K indicates a fit to a single Lorentzian function, indicative of an exchange-coupled system. ESR spectra at various temperatures, not only at 50 K, can be fitted to a single Lorentzian function. The g-value deduced from the linear fits at the lowest temperatures (1.5 K and 3.1 K), $g = 2.13$, is almost temperature-independent between 3 K and 292 K. Figure 4-2-4(b) represents ESR spectra at 1.5 K with DPPH. Since a resonator was used for the measurement, the transmission intensity is increased at resonant field.

The frequency versus resonant field-plot was obtained from these measurements as shown in Fig. 4-2-5. Each point can be fitted well with a linear line passing through the origin as paramagnetic resonance with $g = 2.13$, implying no magnetic order which is consistent with the result of the specific heat measurement. As suggested by the increase in magnetic susceptibility at low temperatures, the ESR signals arising from paramagnetic impurities are observed at low temperatures.

Figures 4-2-6(a) and 4-2-6(b) demonstrate the high-field magnetization curves for a polycrystalline sample of $Cu_2(pymca)_3(ClO_4)$ at 1.4 K and 4.2 K and their field derivatives of the magnetization curves at 1.4 K, respectively, measured in pulsed magnetic fields. Three step-like increases are observed in the magnetization curve at 1.4 K, and are reflected in the three peaks in the corresponding $\mathrm{d}M/\mathrm{d}H$. The magnetization values in the almost flat regimes near 35 T and 60 T match to one third and two thirds of the saturation value evaluated from the g-value (2.13) of this compound. Even the maximum observed magnetization value does not reach the saturation value

($1.07\mu_B/Cu^{2+}$). This magnetization curve is not explained by the magnetization of the $S = 1/2$ simple honeycomb-lattice antiferromagnet (HLA) with uniform exchange interactions, as shown later to indicate a monotonic increase up to the saturation field.

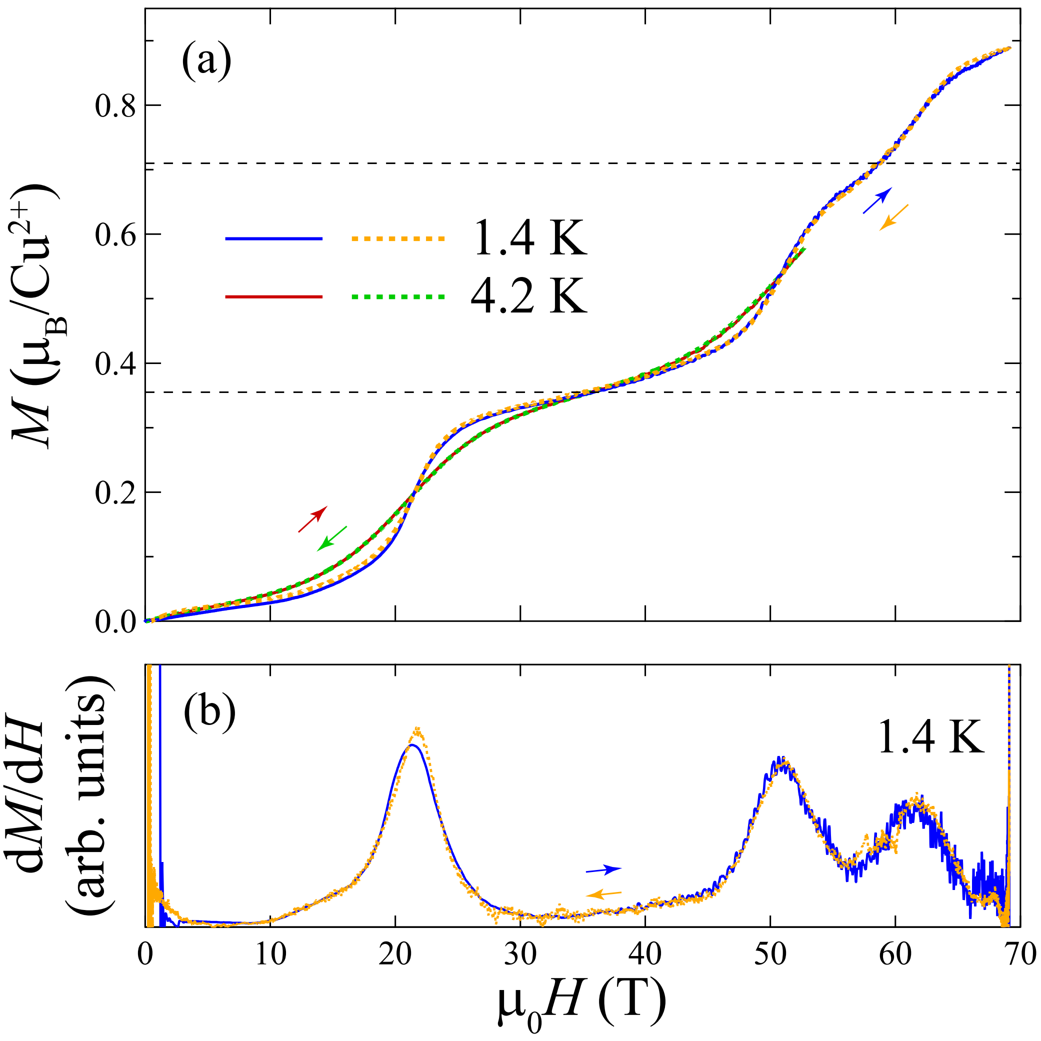

Figure 4-2-6: (a) High-field magnetization (M) for a polycrystalline $Cu_2(pymca)_3(ClO_4)$ sample in magnetic fields of up to 70 T at 1.4 K and up to 50 T at 4.2 K. The black dashed lines correspond to one-third and two-third of the saturation magnetization expected from the g-value. (b) The field derivatives of the magnetization curves (dM/dH) at 1.4 K. In both figures, the solid and dotted lines indicate the field-ascending and descending processes, respectively, as represented by the arrows.

4-2-3 Numerical Calculation Method

Next, observed magnetization curves were analyzed by a quantum Monte Carlo (QMC) method implemented with the ALPS package [95]. Our used QMC code was based on the directed-loop algorithm in the stochastic-series-expansion representation [96–98]. The Hamiltonian used in the QMC calculation is the decomposition of the exchange interaction J in Eq. (4-1-1) into three types of the exchange interactions J_A, J_B, and

J_C based on the crystal structure in Ref. 94 as shown in Fig. 4-2-7. The calculation was performed for the system size of 72 with periodic boundary condition. The details of the size dependence will be described in Appendix III. The size of 72 is enough to obtain the thermodynamic limit of physical quantity.

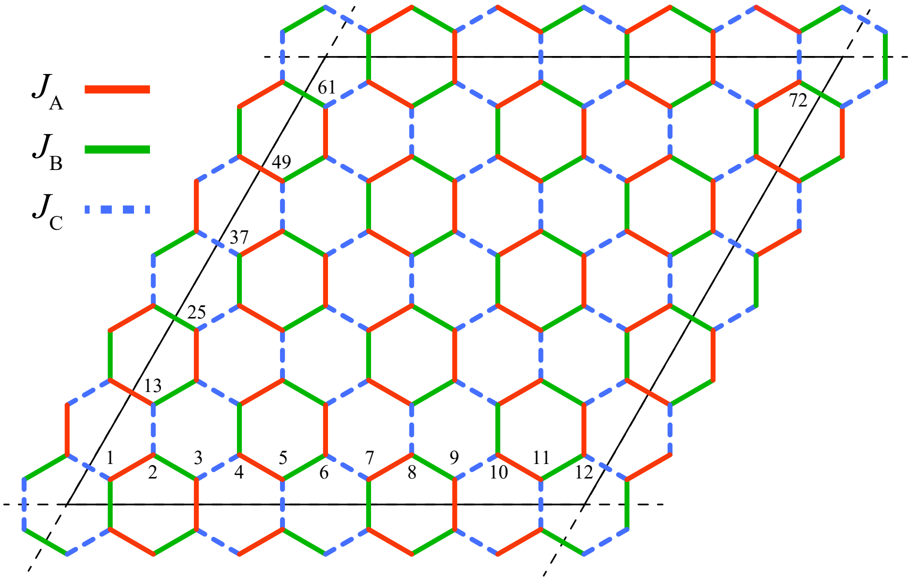

Figure 4-2-7: Schematic view of the honeycomb-lattice with three types of the nearest-neighbor interactions (J_A, J_B, and J_C) used in the QMC calculation. The numbers represent the site numbers.

4-2-4 Comparison with Numerical Results

First, we confirm the experimental outcome. The magnetic susceptibility, specific heat, and magnetization measurements suggest that the ground state must be a nonmagnetic singlet state with an excitation energy gap to the triplet state. The finite magnetization at low fields is thought to arise partly from the magnetic impurities, the contribution of which is also observed in the magnetic susceptibility in Fig. 4-2-2. However, the origin of the small finite slope of the magnetization curve below 20 T is not clear at present.

The structural analysis suggests three different exchange paths, but two of them must be almost equal because of the local environment around the Cu^{2+} ions and the bonding between Cu^{2+} ions. We, however, first calculated the magnetization curve for a regular HLA, in which the magnitudes of all the exchange interactions were identical (i.e., $J_A = J_B = J_C$), as shown by the darkest blue line with marker in Fig. 4-2-8. As the magnetic field increases, this magnetization curve increases continuously from zero with a concave curvature, which is a gapless feature and does not correspond to experimental observation.

In order to open the energy gap, different exchange interactions should be included in the calculation. Figure 4-2-8 displays the results of magnetization curves calculating for the exchange interaction ratio J_C/J_A from 0.0 to 1.0 in 0.1 increments when the normalized temperature T^* by J_A is 0.032. One-third and two-thirds magnetization plateaus are found to appear as J_C/J_A approached from 1.0 to 0.0. Based on the above description, the calculated magnetization curve reproduces the observed behavior when $J_A/k_B = 43.7$ K, $J_A = J_B$ and $J_C/J_A = 0.2$ as shown in Fig. 4-2-9. However, above the 2/3 magnetization plateau, the calculated magnetization differs completely from the observed one. The calculated curve increases toward the saturation value, while the observed one shows the behavior implying another magnetization plateau.

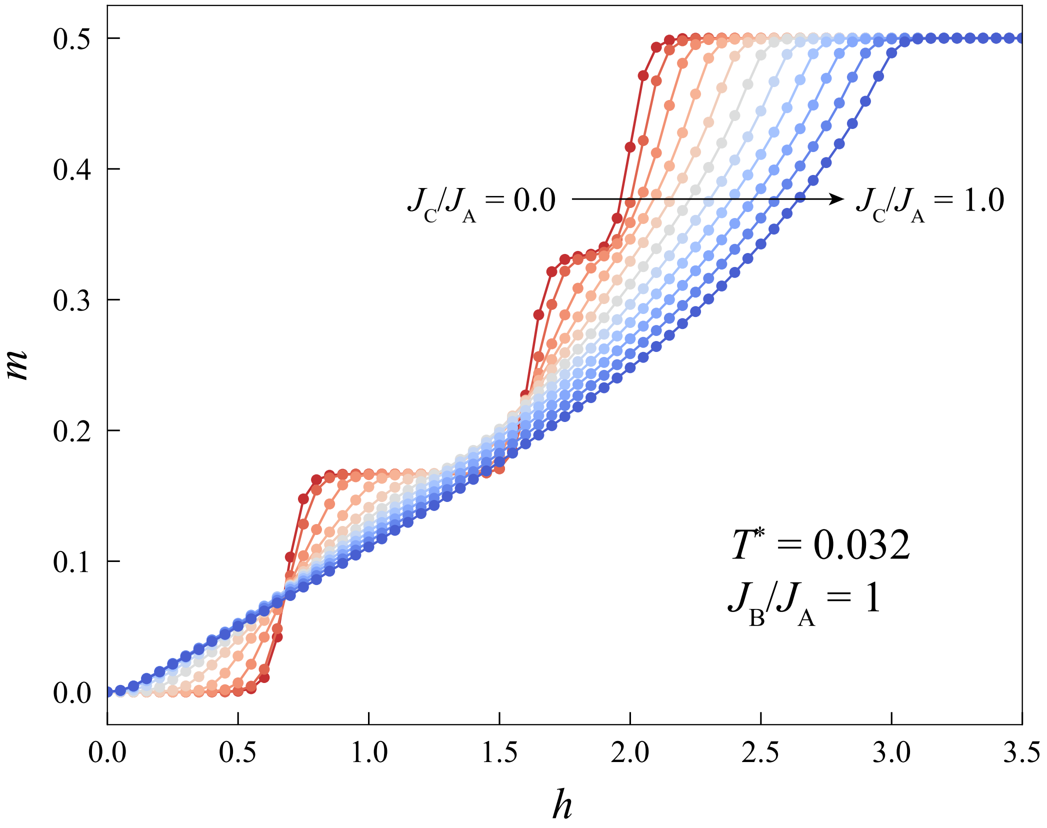

Figure 4-2-8: Numerically calculated magnetization curves at various ratio J_C/J_A from 0 to 1 every 0.1 step when $J_A = 1$ and $J_B/J_A = 1$. m is the magnetization per spin, h is the normalized magnetic field ($= g\mu_B H/J_A$), and T^* is the normalized temperature ($= k_B T/J_A$). The error bars of the magnetization are omitted for simplicity, since the width of the errors are less than the size of the markers.

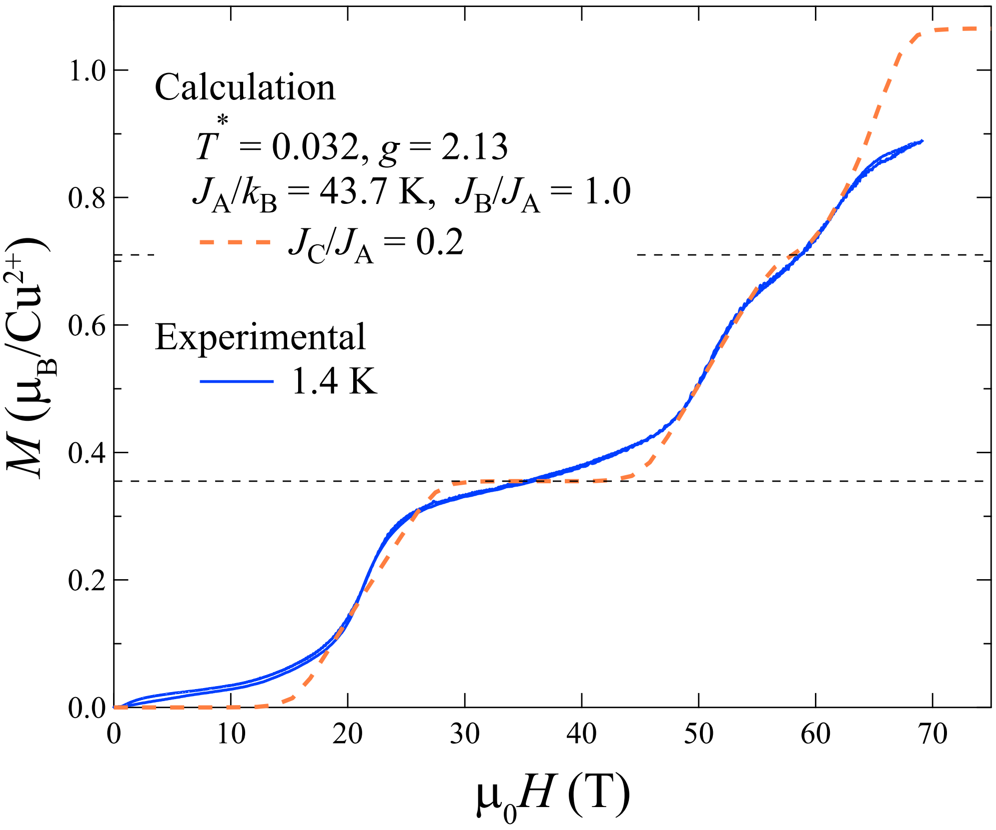

Figure 4-2-9: High-field magnetization curves for a polycrystalline $Cu_2(pymca)_3(ClO_4)$ sample at 1.4 K (solid line) and for a HLA calculated by QMC method for parameter sets of exchange constants ($J_A = J_B$, $J_C/J_A = 0.2$, $J_A/k_B = 43.7$ K) at $T^* = k_BT/J = 0.032$ with $g = 2.13$, as described in the text (orange dashed line).

4-3 Discussion

We next discuss how to change the magnetization plateaus based on the QMC calculations. Our measured magnetization curve of $Cu_2(pymca)_3(ClO_4)$ indicates one-third and two-thirds magnetization plateaus in the J_A-J_B-J_C HLA model. We therefore investigate the magnetization curves by changing the ratios of exchange bonds. Numerical calculation results, for a fixed ratio $J_C/J_A = 0.2$, are shown in Fig. 4-3-1. The field range of each magnetization plateau increases as J_B/J_A increases. The observed magnetization curve is reproduced most accurately when $J_C/J_A = 0.2$ and $J_B/J_A = 1.0$. This finding corresponds to the fact that two out of three Cu-Cu exchange bonds have a similar bond length, as stated in Sect. 4-1-2. The lengths of these two are only about 1% different from each other. However, the small difference may affect the overlap of electron orbitals of Cu^{2+} ions, resulting in a large change in the exchange interaction. The calculations reveal that one small and two large exchange bonds are required to observe the 1/3 and 2/3 magnetization plateaus in a distorted HLA. These calculations do not reproduce step-like features in the magnetization above the 2/3 magnetization plateau. In addition, the temperature dependence of the magnetic susceptibility calculated using the same parameters for the magnetization is shown in Fig. 4-3-2. Although the qualitative behavior of the calculated susceptibility agrees with the experimental

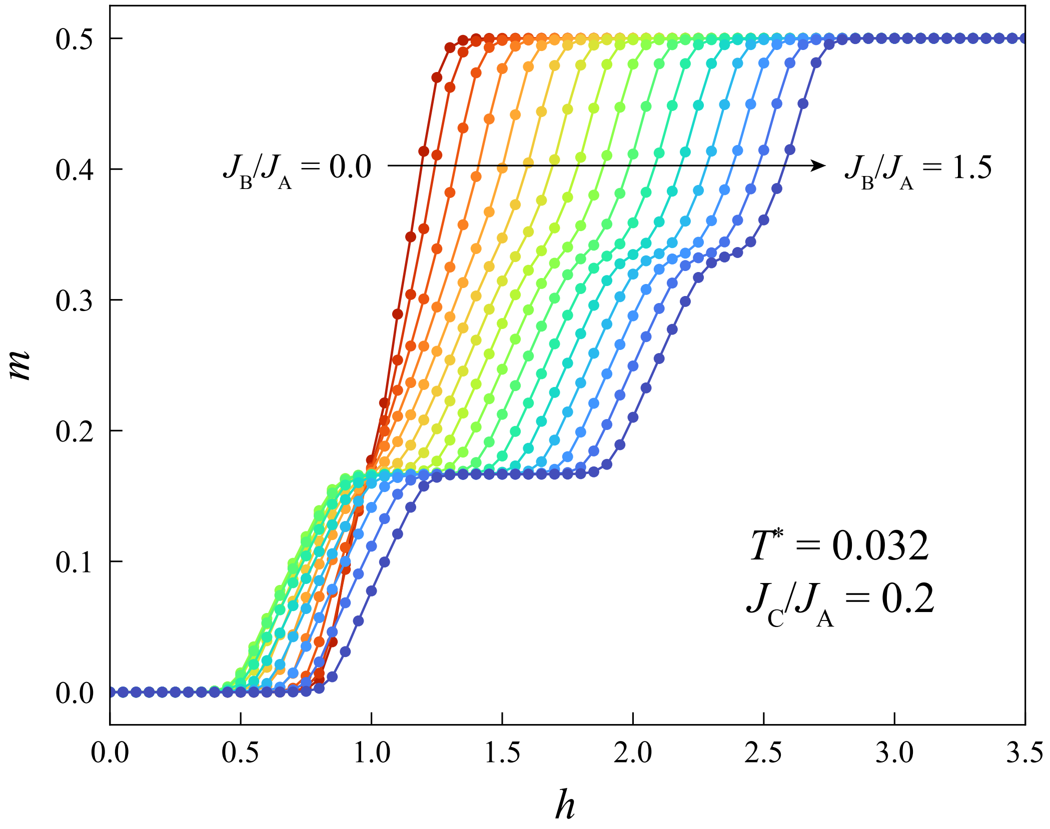

Figure 4-3-1: Numerically calculated magnetization curves at various ratio J_B/J_A from 0 to 1.5 every 0.1 step when $J_A = 1$ and $J_C/J_A = 0.2$. m, h, and T^* are defined as well in Fig. 4-2-8. The error bars of the magnetization are omitted for simplicity, as the same reason in the caption of Fig. 4-2-8.

one, there is a quantitative difference between them. Better parameters to reproduce the observed magnetic susceptibility are $g = 2.08$ and $J_C/J_A = 0.5$. However, the g-value determined by ESR measurements is 2.13 at any temperature, which disagrees with the above value (2.08). Thus, further theoretical and experimental studies on this compound may be necessary. Experiment in magnetic fields beyond 70 T would be required and a more sophisticated and suitable model needs to be considered for this compound.

Takano calculated the phase diagram of the $S = 1/2$ J_A-J_B-J_C model on the HLA at 0 K by a nonlinear σ model [99]. For the parameter window $\ln(J_A/J_C), \ln(J_B/J_C) \in [-3, 3]$, an AF LRO phase and a gapped spin liquid phase are separated as shown in Fig. 4-3-3. The AF phase is symmetric against the $J_A = J_B$ line. Our compound $Cu_2(pymca)_3(ClO_4)$ is located in the AF LRO phase ($J_A/J_C = J_B/J_C = 5$) in the calculation. Later, Shimokawa calculated numerically the phase diagram for the same model by a QMC method [100]. In the parameter window $J_A/J_C, J_B/J_C \in [0.1, 10]$, the calculated AF LRO phase is small compared with the calculated one by Takano. As a result, our compound is in the spin liquid phase as indicated in Fig. 4-3-4. This is consistent with our observation. The ground state is a singlet with an excitation gap. There are six types of singlet states in the spin liquid phase, as illustrated in Fig. 4-3-4. Three of them are different dimer states which appear in three regimes of ($J_A \gg J_B \sim J_C$), ($J_B \gg J_A \sim J_C$), and ($J_C \gg J_A \sim J_B$). The others are different singlet states consisting of singlet clusters of six spins which appear in three regimes between the dimer-state regimes. They can continuously vary to each other as changing the parameters in the singlet phase.

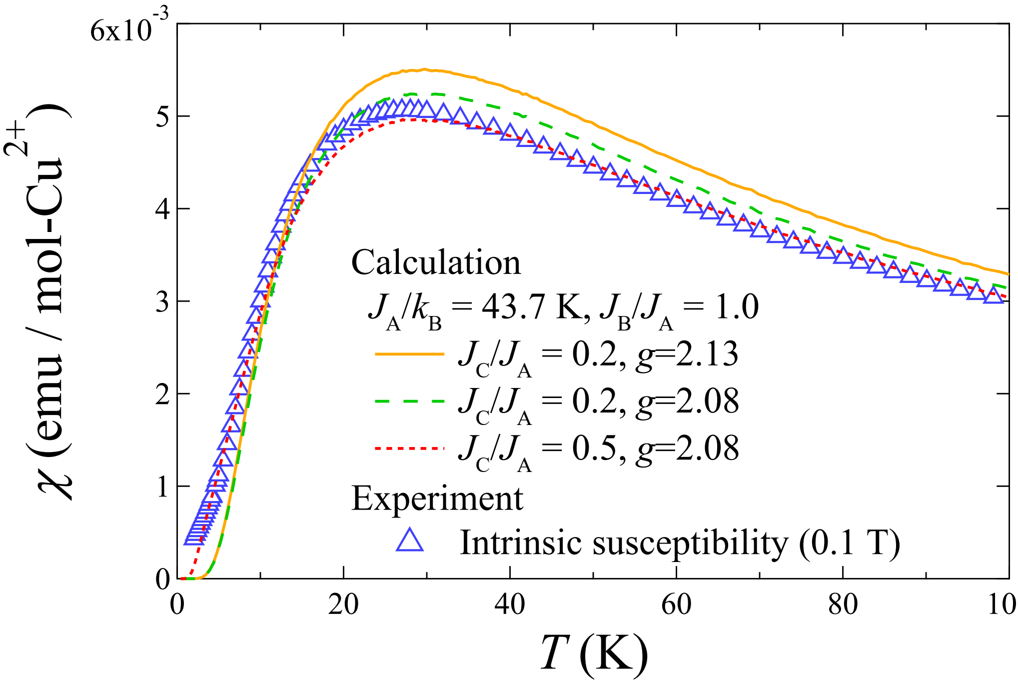

Figure 4-3-2: Temperature dependence of the intrinsic magnetic susceptibility and numerically calculated one for indicated different parameter sets.

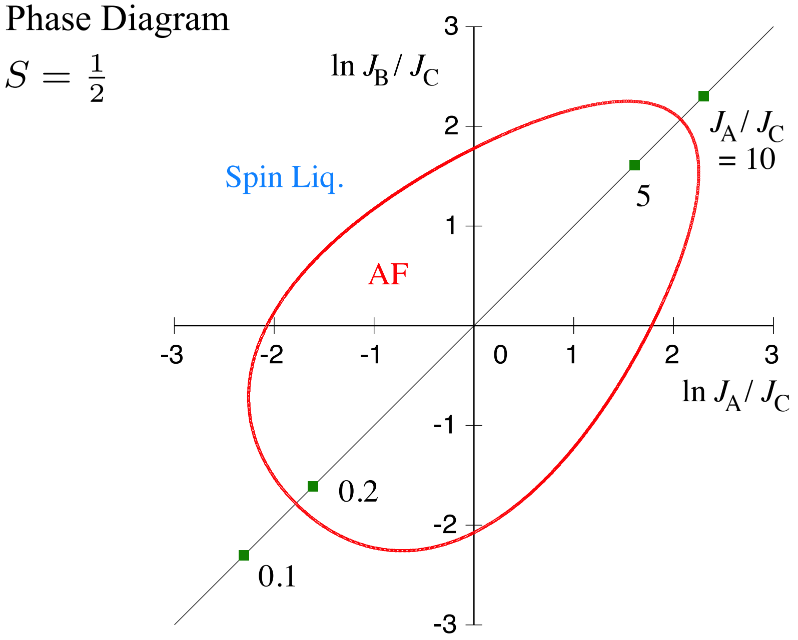

Figure 4-3-3: Phase diagram of the $S = 1/2$ J_A-J_B-J_C model on the HLA in the parameter window $\ln(J_A/J_C), \ln(J_B/J_C) \in [-3, 3]$ calculated by a nonlinear σ model. Quoted from [99].

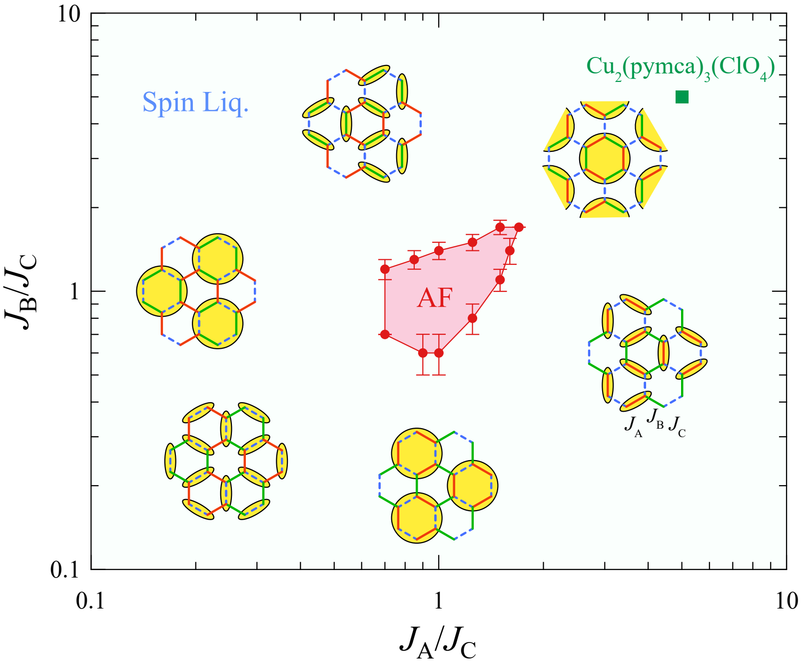

Figure 4-3-4: Phase diagram of the $S = 1/2$ J_A-J_B-J_C model on the HLA in the parameter window $J_A/J_C, J_B/J_C \in [0.1, 10]$ by a quantum Monte Carlo method [100]. The error bars indicate the calculation errors. The schematic views of the singlet states (yellow circles) in the honeycomb-lattice.

4-4 Conclusion

In conclusion, we performed magnetic susceptibility, specific heat, ESR, and magnetization measurements on polycrystalline $\mathrm{Cu_2(pymca)_3(ClO_4)}$ samples, regarded as a spin-1/2 HLA. The magnetic susceptibility showed a broad maximum near 25 K, characteristic of a low-dimensional antiferromagnet. The specific heat at zero field decreased smoothly down to 0.6 K, indicating no long-range magnetic order down to this temperature. Each ESR spectrum of the polycrystalline sample could be fitted to a single Lorentzian function. The high-field magnetization up to 70 T shows three step-like features that are notably reproduced, except for the magnetization near 70 T, by a QMC calculation using the exchange constants $J_{\mathrm{A}}/k_{\mathrm{B}} = 43.7$ K, $J_{\mathrm{A}} = J_{\mathrm{B}}$, and $J_{\mathrm{C}}/J_{\mathrm{A}} = 0.2$. We found that the distortion of the honeycomb-lattice, resulting in having two large and one small exchange interactions, causes this step-like magnetization. The parameters used for the calculation were found to be located in the spin liquid phase calculated by a QMC method, which agrees with the experimental observation.

5 Summary

We summarize our studies on two types of the spin-1/2 low-dimensional antiferromagnets $BaCo_2V_2O_8$ and $Cu_2(pymca)_3(ClO_4)$.

S= 1/2 quasi-one-dimensional antiferromagnet $BaCo_2V_2O_8$

- Single crystals $BaCo_2V_2O_8$ were grown by the floating-zone method.
- The field-induced order-disorder transition, observed by the specific heat measurements, occurs at approximately 10 T for $H \parallel [100]$.
- Electron spin resonance measurements were performed, and the lowest excitation mode with an energy gap of about 400 GHz in zero magnetic field exhibits softening at 10 T for $H \parallel [100]$, whereas, for $H \parallel [110]$, it does not up to the saturation field.
- Magnetic excitations were calculated by the density-matrix renormalization group method using the Hamiltonian, that reflects the crystal structure of $BaCo_2V_2O_8$, and the calculations reproduced the observed modes for $H \parallel [100]$ well and did not so much for $H \parallel [110]$.
- The transition magnetic field of 10 T for $H \parallel [100]$ was reproduced by the calculations for two cases, the staggered magnetic field parameter C_y change ($C_y = 0.25$ below 20 T and $C_y = 0.4$ above 20 T) and the finite interchain interaction J' ($0.02J$). Overall, the latter is appropriated.
- The disordered state above the critical magnetic field for $H \parallel [100]$ is considered to be a field-induced ferromagnetic state or a paramagnetic state, unlike a Tomonaga-Luttinger spin liquid state for $H \parallel [001]$.

S= 1/2 honeycomb-lattice antiferromagnet $Cu_2(pymca)_3(ClO_4)$

- Specific heat measurements in zero field revealed no long-range magnetic order down to 0.6 K.
- A paramagnetic signal with $g = 2.13$ and a single-Lorentzian shape was observed for a polycrystalline sample in the electron spin resonance measurements.
- The magnetization measurements were performed in magnetic fields of up to 70 T at 1.4 K, and the magnetization curve represented three step-like features.
- The calculated magnetization by the quantum Monte Carlo (QMC) method using the distorted honeycomb-lattice Hamiltonian with $J_A/k_B = 43.7$ K, $J_B/J_A = 1$, and $J_C/J_A = 0.2$ reproduced the observed magnetization curve, except for the magnetization near 70 T.
- The parameters used for the calculation were found to be located in the spin liquid phase (gapped) calculated by a QMC method.
- The observed magnetization near 70 T and magnetic susceptibility do not agree with those of the calculation, Therefore, further experiments and calculations including model improvements are required.

Appendix I

In this appendix, we consider from a theoretical point of view that a transverse magnetic field causes the phase transition in $\mathrm{BaCo_2V_2O_8}$. The Hamiltonian expressed in terms of fermion operators, obtained through the Jordan-Wigner transformation, is useful for gaining insight into elementary spinon excitations. Here, we analyze the effective spin model for $\mathrm{BaCo_2V_2O_8}$ in transverse fields by using the Jordan-Wigner transformation. For simplicity, we ignore the z-component of the effective staggered fields, namely the h_z term in Eq. (3-2-2), because our numerical results indicate that the critical field is relatively insensitive to h_z when compared with the significant effect of h_y. We do not include the interchain interaction $\mathcal{H}^{\mathrm{MF}}_{\mathrm{inter}}$ in the present argument. J is set equal to unity. Thus, we consider the Hamiltonian given by

$$\begin{aligned}\mathcal{H} =& \sum_j \left\{ S^z_j S^z_{j+1} + \varepsilon \left(S^x_j S^x_{j+1} + S^y_j S^y_{j+1} \right) \right\} \\ &- \mu_{\mathrm{B}} \sum_j \left\{ g_{xx} H_0 S^x_j + h_y S^y_j \sin\left[2\phi + \pi(j-1)\right] \right\}. \end{aligned} \tag{A1-1}$$

To apply the Jordan-Wigner transformation, we rotate the spin coordination so as to align the field direction with the z-axis [17,84]. For $H \parallel [100]$ ($\phi = \pi/4$), the h_y term is of $+-+-$ type. Accordingly, the spin coordination is rotated in the following order: (1) $R_x(\pi)$ on even sites, (2) $R_{z'}(\theta)$ on all sites with $\theta = \tan^{-1}(g_{xx}H_0/h_y) = \tan^{-1}(1/C_y)$, and (3) $R_{x''}(\pi/2)$ on all sites, where $R_\alpha(\psi)$ performs the rotation by an angle ψ around the α axis. Using these rotations, Eq. (A1-1) is transformed into

$$\mathcal{H}_{100} = \sum_j \vec{S}_j M_{100} \vec{S}_{j+1} - A_{100} x \sum_j S^z_j, \tag{A1-2}$$

$$M_{100} = \begin{pmatrix} \varepsilon\cos 2\theta & 0 & \varepsilon \sin 2\theta \\ 0 & -1 & 0 \\ \varepsilon \sin 2\theta & 0 & -\varepsilon\cos 2\theta \end{pmatrix}, \tag{A1-3}$$

where $A_{100} \equiv g_{xx}(\sin\theta + C_y\cos\theta) = g_{xx}\sqrt{1+C_y^2}$ denotes an effective g-factor, estimated to be 2.96 with $g_{xx} = 2.75$ and $C_y = 0.4$, and $x \equiv \mu_B H_0$. The spin operators are written in the post-rotated frame.

In the Jordan-Winger transformation, the spin operators $\vec{S}_j$ are represented by spinless fermion (spinon) operators $f^\dagger_j$ (f_j) as

$$S^+_j = (S^-_j)^\dagger = \exp\left(\mathrm{i}\pi \sum_{i=1}^{j-1} f^\dagger_i f_i \right) f^\dagger_j, \tag{A1-4}$$

$$S^z_j = f^\dagger_j f_j - \frac{1}{2}. \tag{A1-5}$$

We focus on the one-body Hamiltonian to obtain an intuitive picture of the elementary excitation. Thus, we eliminate the $S^x_j S^z_{j+1}$, $S^z_j S^x_{j+1}$, and $S^z_j S^z_{j+1}$ terms. Equation (A1-2) is transcribed into a fermionic representation as

$$\begin{aligned}\mathcal{H}_{100} =& \sum_j \left[\frac{T_-(\theta)}{2} \left(f^\dagger_j f_{j+1} + f^\dagger_{j+1} f_j \right) \right. \\ & \left. + \frac{T_+(\theta)}{2} \left(f^\dagger_j f^\dagger_{j+1} + f_{j+1} f_j \right) - A_{100} x f^\dagger_j f_j \right], \end{aligned} \tag{A1-6}$$

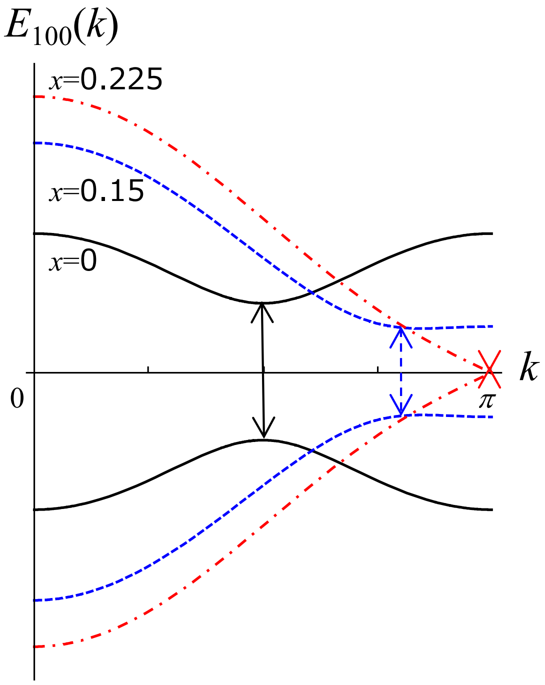

Figure A1-1: The spinon bands given by Eq. (A1-8) are plotted for $x = 0$ (black solid line), 0.15 (blue broken line), and 0.225 (red dotted broken line). The arrows indicate the spinon particle-hole excitations, which are associated with the lowest excitation observed by ESR. The arrow length indicates the magnitude of the excitation energy, which decreases with increasing magnetic field, i.e., x. Quoted from [101].

where $T_{\pm}(\theta) \equiv \frac{1}{2}(\varepsilon \cos 2\theta \pm 1)$. In momentum space, Eq. (A1-6) is transformed into

$$\mathcal{H}_{100} = \frac{1}{2} \sum_k \Psi_k^\dagger \begin{pmatrix} \eta_k & \mathrm{i}T_+(\theta) \sin k \\ -\mathrm{i}T_+(\theta) \sin k & -\eta_k \end{pmatrix} \Psi_k, \tag{A1-7}$$

where $\Psi_k^\dagger \equiv \left(f_k^\dagger, f_{-k}\right)$, and $\eta_k \equiv T_-(\theta) \cos k - A_{100} x$.

Diagonalizing the 2×2 matrix in Eq. (A1-7) yields the spinon band

$$E_{100}(k) = \pm\sqrt{\eta_k^2 + [T_+(\theta) \sin k]^2}. \tag{A1-8}$$

As shown in Fig. A1-1, the spinon band is composed of particle and hole bands, while they are mixed and a band gap appears. The lower band is fully occupied in the ground state. An elementary excitation is associated with particle-hole excitations from the "valence" band to the "conduction" band. We note that, as indicated by the arrows in Fig. A1-1, the top of the valence band and the bottom of the conduction band have the same momentum, so that the lowest excitation has zero momentum. With increasing transverse field, the particle and hole band energies shift in opposite directions, and eventually split above a critical field. According to this band shift, the excitation gap shrinks, closes at the critical point, and subsequently increases. The excitation gap corresponds to a spinon gap below the critical field. The descending mode observed in the ESR measurements, shown in Fig. 3-2-15, can be associated with the lowest particle-hole excitation of a spinon. Thus, the elementary excitation is described within a spinon picture, despite the presence of the effective staggered field .

We next discuss the dependence of the critical field. We note that the momentum position of the band gap is $k = \pi/2$ in zero field and moves to $k = \pi$ with increasing transverse field. Therefore, the critical field is determined by $E_{100}(\pi) = 0$ as

$$x_{c(100)} = \frac{1}{2A_{100}}(1 - \varepsilon \cos 2\theta). \tag{A1-9}$$

A_{100} simply specifies a scale factor, while the critical field depends on ε and C_y through a factor $(1-\varepsilon \cos 2\theta)$ with $\theta = \tan^{-1}(1/C_y)$. With increasing C_y, θ varies monotonically from $\pi/2$ to 0, such that $(1-\varepsilon \cos 2\theta)$ changes from $(1+\varepsilon)$ to $(1-\varepsilon)$. This suggests that the critical field should decrease because of the effective staggered field if ε is finite. The relevance of ε and C_y is consistent with the intuitive interpretation, discussed in Sect. 3-3, that the longitudinal antiferromagnetic order is quickly suppressed owing to the combined effects of the transverse field and transverse exchange interaction.

For the case of $H \parallel [110]$ ($\phi = 0$), the same procedure can be followed with only slight modifications. Because the h_y term disappears for $\phi = 0$, the rotation $R_x(\pi)$ on even sites (which was the first process for $H \parallel [100]$) is unnecessary, and $C_y = 0$. The critical field is given by setting $C_y = 0$ in Eq. (A1-9). Consequently, the difference between $H \parallel [100]$ and $H \parallel [110]$ is attributed to the presence of C_y.

Appendix II

In this appendix, the program used for the calculation of the magnetization process for $Cu_2(pymca)_3(ClO_4)$ by quantum Monte Carlo (QMC) method implemented with the ALPS package is shown. ALPS has several lattices and Hamiltonians prepared in advance, but users can also define their own lattice and Hamiltonian. In this program, the calculation was performed through python using uniquely defined lattice and Hamiltonian.

The first program list defines the honeycomb-lattice with three types of nearest-neighbor interactions. The number of spins is 72. In the List A2-1, the lines in XML file represent "VERTEX" and "EDGE" elements that correspond to the site and the bond, respectively. Each tag <...> in the XML file consists of <element, attribute, attribute,...>. Each element provides the attribute ("type") that indicates the type used when constructing the Hamiltonian. When the two "id" attributes in the <VERTEX> are assigned to the attributes "source" and "target" in the <EDGE>, the bond between two sites can be defined.

List A2-1: JAJBJC-honeycomb-lattices.xml

```
<LATTICES>

<GRAPH name="honeycomb lattice 6x6" dimension="2" vertices="72" edges
   ="108">
  <VERTEX id=" 1" type=" 1"/>
  <VERTEX id=" 2" type=" 2"/>
  <VERTEX id=" 3" type=" 1"/>
  <VERTEX id=" 4" type=" 2"/>
  <VERTEX id=" 5" type=" 1"/>
  <VERTEX id=" 6" type=" 2"/>
  <VERTEX id=" 7" type=" 1"/>
  <VERTEX id=" 8" type=" 2"/>
  <VERTEX id=" 9" type=" 1"/>
  <VERTEX id=" 10" type=" 2"/>
  <VERTEX id=" 11" type=" 1"/>
  <VERTEX id=" 12" type=" 2"/>
  <VERTEX id=" 13" type=" 1"/>
  <VERTEX id=" 14" type=" 2"/>
  <VERTEX id=" 15" type=" 1"/>
  <VERTEX id=" 16" type=" 2"/>
  <VERTEX id=" 17" type=" 1"/>
  <VERTEX id=" 18" type=" 2"/>
  <VERTEX id=" 19" type=" 1"/>
  <VERTEX id=" 20" type=" 2"/>
  <VERTEX id=" 21" type=" 1"/>
  <VERTEX id=" 22" type=" 2"/>
  <VERTEX id=" 23" type=" 1"/>
  <VERTEX id=" 24" type=" 2"/>
  <VERTEX id=" 25" type=" 1"/>
  <VERTEX id=" 26" type=" 2"/>
  <VERTEX id=" 27" type=" 1"/>
  <VERTEX id=" 28" type=" 2"/>
  <VERTEX id=" 29" type=" 1"/>
  <VERTEX id=" 30" type=" 2"/>
  <VERTEX id=" 31" type=" 1"/>
  <VERTEX id=" 32" type=" 2"/>
```

```
<VERTEX id=" 33" type=" 1"/>
<VERTEX id=" 34" type=" 2"/>
<VERTEX id=" 35" type=" 1"/>
<VERTEX id=" 36" type=" 2"/>
<VERTEX id=" 37" type=" 1"/>
<VERTEX id=" 38" type=" 2"/>
<VERTEX id=" 39" type=" 1"/>
<VERTEX id=" 40" type=" 2"/>
<VERTEX id=" 41" type=" 1"/>
<VERTEX id=" 42" type=" 2"/>
<VERTEX id=" 43" type=" 1"/>
<VERTEX id=" 44" type=" 2"/>
<VERTEX id=" 45" type=" 1"/>
<VERTEX id=" 46" type=" 2"/>
<VERTEX id=" 47" type=" 1"/>
<VERTEX id=" 48" type=" 2"/>
<VERTEX id=" 49" type=" 1"/>
<VERTEX id=" 50" type=" 2"/>
<VERTEX id=" 51" type=" 1"/>
<VERTEX id=" 52" type=" 2"/>
<VERTEX id=" 53" type=" 1"/>
<VERTEX id=" 54" type=" 2"/>
<VERTEX id=" 55" type=" 1"/>
<VERTEX id=" 56" type=" 2"/>
<VERTEX id=" 57" type=" 1"/>
<VERTEX id=" 58" type=" 2"/>
<VERTEX id=" 59" type=" 1"/>
<VERTEX id=" 60" type=" 2"/>
<VERTEX id=" 61" type=" 1"/>
<VERTEX id=" 62" type=" 2"/>
<VERTEX id=" 63" type=" 1"/>
<VERTEX id=" 64" type=" 2"/>
<VERTEX id=" 65" type=" 1"/>
<VERTEX id=" 66" type=" 2"/>
<VERTEX id=" 67" type=" 1"/>
<VERTEX id=" 68" type=" 2"/>
<VERTEX id=" 69" type=" 1"/>
<VERTEX id=" 70" type=" 2"/>
<VERTEX id=" 71" type=" 1"/>
<VERTEX id=" 72" type=" 2"/>
<EDGE source=" 1" target=" 2" type="1"/>
<EDGE source=" 2" target=" 3" type="2"/>
<EDGE source=" 3" target=" 4" type="3"/>
<EDGE source=" 4" target=" 5" type="1"/>
<EDGE source=" 5" target=" 6" type="2"/>
<EDGE source=" 6" target=" 7" type="3"/>
<EDGE source=" 7" target=" 8" type="1"/>
<EDGE source=" 8" target=" 9" type="2"/>
<EDGE source=" 9" target=" 10" type="3"/>
<EDGE source=" 10" target=" 11" type="1"/>
<EDGE source=" 11" target=" 12" type="2"/>
<EDGE source=" 12" target=" 1" type="3"/>
<EDGE source=" 13" target=" 14" type="2"/>
<EDGE source=" 14" target=" 15" type="3"/>
<EDGE source=" 15" target=" 16" type="1"/>
<EDGE source=" 16" target=" 17" type="2"/>
<EDGE source=" 17" target=" 18" type="3"/>
```

```
<EDGE source=" 18" target=" 19" type="1"/>
<EDGE source=" 19" target=" 20" type="2"/>
<EDGE source=" 20" target=" 21" type="3"/>
<EDGE source=" 21" target=" 22" type="1"/>
<EDGE source=" 22" target=" 23" type="2"/>
<EDGE source=" 23" target=" 24" type="3"/>
<EDGE source=" 24" target=" 13" type="1"/>
<EDGE source=" 25" target=" 26" type="3"/>
<EDGE source=" 26" target=" 27" type="1"/>
<EDGE source=" 27" target=" 28" type="2"/>
<EDGE source=" 28" target=" 29" type="3"/>
<EDGE source=" 29" target=" 30" type="1"/>
<EDGE source=" 30" target=" 31" type="2"/>
<EDGE source=" 31" target=" 32" type="3"/>
<EDGE source=" 32" target=" 33" type="1"/>
<EDGE source=" 33" target=" 34" type="2"/>
<EDGE source=" 34" target=" 35" type="3"/>
<EDGE source=" 35" target=" 36" type="1"/>
<EDGE source=" 36" target=" 25" type="2"/>
<EDGE source=" 37" target=" 38" type="1"/>
<EDGE source=" 38" target=" 39" type="2"/>
<EDGE source=" 39" target=" 40" type="3"/>
<EDGE source=" 40" target=" 41" type="1"/>
<EDGE source=" 41" target=" 42" type="2"/>
<EDGE source=" 42" target=" 43" type="3"/>
<EDGE source=" 43" target=" 44" type="1"/>
<EDGE source=" 44" target=" 45" type="2"/>
<EDGE source=" 45" target=" 46" type="3"/>
<EDGE source=" 46" target=" 47" type="1"/>
<EDGE source=" 47" target=" 48" type="2"/>
<EDGE source=" 48" target=" 37" type="3"/>
<EDGE source=" 49" target=" 50" type="2"/>
<EDGE source=" 50" target=" 51" type="3"/>
<EDGE source=" 51" target=" 52" type="1"/>
<EDGE source=" 52" target=" 53" type="2"/>
<EDGE source=" 53" target=" 54" type="3"/>
<EDGE source=" 54" target=" 55" type="1"/>
<EDGE source=" 55" target=" 56" type="2"/>
<EDGE source=" 56" target=" 57" type="3"/>
<EDGE source=" 57" target=" 58" type="1"/>
<EDGE source=" 58" target=" 59" type="2"/>
<EDGE source=" 59" target=" 60" type="3"/>
<EDGE source=" 60" target=" 49" type="1"/>
<EDGE source=" 61" target=" 62" type="3"/>
<EDGE source=" 62" target=" 63" type="1"/>
<EDGE source=" 63" target=" 64" type="2"/>
<EDGE source=" 64" target=" 65" type="3"/>
<EDGE source=" 65" target=" 66" type="1"/>
<EDGE source=" 66" target=" 67" type="2"/>
<EDGE source=" 67" target=" 68" type="3"/>
<EDGE source=" 68" target=" 69" type="1"/>
<EDGE source=" 69" target=" 70" type="2"/>
<EDGE source=" 70" target=" 71" type="3"/>
<EDGE source=" 71" target=" 72" type="1"/>
<EDGE source=" 72" target=" 61" type="2"/>
<EDGE source=" 2" target=" 13" type="3"/>
<EDGE source=" 4" target=" 15" type="2"/>
```

```
  <EDGE source=" 6" target=" 17" type="1"/>
  <EDGE source=" 8" target=" 19" type="3"/>
  <EDGE source=" 10" target=" 21" type="2"/>
  <EDGE source=" 12" target=" 23" type="1"/>
  <EDGE source=" 14" target=" 25" type="1"/>
  <EDGE source=" 16" target=" 27" type="3"/>
  <EDGE source=" 18" target=" 29" type="2"/>
  <EDGE source=" 20" target=" 31" type="1"/>
  <EDGE source=" 22" target=" 33" type="3"/>
  <EDGE source=" 24" target=" 35" type="2"/>
  <EDGE source=" 26" target=" 37" type="2"/>
  <EDGE source=" 28" target=" 39" type="1"/>
  <EDGE source=" 30" target=" 41" type="3"/>
  <EDGE source=" 32" target=" 43" type="2"/>
  <EDGE source=" 34" target=" 45" type="1"/>
  <EDGE source=" 36" target=" 47" type="3"/>
  <EDGE source=" 38" target=" 49" type="3"/>
  <EDGE source=" 40" target=" 51" type="2"/>
  <EDGE source=" 42" target=" 53" type="1"/>
  <EDGE source=" 44" target=" 55" type="3"/>
  <EDGE source=" 46" target=" 57" type="2"/>
  <EDGE source=" 48" target=" 59" type="1"/>
  <EDGE source=" 50" target=" 61" type="1"/>
  <EDGE source=" 52" target=" 63" type="3"/>
  <EDGE source=" 54" target=" 65" type="2"/>
  <EDGE source=" 56" target=" 67" type="1"/>
  <EDGE source=" 58" target=" 69" type="3"/>
  <EDGE source=" 60" target=" 71" type="2"/>
  <EDGE source=" 62" target=" 1" type="2"/>
  <EDGE source=" 64" target=" 3" type="1"/>
  <EDGE source=" 66" target=" 5" type="3"/>
  <EDGE source=" 68" target=" 7" type="2"/>
  <EDGE source=" 70" target=" 9" type="1"/>
  <EDGE source=" 72" target=" 11" type="3"/>
</GRAPH>

</LATTICES>
```

The following List A2-2 defines the spin Hamiltonian. The lines until <BONDOPERATOR> in the list are extracted from the source file of ALPS program. From the line <HAMILTONIAN>, the parameters J_{A}, J_{B}, J_{C}, and h are defined in the <PARAMETER> lines. The <SITETERM> and <BONDTERM> lines define the Zeeman and the exchange interaction terms in the Hamiltonian. By assigning the "type" attributes in the <SITETERM> and <BONDTERM>, the sites and bonds with the same "type" attributes in the <VERTEX> and the <EDGE> elements are used for the calculation.

List A2-2: JAJBJC-honeycomb-model.xml

```
<MODELS>

<SITEBASIS name="spin">
  <PARAMETER name="local_spin" default="local_S"/>
  <PARAMETER name="local_S" default="1/2"/>
  <QUANTUMNUMBER name="S" min="local_spin" max="local_spin"/>
  <QUANTUMNUMBER name="Sz" min="-S" max="S"/>
```

```
  <OPERATOR name="Splus" matrixelement="sqrt(S*(S+1)-Sz*(Sz+1))">
    <CHANGE quantumnumber="Sz" change="1"/>
  </OPERATOR>
  <OPERATOR name="Sminus" matrixelement="sqrt(S*(S+1)-Sz*(Sz-1))">
    <CHANGE quantumnumber="Sz" change="-1"/>
  </OPERATOR>
  <OPERATOR name="Sz" matrixelement="Sz"/>
</SITEBASIS>

<BASIS name="spin">
  <SITEBASIS ref="spin"/>
  <CONSTRAINT quantumnumber="Sz" value="Sz_total"/>
</BASIS>

<BONDOPERATOR name="exchange" source="x" target="y">
  Sz(x)*Sz(y) + 1/2*( Splus(x)*Sminus(y) + Sminus(x)*Splus(y) )
</BONDOPERATOR>

<HAMILTONIAN name="spin">
  <PARAMETER name="JA" default="0"/>
  <PARAMETER name="JB" default="0"/>
  <PARAMETER name="JC" default="0"/>
  <PARAMETER name="h" default="0"/>
  <BASIS ref="spin"/>
  <SITETERM type="1" site="i">
    -h*Sz(i)
  </SITETERM>
  <SITETERM type="2" site="i">
    -h*Sz(i)
  </SITETERM>
  <BONDTERM type="1" source="i" target="j">
    JA*exchange(i,j)
  </BONDTERM>
  <BONDTERM type="2" source="i" target="j">
    JB*exchange(i,j)
  </BONDTERM>
  <BONDTERM type="3" source="i" target="j">
    JC*exchange(i,j)
  </BONDTERM>
</HAMILTONIAN>

</MODELS>
```

After loading the XML files of the lattice and the model, a series of parameter set (spin quantum number, temperature, Monte Carlo steps, J_{A}, J_{B}, J_{C}, and magnetic field h) is produced. This parameter set is used for QMC calculation given in the List A2-3 (python file). From the calculated results, the magnetization data are extracted and stored after changing text format. The magnetic susceptibility can be calculated in the same way.

List A2-3: mag_Honeycomb.py

```
import pyalps

JBname = 1.0
JCname = 0.2

```

```python
parms = []
for hloop in range(0,71):
    h = hloop*0.05
    parms.append({
        'LATTICE_LIBRARY': "JAJBJC-honeycomb-lattices.xml",
        'LATTICE' : "honeycomb lattice 6x6",
        'MODEL_LIBRARY' : "JAJBJC-honeycomb-model.xml",
        'MODEL' : "spin",
        'local_S' : 0.5,
        'T' : 0.032,
        'THERMALIZATION' : 100000,
        'SWEEPS' : 200000,
        'JA' : 1.0,
        'JB' : JBname,
        'JC' : JCname,
        'h' : h,
    })

input_file = pyalps.writeInputFiles('mag_JB='+str(JBname)+'_JC='+str(JCname),parms)
pyalps.runApplication('dirloop_sse',input_file,Tmin=30,MPI=4)

data = pyalps.loadMeasurements(pyalps.getResultFiles(prefix='mag_JB='+str(JBname)+'_JC='+str(JCname)),'Magnetization Density')
magnetization = pyalps.collectXY(data,x='h',y='Magnetization Density')

f = open('mag_JB='+str(JBname)+'_JC='+str(JCname)+'.dat','w')
f.write(pyalps.plot.convertToText(magnetization))
f.close()
```

Appendix III

In this appendix, the size dependence on the quantum Monte Carlo calculation of the magnetization process for $Cu_2(pymca)_3(ClO_4)$ is described.

Figure A3-1 shows the results of calculated magnetization curves for the exchange interaction ratio J_C/J_A from 0.0 to 1.0 in 0.1 increment at the normalized temperature $T^* = 0.032$ for 18 spin with periodic boundary condition. Compared with Fig. 4-2-8, the magnetization is nearly identical when J_C/J_A is small, but pseudo plateaus appear as J_C/J_A approaches to 1.0.

The calculated magnetization curves of a regular honeycomb-lattice ($J_A = J_B = J_C = 1$) for the system sizes of 18, 72, and 162 are represented in Fig. A3-2. Looking at this figure, the system size of 18 are significantly different from the others (72 and 162 sizes), which are almost the same. Therefore, various calculations in Sect. 4 were performed with 72 spins.

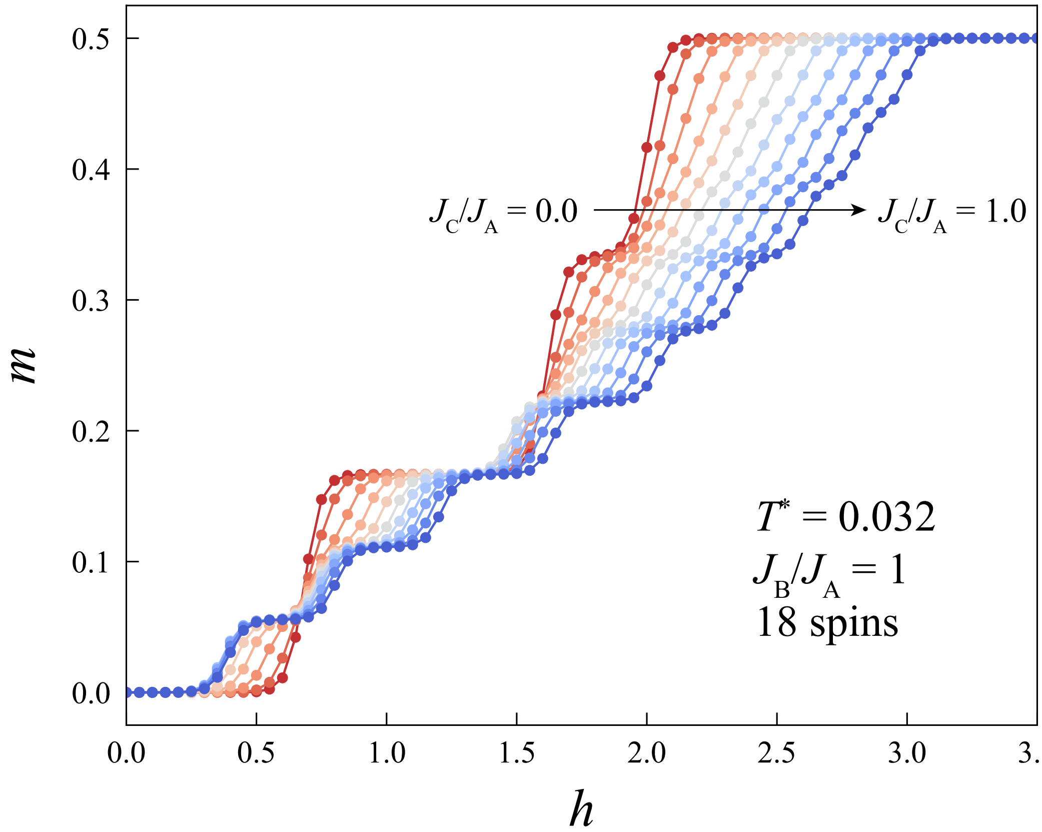

Figure A3-1: Numerically calculated magnetization curves at various ratio J_C/J_A from 0 to 1 every 0.1 step when $J_A = 1$ and $J_B/J_A = 1$. m, h, and T^* are defined as well in Fig. 4-2-8. The error bars of the magnetization are omitted for simplicity, as the same reason in the caption of Fig. 4-2-8.

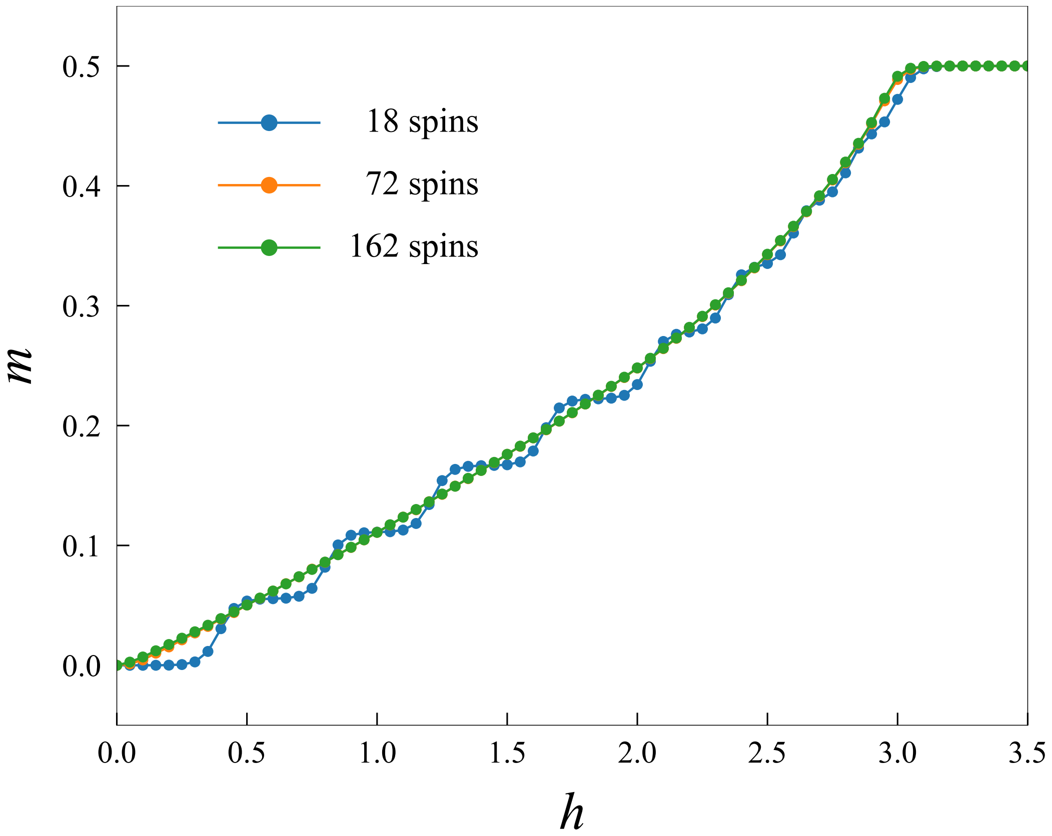

Figure A3-2: Numerically calculated magnetization curves for various system sizes (18, 72, and 162) at $J_{\mathrm{A}} = J_{\mathrm{B}} = J_{\mathrm{C}} = 1$. m, h, and T^{*} are defined as well in Fig. 4-2-8. The error bars of the magnetization are omitted for simplicity, as the same reason in the caption of Fig. 4-2-8.

References

[1] S. Sachdev, *Quantum Phase Transitions Second Edition* (Cambridge University Press, Cambridge, UK, 2011).

[2] A. Luther and I. Peschel, Phys. Rev. B **12**, 3908 (1975).

[3] F.D.M. Haldane, Phys. Rev. Lett. **45**, 1358 (1980).

[4] J.D. Cloizeaux and J.J. Pearson, Phys. Rev. **128**, 2131 (1962).

[5] P.W. Anderson, Phys. Rev. **86**, 694 (1952).

[6] R. Kubo, Phys. Rev. **86**, 929 (1952).

[7] R. Kubo, Rev. Mod. Phys. **25**, 344 (1953).

[8] Y. Endoh, G. Shirane, R.J. Birgeneau, P.M. Richards and S.L. Holt, Phys. Rev. Lett. **32**, 170 (1974).

[9] E. Lieb, T. Schultz, and D. Mattis, Ann. Phys. **16**, 407 (1961).

[10] S. Katsura, Phys. Rev. **127**, 1508 (1962).

[11] A. Dutta, G. Aeppli, B.K. Chakrabarti, U. Divakaran, T.F. Rosenbaum, and D. Sen, *Quantum Phase Transition in Transverse Field Spin Models From Statistical Physics to Quantum Information* (Cambridge University Press, Cambridge, UK, 2015).

[12] T. Kadowaki and H. Nishimori, Phys. Rev. E, **58**, 5355 (1998).

[13] R. Coldea, D.A. Tennant, E.M. Wheeler, E. Wawrzynska, D. Prabhakaran, M. Telling, K. Habicht, P. Smeibidl, and K. Kiefer, Science **327**, 177 (2010).

[14] C.N. Yang and C.P. Yang, Phys. Rev. **151**, 258 (1966).

[15] N.M. Bogoliubov, A.G. Izergin, and V.E. Korepin, Nucl. Phys. B **275**, 687 (1986).

[16] K. Okunishi and T. Suzuki, Phys. Rev. B **76**, 224411 (2007).

[17] P. Pfeuty, Ann. Phys. **57**, 79 (1970).

[18] D.V. Dmitriev, V.Y. Krivnov, and A.A. Ovchinnikov, Phys. Rev. B **65**, 172409 (2002).

[19] H. Shiba, Prog. Theor. Phys. **64**, 466 (1980).

[20] W.P. Lehmann, W. Breitling, and R. Weber, J. Phys. C: Solid State Phys. **14**, 4655 (1981).

[21] S.E. Nagler, W.J.L. Buyers, R.L. Armstrong, and B. Briat, Phys. Rev. B **27**, 1784 (1983).

[22] K. Amaya, H. Hori, I. Shiozaki, M. Date, M. Ishizuka, T. Sakakibara, T. Goto, N. Miura, H. Kikuchi, and Y. Ajiro, J. Phys. Soc. Jpn. **59**, 1810 (1990).

[23] H. Shiba, Y. Ueda, K. Okunishi, S. Kimura, and K. Kindo, J. Phys. Soc. Jpn. **72**, 2326 (2003).

[24] S. Mori, I. Mannari, and I. Harada, J. Phys. Soc. Jpn. **63**, 3474 (1994).

[25] R. Wichmann and Hk. Müller-Buschbaum, Z. Anorg. Allg. Chem. **534**, 153 (1986).

[26] D. Osterloh and Hk. Müller-Buschbaum, Z. Naturforsch. B **49b**, 923 (1994).

[27] Z. He, T. Taniyama, T. Kyomen, and M. Itoh, Phys. Rev. B **72**, 172403 (2005).

[28] Z. He, T. Taniyama, and M. Itoh, Appl. Phys. Lett. **88**, 132504 (2006).

[29] Z. He, T. Taniyama, and M. Itoh, Phys. Rev. B **73**, 212406 (2006).

[30] S. Kimura, H. Yashiro, M. Hagiwara, K. Okunishi, K. Kindo, Z. He, T. Taniyama, and M. Itoh, J. Phys.: Conf. Ser. **51**, 99 (2006).

[31] A. Okutani, T. Kida, T. Usui, T. Kimura, K. Okunishi, and M. Hagiwara, Phys. Procedia **75**, 779 (2015).

[32] B. Grenier, S. Petit, V. Simonet, E. Canévet, L.-P. Regnault, S. Raymond, B. Canals, C. Berthier, and P. Lejay, Phys. Rev. Lett. **114**, 017201 (2015).

[33] Z. Wang, M. Schmidt, A.K. Bera, A.T.M.N. Islam, B. Lake, A. Loidl, and J. Deisenhofer, Phys. Rev. B **91**, 140404(R) (2015).

[34] A.K. Bera, B. Lake, F.H.L. Essler, L. Vanderstraeten, C. Hubig, U. Schollwöck, A.T.M.N. Islam, A. Schneidewind, and D.L. Quintero-Castro, Phys. Rev. B **96**, 054423 (2017).

[35] A. Abragam and M.H.L. Pryce, Proc. Roy. Soc. **A206**, 173 (1951).

[36] M.E. Lines, Phys. Rev. **131**, 546 (1963).

[37] P.H.Y. Li, R.F. Bishop, D.J.J. Farnell, and C.E. Campbell, Phys. Rev. B **86**, 144404 (2012).

[38] K. Takano, Phys. Rev. B **74**, 140402(R) (2006).

[39] V. Kataev, A. Möller, U. Löw, W. Jung, N. Schittner, M. Kriener, and A. Freimuth, J. Magn. Magn. Mater. **290-291**, 310 (2005).

[40] A. Möller, U. Löw, T. Taetz, M. Kriener, G. André, F. Damay, O. Heyer, M. Baraden, and J.A. Mydoshi, Phys. Rev. B **78**, 024420 (2008).

[41] M. Yehia, E. Vavilova, A. Möller, T. Taetz, U. Löw, R. Kligeler, V. Kataev, and B. Buchner, Phys. Rev. B **81**, 060414(R) (2010).

[42] Y. Miura, R. Hirai, Y. Kobayashi, and M. Sato, J. Phys. Soc. Jpn. **75**, 084707 (2006).

[43] N. Onishi, K. Oka, M. Azuma, Y. Shimakawa, Y. Motome, T. Taniguchi, M. Hiraishi, M. Miyazaki, T. Masuda, A. Koda, K.M. Kojima, and R. Kadono, Phys. Rev. B **85**, 184412 (2012).

[44] M. Matsuda, M. Azuma, M. Tokunaga, Y. Shimakawa, and N. Kumada, Phys. Rev. Lett. **105**, 187201 (2010).

[45] T. Shimokawa and H. Kawamura, Phys. Rev. Lett. **123**, 057202 (2019).

[46] A. Kitaev, Ann. Phys. **321**, 2 (2006).

[47] G. Jackeli and G. Khaliullin, Phys. Rev. Lett. **102**, 017205 (2009).

[48] K. Mehlawat, A. Thamizhavel, and Y. Singh, Phys. Rev. B **95**, 144406 (2017).

[49] Y. Kubota, H. Tanaka, T. Ono, Y. Narumi, and K. Kindo, Phys. Rev. B **91**, 094422 (2015).

[50] G.D. Munno, D. Armentano, M. Julve, F. Lloret, R. Lescouëzec, and J. Faus, Inorg. Chem. **38**, 2234 (1999).

[51] D. Armentano, G.D. Munno, F. Lloret, M. Julve, J. Curély, A.M. Babb, and J.Y. Lu, New J. Chem. **27**, 161 (2003).

[52] G.D. Munno, M. Julve, G. Viau, F. Lloret, J. Faus, and D. Viterbo, Angew. Chem. Int. Ed. Engl. **35**, 1807 (1996).

[53] G.D. Munno, T. Poerio, G. Viau, M. Julve, F. Lloret, Y. Journaux, and E. Riviére, Chem. Commun. **22**, 2587 (1996).

[54] A. Rodriguez-Diéguez, J. Cano, R. Kivekäs, A. Debdoubi, and E. Colacio, Inorg. Chem. **46**, 2503 (2007).

[55] M. Bird, Applied Superconductivity Conference 2020 Virtual Conference, Wk2LOr3A-01 (2020).

[56] D. Nakamura, A. Ikeda, H. Sawave, Y.H. Matsuda, and, S. Takeyama, Rev. Sci. Instrum. **89**, 095106 (2018).

[57] A. Miyake, H. Mitamura, S. Kawachi, K. Kimura, T. Kimura, T. Kihara, M. Tachibana, and M. Tokunaga, Rev. Sci. Instrum. **91**, 105103 (2020).

[58] K. Momma and F. Izumi, J. Appl. Cryst. **44**, 1272 (2011).

[59] S. Kimura, H. Yashiro, K. Okunishi, M. Hagiwara, Z. He, K. Kindo, T. Taniyama, and M. Itoh, Phys. Rev. Lett. **99**. 087602 (2007).

[60] S. Kimura, T. Takeuchi, K. Okunishi, M. Hagiwara, Z. He, K. Kindo, T. Taniyama, and M. Itoh, Phys. Rev. Lett. **100**, 057202 (2008).

[61] S. Kimura, M. Matsuda, T. Masuda, S. Hondo, K. Kaneko, N. Metoki, M. Hagiwara, T. Takeuchi, K. Okunishi, Z. He, K. Kindo, T. Taniyama, and M. Itoh, Phys. Rev. Lett. **101**, 207201 (2008).

[62] E. Canévet, B. Grenier, M. Klanjšek, C. Berthier, M. Horvatić, V. Simonet, and P. Lejay Phys. Rev. B **87**, 054408 (2013).

[63] B. Grenier, V. Simonet, B. Canals, P. Lejay, M. Klanjšek, M. Horvatić, and C. Berthier, Phys. Rev. B **92**, 134416 (2015).

[64] Z.Y. Zhao, X.G. Liu, Z.Z. He, X.M. Wang, C. Fan, W.P. Ke, Q.J. Li, L.M. Chen, X. Zhao and X.F. Sun, Phys. Rev. B **85**, 134412 (2012).

[65] S. Kimura, K. Okunishi, M. Hagiwara, K. Kindo, Z. He, T. Taniyama, M. Itoh, K. Koyama, and K. Watanabe, J. Phys. Soc. Jpn. **82**, 033706 (2013).

[66] S.K. Niesen, G. Kolland, M. Seher, O. Breunig, M. Valldor, M. Braden, B. Grenier, and T. Lorenz, Phys. Rev. B **87**, 224413 (2013).

[67] M. Matsuda, H. Onishi, A. Okutani, J. Ma, H. Agrawal, T. Hong, D.M. Pajerowski, J.R.D. Copley, K. Okunishi, M. Mori, S. Kimura, and M. Hagiwara, Phys. Rev. B **96**, 024439 (2017).

[68] Q. Faure, S. Takayoshi, S. Petit, V. Simonet, S. Raymond, L.-P. Regnault, M. Boehm, J.S. White, M. Månsson, C. Rüegg, P. Lejay, B. Canals. T. Lorenz. S.C. Furuya, T. Giamarchi, and B. Grenier, Nat. Phys. **14**, 716 (2018).

[69] Z. Wang, T. Lorenz, D.I. Gorbunov, P.T. Cong, Y. Kohama, S. Niesen, O. Breunig, J. Engelmayer, A. Herman, J. Wu, K. Kindo, J. Wosniza, S. Zherlitsyn, and A. Loidl, Phys. Rev. Lett. **120**, 207205 (2018).

[70] Y. Cui, H. Zou, N. Xi, Z. He, Y.X. Yang, L. Shu, G.H. Zhang, Z. Hu, T. Chen, R. Yu, J. Wu, and W. Yu, Phys. Rev. Lett. **123**, 067203 (2019).

[71] H. Zou, Y. Cui, X. Wang, Z. Zhang, J. Yang, G. Xu, A. Okutani, M. Hagiwara, M. Matsuda, G. Wang, G. Mussardo, K. Hódsági, M. Kormos, Z.Z. He, S. Kimura, R. Yu, W. Yu, J. Ma, and J. Wu, arXiv:2005.13302v2.

[72] Z. Zhang, K. Amelin, X. Wang, H. Zou, J. Yang, U. Nagel, T. Room, T. Dey, A.A. Nugroho, T. Lorenz, J. Wu, and Z. Wang, Phys. Rev. B **101**, 220411(R) (2020).

[73] N. Ishimura and H.Shiba, Prog. Theor. Phys. **63**, 743 (1980).

[74] Y. Han, S. Kimura, K. Okunishi, and M. Hagiwara, Appl. Magn. Reson., doi:10.1007/s00723-020-01296-w, (2020). (Review article)

[75] A.U.B. Wolter, H. Rakoto, M. Costes, A. Honecker, W. Brenig, A. Klümper, H.-H. Klauss, F.J. Litterst, R. Feyerherm, D. Jérome, and S. Süllow, Phys. Rev. B **68**, 220406(R) (2003).

[76] A. Matsuo, K. Hosokawa, Y. Narumi, K. Okunishi, N. Maeshima, T. Asano, Y. Ajiro, N. Ishida, T. Nogami, and K. Kindo, Prog. Theor. Phys. Suppl. **159**, 158 (2005).

[77] S. Glocke, A. Klümper, H. Rakoto, J.M. Broto, A.U.B. Wolter, and S. Süllow, Phys. Rev. B **73**, 220403(R) (2006).

[78] Y. Chen, M.B. Stone, M. Kenzelmann, C.D. Batista, D.H. Reich, and C. Broholm, Phys. Rev. B **75**, 214409 (2007).

[79] P. Lejay, E. Canevet, S.K. Srivastava, B. Grenier, M. Klanjsek, and C. Berthier, J. Cryst. Growth **317**, 128 (2011).

[80] F. Izumi and K. Momma, Solid State Phenom. **130**, 15 (2007).

[81] X.R. Huang, J. Appl. Crystallogr. **43**, 926 (2010).

[82] S.R. White, Phys. Rev. Lett. **69**, 2863 (1992).

[83] E. Jeckelmann, Phys. Rev. B **66**, 045114 (2002).

[84] H. Zou, R. Yu, and J. Wu, J. Phys.: Condens. Matter **32**, 045602 (2020).

[85] H. Onishi and M. Mori, private communication.

[86] S.G. Carling, C. Mathonière, P. Day, K.M.A. Malik, S.J. Coles, and M.B. Hursthouse, J. Chem. Soc., Dalton Trans. **9**,1839 (1996).

[87] Z. Honda, T. Kodama, R. Kikukawa, M. Hagiwara, T. Kida, M. Sakai, T. Fukuda, T. Fujihara, and N. Kamata, J. Phys. Soc. Jpn. **84**, 034601 (2015).

[88] Z. Honda, T. Kodama, M. Hagiwara, T. Kida, A. Okutani, M. Sakai, T. Fukuda, and N. Kamata, Solid State Sci. **59**, 15 (2016).

[89] S. Nakatsuji, K. Kuga, K. Kimura, R. Satake, N. Katayama, E. Nishibori, H. Sawa, R. Ishii, M. Hagiwara, F. Bridges, T.U. Ito, W. Higemoto, Y. Karaki, M. Halim, A.A. Nugroho, J.A. Rodriguez-Rivera, M.A. Green, and C. Broholm, Science **336**, 559 (2012).

[90] Y. Ishiguro, K. Kimura, S. Nakatsuji, S. Tsutsui, A.Q.R. Baron, T. Kimura, and Y. Wakabayashi, Nat. Commun. **4**, 2022 (2013).

[91] N. Katayama, K. Kimura, Y. Han, J. Nasu, N. Drichko, Y. Nakanishi, M. Halim, Y. Ishiguro, R. Satake, E. Nishibori, M. Yoshizawa, T. Nakano, Y. Nozue, Y. Wakabayashi, S. Ishihara, M. Hagiwara, H. Sawa, and S. Nakatsuji, Proc. Natl. Acad, Sci. U.S.A. **112**, 9305 (2015).

[92] Y. Han, M. Hagiwara, T. Nakano, Y. Nozue, K. Kimura, M. Halm, and S. Nakatsuji, Phys. Rev. B **92**, 180410(R) (2015).

[93] H. Man, M. Halim, H. Sawa, M. Hagiwara, Y. Wakabayashi, and S. Nakatsuji, J. Phys.: Condens. Matter **30**, 443002 (2018). (Review article)

[94] K. Sugawara, K. Sugimoto, N. Katayama, M. Hagiwara, Z. Honda, and H. Sawa, J. Phys. Soc. Jpn. **86**, 123302 (2017).

[95] A.F. Albuquerque, F. Alet, P. Corboz, P. Dayal, A. Feiguin, S. Fuchs, L. Gamper, E. Gull, S. Gürtler, A. Honecker, R. Igarashi, M. Körner, A. Kozhevnikov, A. Läuchli, S.R. Manmana, M. Matsumoto, I.P. McCulloch, F. Michel, R.M. Noack, G. Pawłowski, L. Pollet, T. Pruschke, U. Schollwöck, S. Todo, S. Trebst, M. Troyer, P. Werner, S. Wessel, for the ALPS collaboration., J. Magn. Magn. Mater. **310**, 1187 (2007); see also (http://alps.comp-phys.org/).

[96] A.W. Sandvik, Phys. Rev. B **59**, R14157(R) (1999).

[97] F. Alet, S. Wessel, and M. Troyer Phys. Rev. E **71**, 036706 (2005).

[98] L. Pollet, S.M.A. Rombouts, K. Van Houcke, and K. Heyde, Phys. Rev. E **70**, 056705 (2005).

[99] K. Takano, The Physical Society of Japan 2019 Autumn Meeting, 13aD11-8 (2019).

[100] T. Shimokawa, private communication.

[101] A. Okutani, H. Onishi, S. Kimura, T. Takeuchi, T. Kida, M. Mori, A. Miyake, M. Tokunaga, K. Kindo, and M. Hagiwara, J. Phys. Soc. Jpn. **90**, 044704 (2021).

Publication List

1. "High-Field Multi-Frequency ESR in the Quasi-1D $S = 1/2$ Ising-Like Antiferromagnet $BaCo_2V_2O_8$ in a Transverse Field"
   A. Okutani, S. Kimura, T. Takeuchi, and M. Hagiwara
   Appl. Magn. Reson. **46**, 1003–1006 (2015).

2. "Magnetic properties of single-crystals of the $S = 2$ quasi-1D Heisenberg antiferromagnet $MnCl_3$(bpy)"
   M. Hagiwara, S. Shinozaki, **A. Okutani**, D. Yoshizawa, T. Kida, T. Takeuchi, O.N. Risset, D.R. Talham, and M.W. Meisel
   Phys. Procedia **75**, 106–113 (2015).

3. "Transport properties of the metallic two-dimensional triangular antiferromagnet Ag_2CrO_2"
   T. Kida, **A. Okutani**, H. Yoshida, and M. Hagiwara
   Phys. Procedia **75**, 647–652 (2015).

4. "High field magnetization of single crystals of the $S = 1/2$ quasi-1D Ising-like antiferromagnet $SrCo_2V_2O_8$"
   A. Okutani, T. Kida, T. Usui, T. Kimura, K. Okunishi, and M. Hagiwara
   Phys. Procedia **75**, 779–784 (2015).

5. "Antiferromagnetic order in single crystals of the $S = 2$ quasi-one-dimensional chain $MnCl_3$(bpy)"
   S. Shinozaki, **A. Okutani**, D. Yoshizawa, T. Kida, T. Takeuchi, S. Yamamoto, O.N. Risset, D.R. Talham, M.W. Meisel, and M. Hagiwara
   Phys. Rev. B **93**, 014407-1–6 (2016) (Editors' Suggestion).

6. "Colossal Seebeck effect enhanced by quasi-ballisitic phonons dragging massive electrons in $FeSb_2$"
   H. Takahashi, R. Okazaki, S. Ishiwata, H. Taniguchi, **A. Okutani**, M. Hagiwara, and I. Terasaki
   Nat. Commun. **7**, 12732-1–6 (2016).

7. "Long-range magnetic order and interchain interactions in the $S = 2$ chain system $MnCl_3$(bpy)"
   R.S. Fishman, S. Shinozaki, **A. Okutani**, D. Yoshizawa, T. Kida, M. Hagiwara, and M.W. Meisel
   Phys. Rev. B **94**, 104435-1–5 (2016).

8. "Crystal structures and magnetic properties of the honeycomb-lattice antiferromagnet $M_2(\mathrm{pymca})_3(ClO_4)$, ($M$=Fe, Co, Ni)"
   Z. Honda, T. Kodama, M. Hagiwara, T. Kida, **A. Okutani**, M. Sakai, T. Fukuda, and N. Kamata
   Solid State Sci. **59**, 15–18 (2016).

9. "Magnetic structure and dispersion relation of the $S = \frac{1}{2}$ quasi-one-dimensional Ising-like antiferromagnet $BaCo_2V_2O_8$ in a transverse magnetic field"

M. Matsuda, H. Onishi, **A. Okutani**, J. Ma, H. Agrawal, T. Hong, D.M. Pajerowski, J.R.D. Copley, K. Okunishi, M. Mori, S. Kimura, and M. Hagiwara
Phys. Rev. B **96**, 024439-1–8 (2017).

10. "Surface magnetism of exfoilated α-Co hydroxide nanosheets"
    Z. Honda, K. Anai, M. Hagiwara, T. Kida, **A. Okutani**, M. Sakai, T. Fukuda, and N. Kamata
    J. Phys. Chem. Solids **107**, 14–17 (2017).

11. "Direct observation of spin-quadrupolar excitations in $Sr_2CoGe_2O_7$ by high-field electron spin resonance"
    M. Akaki, D. Yoshizawa, **A. Okutani**, T. Kida, J. Romhányi, K. Penc, and M. Hagiwara
    Phys. Rev. B **96**, 214406-1–16 (2017).

12. "High-field Magnetism of the Honeycomb-lattice Antiferromagnet $Cu_2(pymca)_3(ClO_4)$"
    A. Okutani, T. Kida, Y. Narumi, T. Shimokawa, Z. Honda, K. Kindo, T. Nakano, Y. Nozue, and M. Hagiwara
    J. Phys. Soc. Jpn. **88**, 013703-1–4 (2019).

13. "E_8 spectra of Quasi-one-dimensional Antiferromagnet $BaCo_2V_2O_8$ under Transverse Field"
    H. Zou, Y. Cui, X. Wang, Z. Zhang, J. Yang, G. Xu, **A. Okutani**, M. Hagiwara, M. Matsuda, G. Wang, G. Mussardo, K. Hódsági, M. Kormos, Z.Z. He, S. Kimura, R. Yu, W. Yu, J. Ma, and J. Wu
    arXiv:2005.13302v2.

14. "Spin Excitations of the $S = 1/2$ One-dimensional Ising-Like Antiferromagnet $BaCo_2V_2O_8$ in Transverse Magnetic Fields"
    A. Okutani, H. Onishi, S. Kimura, T. Takeuchi, T. Kida, M. Mori, A. Miyake, M. Tokunaga, K. Kindo, and M. Hagiwara
    J. Phys. Soc. Jpn. **90**, 044704-1–9 (2021).

Acknowledgment

I wish to express my sincere gratitude to Prof. Masayuki Hagiwara at AHMF (Center for Advanced High Magnetic Field Science) in Osaka University for assiduous guidance, valuable suggestions, enlightening discussions, and continuous encouragement. I am indebted to Assoc. prof. Yasuo Narumi for teaching me the experimental techniques, valuable suggestions, and helpful advice. I am grateful to Dr. Takanari Kida for teaching me the experimental techniques, valuable suggestions, and helpful advice. I wish to express my gratitude to Dr. Mitsuru Akaki at Molecular Photoscience Research Center in Kobe University for teaching me the experimental techniques, valuable suggestions, and helpful advice. I also would like to thank Mr. Kazuya Taniguchi for making the pulse magnet and the experimental parts. I wish to express my gratitude to Dr. Takahito Fujita for teaching me the experimental techniques, valuable suggestions, and helpful advice. I also would like to thank Dr. Daichi Yoshizawa at Institute for Molecular Science for helpful and enjoyable discussion and support for experiments and my student life.

I particularly acknowledge the following researchers; Assoc. prof. Shojiro Kimura at Institute for Materials Research in Tohoku University for teaching me the experimental techniques, valuable suggestions, and helpful advice, Dr. Michiyasu Mori and Hiroaki Onishi at Advanced Science Research Center in Japan Atomic Energy Agency for the calculation of magnetic excitation for $BaCo_2V_2O_8$, valuable suggestions and helpful advice from a theoretical view point, Dr. Tetsuya Takeuchi at Low Temperature Center in Osaka University for the specific heat experiment, Prof. Masashi Tokunaga and Dr. Atushi Miyake at Institute for Solid State Physics in The University of Tokyo for the high-field magnetostriction experiment, Prof. Koichi Kindo at Institute for Solid State Physics in The University of Tokyo for making the pulse magnet, Assoc. prof. Zentaro Honda at Saitama University for providing us the polycrystalline $Cu_2(pymca)_3(ClO_4)$ sample and helpful advice, Prof. Hiroshi Sawa at Nagoya University and Dr. Kento Sugawara at National Institutes for Quantum and Radiological Science and Technology for valuable suggestions and helpful advice from a structure analysis of $Cu_2(pymca)_3(ClO_4)$, Prof. Yasuo Nozue at Osaka University and Assoc. prof. Takehito Nakano at Ibaraki University for the X-band electron spin resonance experiment, Dr. Tokuro Shimokawa at Okinawa Institute of Science and Technology Graduate University for the calculation of magnetization for $Cu_2(pymca)_3(ClO_4)$, valuable suggestions and helpful advice from a theoretical view point, Prof. Ken'ichi Takano at Toyota Technological Institute for valuable suggestions and helpful advice from a theoretical view point.

I wish to express my gratitude to the members of Hagiwara Laboratory at AHMF in Osaka University for helpful and enjoyable discussion and support for experiments and my student life.

I also would like to very thank my family for supporting my student life.